Experimental Investigation of a Normally Impinging Planar Jet

by

Supun Pieris

A thesis
presented to the University of Waterloo
in fulfillment of the
thesis requirement for the degree of
Master of Applied Science
in
Mechanical and Mechatronics Engineering

Waterloo, Ontario, Canada, 2017

Abstract

Impinging jets are commonly employed in engineering applications, such as cooling and drying processes, requiring relatively high local transport properties. Flow development of a planar impinging jet and the effect of varying jet parameters are investigated experimentally in a jet facility that is specifically designed, fabricated, and characterized as part of the current study. The velocity field is measured using time-resolved, planar, two-component Particle Image Velocimetry. The investigation focuses on two jet parameters: Reynolds number and nozzle-to-plate spacing. Four test cases are investigated, including two Reynolds numbers 3000 and 6000, and two nozzle-to-plate spacings, $2B$ and $4B$, where B is the jet width.

Primary vortices form in the shear layer just downstream of the nozzle exit due to amplification of disturbances through the Kelvin-Helmholtz instability. Vortex shedding exhibits higher periodicity with increasing Reynolds number but is not significantly affected by changes to the nozzle-to-plate spacing. Further, vortex shedding location shifts upstream with increasing Reynolds number. The Strouhal number based on vortex shedding frequency varies between $0.4 \leq \mathrm{St}_B \leq 0.5$ and the vortices are convected downstream at an average convective velocity of 57% of the jet centerline velocity for all cases examined. For $\mathrm{Re}_B = 6000$, the characteristic wavelength of the primary vortices is $1.1B$ for both nozzle-to-plate spacings. At the lower Reynolds number, the wavelengths increase to approximately $1.3B$ and $1.5B$, for nozzle-to-plate spacings of $2B$ and $4B$, respectively. Local deceleration of primary vortices, due to the impinging surface, causes consecutively shed vortices to merge, with vortex merging observed in all cases investigated.

As the primary vortices pass in the outer shear layer of the wall jet region, secondary vortices of opposingly signed vorticity form due to roll-up of the wall bound vorticity in the inner shear layer. The secondary vortex shedding is marked by amplification of the surface normal velocity fluctuations in the inner shear layer when $x/B > 3$. The secondary vortex shedding shows a lower periodicity compared to the primary vortices but in general have convective velocities that are larger than that of the primary vortices. As the Reynolds number is increased, the secondary vortex formation is suppressed, and, as a result, the wall jet develops more parallel to the impinging surface. With increasing Reynolds number, the convective velocities of the secondary vortices also decrease. In all cases, pairing between a primary and secondary vortex is observed and the paired vortices are convected in the streamwise direction away from the surface. At the higher Reynolds number, the pairing is immediately followed by vortex breakdown.

Acknowledgements

First and foremost, I would like to thank my supervisors, Dr. Serhiy Yarusevych and Dr. Sean D. Peterson for your guidance and knowledge provided during my masters studies. Your commitment to producing high quality results was essential in producing this work. I am grateful to have worked with not just one, but two mentors that always pushed me to become a better researcher.

To my colleagues in the fluids research groups: John Kurelek, Jeff McClure, Ben Pocock, Mark Istvan, Ajith Airody, Erik Marble, Jonathan Deng, Caddie Zhang, Laura Haya, Burak Tuna, and Winston Hu, thank you for the insightful discussions, willingness to always help, and friendship. Caddie, your knowledge of PIV was pivotal in completing these experiments and it was nice to share the stress during our weeks of collecting data. John, thank you for your help during experimental setup, teaching me the ways of MATLAB/Inkscape figure making, helping with PIV image processing and for getting me into playing squash. Jeff, thank you for our insightful discussions of CFD, spectral methods, turbulence, and suffering with me through the early train rides to Toronto. All of you were always available to lend a helping hand, no matter how many times I asked questions.

Thank you to the technical staff in the Mechanical and Mechatronics Engineering department: Neil Griffett, Andy Barber, Richard Gordan, Robert Wagner, Andrew Urschel, Graeme Adair, Rick Forgett, Phil Laycock, and Jorge Cruz. A special thanks to Jason Benninger, who fabricated major sections of the jet facility. Jason's expertise in machining and adherence to good design was vital in bringing the jet facility online without any issues. Thank you to James Merli for setting up the electrical systems to be able to run the Jet facility and allowing me to ask numerous questions about electrical work throughout the project.

Thank you to Sarah, for your steady and unfaltering support during my masters studies, especially for your words of positivity during the months of thesis writing. It definitely kept me grounded so that I was able to finish this project without anymore delay.

I would like to thank my mother, Rita, and all of my family overseas for the constant encouragement, not only during the past two years, but throughout my academic career.

Finally, I would like to thank the Natural Sciences and Engineering Research Council of Canada (NSERC), Ontario Centres of Excellence, and Suncor Energy for the financial support in this research project.

Table of Contents

List of Tables

List of Figures

Nomenclature

Dimensionless Numbers

Symbol	Description	Definition
Ma	Mach Number	$\frac{U_o}{c}$
Re_B	Jet Reynolds number based on nozzle width	$\frac{U_o B}{\nu}$
Re_D	Jet Reynolds number based on nozzle diameter	$\frac{U_o D}{\nu}$
St_e	Nozzle width based excitation Strouhal number	$\frac{f_e U_o}{D}$
$St_{B,0}$	Nozzle width bases Strouhal number defining characteristic shedding frequency of primary vortices	$\frac{fB}{U_o}$
St_B	Nozzle width based Strouhal number	$\frac{fB}{U_o}$
St_D	Nozzle width based Strouhal number	$\frac{fD}{U_o}$
R	Velocity ratio in parallel shear flows with two streams	$\frac{U_1-U_2}{U_1+U_2}$
t^*	Dimensionless time	$\frac{tU_o}{B}$

Roman Symbols

Symbol	**Description**	**Units**
ΔP_{con}	Mean pressure drop across the jet facility contraction	Pa
Δs	Particle displacement between two consecutive pulses of the laser in the potential core region	px
Δt	Frame separation time setting for the laser	µs
$\tilde{u}$	Bandpass filtered root mean square of x-component velocity	$\mathrm{m\,s^{-1}}$
$\tilde{v}$	Bandpass filtered root mean square of y-component velocity	$\mathrm{m\,s^{-1}}$
a	Vortex diameter	m
a_i	Temporal amplitude of POD mode i	
B	Nozzle width (planar jet)	m
b	Distance between two vortex cores	m
c	speed of sound	$\mathrm{m\,s^{-1}}$
D	Nozzle diameter (axisymmetric jet)	m
$f_\#$	Numerical aperature of lens	
f_e	Forced excitation frequency	Hz
f_s	Image acqusition frequency	Hz
H	Normal distance between nozzle and plate	m
k	Wavenumber	$\mathrm{m^{-1}}$
k_0	Charactersitic wavenumber of primary vortices	$\mathrm{m^{-1}}$
L	Span of the nozzle exit	m
L_c	Length of contraction	m
M	Magnification factor	
P_{dyn}	Mean dynamic pressure at the jet exit along the jet centerline	Pa
r	Radial direction in a free or impinging axisymmetric jet	m

U	x-component velocity	$\mathrm{m\,s^{-1}}$
u	Fluctuating x-component velocity	$\mathrm{m\,s^{-1}}$
u'	Root mean square of the x-component velocity	$\mathrm{m\,s^{-1}}$
U_c	Jet centerline velocity measured at the midspan	$\mathrm{m\,s^{-1}}$
U_m	Maximum streamwise velocity in the wall jet velocity profile	$\mathrm{m\,s^{-1}}$
U_o	Characteristic velocity at the jet exit for free jets, impinging jets and wall jets	$\mathrm{m\,s^{-1}}$
$U_{cv,P}$	Convective velocity of the primary vortices	$\mathrm{m\,s^{-1}}$
$U_{cv,S}$	Convective velocity of the secondary vortices	$\mathrm{m\,s^{-1}}$
V	y-component velocity	$\mathrm{m\,s^{-1}}$
v	Fluctuating y-component velocity	$\mathrm{m\,s^{-1}}$
v'	Root mean square of the y-component velocity	$\mathrm{m\,s^{-1}}$
x	Direction parallel to the impinging surface	m
y	Direction normal to the impinging surface	m
y_m	Wall normal distance where the streamwise velocity is a maximum for a wall jet	m
$y_{1/2}$	Wall normal distance where the streamline velocity velocity is $0.5U_m$ for a wall jet	m
z	Spanwise direction in an impinging jet	m

Greek Symbols

Symbol	**Description**	**Units**
χ	Streamwise direction in a free jet	m
χ_T	Streamwise distance where a free jet transitions to turbulent flow	m
η	Transverse direction in a free slot jet	m
Γ	Circulation	$\mathrm{m}^2\,\mathrm{s}^{-1}$
Λ	Autocovariance matrix of velocity fluctutations	$\mathrm{m}\,\mathrm{s}^{-1}$
λ	Disturbance wavelength	m
λ_0	Characteristic wavelength of primary vortices	m
λ_i	Eigenvalues representing the relative turbulent kinetic energy of POD spatial modes	
λ_x	Characteristic surface parallel wavelength of merged primary vortices	m
ω_z	Spanwise vorticity	$\mathrm{rad}\,\mathrm{s}^{-1}$
ψ_i	POD mode representing spatial distribution of turbulent kinetic energy	
ρ	Density	$\mathrm{kg}\,\mathrm{m}^{-3}$
θ	Azimuthal direction in a free or impinging axisymmetric jet	m
ζ	Spanwise direction in a free slot jet	m

Chapter 1

Introduction

Jets are found in many engineering applications, such as cooling of turbine blades, drying processes, heat exchangers, tempering of various materials, and electronics cooling [1–5]. Impinging jet flows in particular are widely used for the aforementioned applications, due to the relatively high local transport properties and the possibility of simple and cost effective implementation. An impinging jet flow is created when a jet impacts a surface and the fluid is diverted away from the jet centreline by the surface. Although impinging jet flows appear at first to be deceivingly simple in terms of their mean flow features, closer inspection reveals rich dynamics. Only within the last two decades has the spatio-temporal behaviour of these flows become observable in experiments, due to developments in measurement techniques such as Particle Image Velocimetry (PIV) that can capture velocity fields for swiftly evolving flows with appropriate temporal resolution [6, 7]. The combined spatial and temporal resolution is essential for analyzing the dynamics of the the flow being studied. Some recent studies have focused on the effect of the jet parameters such as nozzle geometry [8–10], jet-to-plate height [11, 12] and Reynolds number effects [13, 14] on the flow and transport properties. However, much of the research effort has been focused on the heat transfer characteristics of impinging jet flow [9, 11, 15, 16].

One of the distinct features of impinging jet flows is the periodic shedding of coherent structures [17–19]. The coherent structures form in the shear layers of the free jet region, downstream of the nozzle exit, by the Kelvin-Helmholtz instability [13, 14, 16, 20, 21]. These structures enhance entrainment of ambient air and act to transfer momentum from the core of the jet to the outer shear layer. The shedding frequency of the structures is characterized by the non-dimensional Strouhal number, with a range of Strouhal numbers from 0.33 to 0.64, reported in the literature for various jet configurations [19]. For the high aspect ratio slot jet, the coherent structures are oriented such that the vortex cores extend along the span of the jet, while toroidal vortices form in axisymmetric jet flows

[21]. The periodic shedding causes unsteadiness downstream of the jet exit, as seen in time resolved velocity measurements [8, 17]. The coherent structures are then convected downstream by the mean flow into the stagnation region, where the wall causes the coherent structures to deform and stretch [12, 13]. Coherent structures can penetrate into the core of the flow altering transfer properties near the wall [13, 16]. The relative strength of the coherent structures decreases with an increase in Reynolds number, with a critical Reynolds number marking the transition to a different flow regime, where the coherent structures no longer impinge as deeply into the near wall region due to being deflected away by the mean flow [13]. Vortex merging may occur as the wall decelerates the leading vortex compared to upstream vortices [8, 22, 23]. The structures are then transported along the shear layer parallel to the wall as the flow re-orients, forming the wall jet region. Flow reversal near the wall is observed around the region where the wall jet forms [24]. The flow reversal is due to secondary vortices that can form close to the wall due to the passing of coherent structures in the wall jet shear layer, as observed by both experimental [12, 24, 25] and numerical simulations [18, 19]. After being convected downstream along the wall, the coherent structures break down into smaller scales, marking the transition to a fully turbulent wall jet [8, 21].

A significant number of previous experimental and numerical studies that have examined the dynamics of coherent structures in impinging jet flow have focused on the axisymmetric jet [8, 10, 17, 24, 25]. Additionally, some discrepancies exist between experimental data measured in the high shear regions of impinging jet flows, such as mean velocities, and Reynolds stresses, collected using point measurement techniques [24, 26, 27]. Therefore, knowledge gaps in the study of coherent structures that form in high aspect ratio impinging jet flows remain to be filled through further systematic investigation. Furthermore, it is of interest to characterize the effect of jet parameters on the coherent structure dynamics, as these structures are known to play a vital role in transport properties of impinging jet flows [16, 25, 28].

1.1 Study Objectives

As previously mentioned, much of the research that has been conducted regarding impinging jet flows has focused on the thermo-fluidic behaviour of axisymmetric jets. In the present study, an impinging jet issued from a high aspect ratio slot nozzle is investigated experimentally using time-resolved PIV. PIV allows for the flow field information to be captured in both space and time simultaneously, which can be exploited in order to elucidate the unsteady behaviour of the coherent structures. Furthermore, it is of interest to systematically determine the effect of relevant jet parameters, including Reynolds number and height of the nozzle exit above the surface, on the flow and coherent structure dynamics. The specific research objectives of the present study are as follows:

1. Characterize the unsteady behaviour of the coherent structures in a planar impinging jet flow from their formation to breakdown.
2. Examine the effect of Reynolds number and nozzle-to-plate spacing on the flow topology

The investigation is presented in the following chapters of this thesis. Background information about impinging jet flows and vortex dynamics is provided in Chapter 2. A description of the experimental methodology employed is presented in Chapter 3. The results and analysis of the collected data are found in Chapter 4. Lastly, the derived conclusions and recommendations are summarized in Chapters 5 and 6, respectively.

Chapter 2

Background

Impinging jet flows have been widely studied over the past few decades, however, the spatio-temporal behaviour of coherent structures for a slot jet have not been examined thoroughly. Furthermore, many of the previous literature has focused on the axisymmetric jet rather than the slot jet, due to ease of manufacturing during the experimental setup stage of the investigation. In this chapter, background information and previous work relevant to the discussion of impinging jet flows is presented. A brief overview of free jet flows is provided in Section 2.1. In Section 2.2, a more comprehensive discussion about impinging jet flows is presented. Lastly, in Section 2.3, vortex dynamics of impinging jet flows is explored.

2.1 Free Jet Flow

The structure and behaviour of the free jet has been well established through numerous previous works [21, 29–34]. The free jet is characterized by two regions that transform as the jet develops downstream of the jet exit: the potential core and the mixing layer. The two characteristic regions, along with other features of the plane free jet flow, are shown in Fig. 2.1. The free jet is characterized by its Reynolds number, $\mathrm{Re}_B = U_o B/\nu$ and $\mathrm{Re}_D = U_o D/\nu$, for a plane free jet and a axisymmetric free jet, respectively. In the definition of the Reynolds number, U_o is defined as a characteristic velocity at the jet exit, B is the nozzle width while D is the nozzle diameter, and ν is the kinematic viscosity of the working fluid. A Cartesian coordinate system, $(\chi,\, \eta,\, \zeta)$, is used for plane free jets, with χ oriented along the streamwise direction, η oriented along the transverse direction, and ζ placed in the spanwise direction. For an axisymmetric free jet, a cylindrical coordinate system, $(\chi,\, r,\, \theta)$, is used and the transverse and spanwise coordinates are replaced by radial and azimuthal coordinates, respectively.

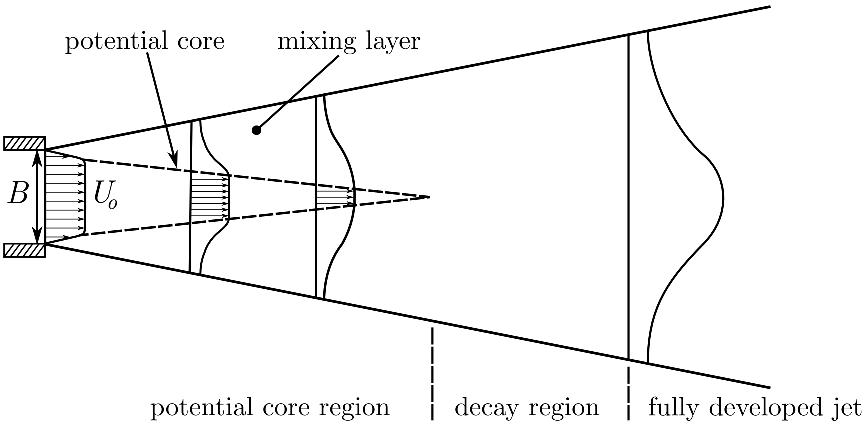

Figure 2.1: A free jet and characteristic regions.

Immediately after the fluid issues from the jet exit, the potential core contains the bulk of the momentum. The mixing layer surrounding the potential core acts to enhance fluid entrainment and transfers mass, momentum, and energy outward into the environment from the jet. The area that is unaffected by the transport mechanism of the mixing layer is the potential core. The mixing region spreads to conserve axial momentum as the bulk velocity decays [21, 29]; coherent structure formation is also observed in this region [30, 35]. At subsequent downstream locations, the potential core diameter decreases, as the mixing region spreads into the potential core. Eventually, the core of the jet disappears, and the mixing region continues to spread (increasing the jet width), ultimately developing into a self-similar velocity profile far downstream. The length of the potential core extends approximately 6 to 8 diameters downstream of the jet exit for Reynolds numbers ranging from $\mathrm{Re}_D = 43\,000$ [30] to $\mathrm{Re}_D = 55\,000$ [35]. Comparatively, the potential core length of planar free jet flows has a larger range of 4.7 to 7.7 nozzle widths according to Livingood & Hrycak [36]. Others have reported that the typical potential core length in a slot jet is approximately 5 to 6 nozzle widths and depends heavily on the velocity and turbulence intensity profiles at the nozzle exit and the nozzle geometry of the jet [37, 38]. Downstream of the potential core, a decrease in centreline axial velocity is encountered as the momentum is distributed over a larger area due to the increase in jet width [32, 39].

The transition of a free jet has been both studied qualitatively through flow visualization and measurements of velocity. McNaughton & Sinclair [40] observed four main types of round free jets as the Reynolds number is varied: a dissipated-laminar jets ($\mathrm{Re}_D < 300$), fully laminar jets ($300 \lesssim \mathrm{Re}_D \lesssim 1000$), semi-turbulent jets ($1000 \lesssim \mathrm{Re}_D \lesssim 3000$), and fully turbulent jets ($\mathrm{Re}_D > 3000$). However, the downstream location where transition occurs, is not reported by McNaughton & Sinclair [40], as the flow regimes are qualitatively defined through flow visualization. Others have attempted to find a more definitive criteria for the turbulence transition location, χ_T. Experiments on round free jets show that the streamwise velocity profile of the jet achieves the characteristic Gaussian shape prior to the location where the fluctuating velocity components became turbulent [30, 32, 41]. Therefore, the velocity profile alone could not serve to identify χ_T. By recording the location where the turbulence intensity values of non-streamwise velocity components are within 5% of their turbulent values, a new criteria for χ_T is defined by Yule [30]. At a Reynolds number of $\mathrm{Re}_D = 9000$, χ_T is between 3-4 nozzle diameters, while at $\mathrm{Re}_D = 10^5$, $\chi_T \approx 1$. The transition to turublence is also accompanied by development of vortices in the mixing layer of the free jet as indicated by the periodic nature of Reynolds stress covariance profiles downstream of the nozzle exit [30].

Popiel & Trass [21] employed a smoke wire visualization technique to show the formation of vortices in the mixing layer, formed through the Kelvin-Helmholtz instability [42, 43], at $\mathrm{Re}_D = 10\,000$ and $\mathrm{Re}_D = 20\,000$. Later work by Cornaro *et al.* [34] also employed smoke wire flow visualization on a free jet configuration at $\mathrm{Re}_D = 6000$, $10\,000$, $15\,000$, and $20\,000$ using nozzles with diameters of $D = 47.2$, 72.6, and 98.6 mm. A difference in flow development downstream of the jet exit is observed for the same Reynolds number when using a nozzle with a different diameter, which is attributed to the variation of turbulence levels in the flow near the nozzles exit edges [34]. Yule [30] visualized the formation of the vortices in the mixing layer using pulsed hydrogen bubbles at $\mathrm{Re}_D = 9000$ and differentiates between the vortices that form in the transitional region of the free jet and the weaker eddies seen in the fully developed turbulent free jet region observed by Fiedler [44]. Proper orthogonal decomposition (POD) [45] is implemented in the far field region of an axisymmetric free jet by Shinneeb *et al.* [31], to identify the coherent structures of the velocity field assembled by PIV for $\mathrm{Re}_D = 22\,500$. The coherent structures consist of vortices of both positive and negative rotational directions in the far-field region. Shinneeb *et al.* [31] describe that, along the axial direction, the number of vortices decreases as the size of the vortices increases, which is indicative of shear layer vortex merging.

Different types of output velocity profiles have been considered in previous investigations that studied free jets. The desired velocity profile will depend on the choice of the nozzle, with the nozzles used in literature falling into one of three categories: contoured contractions, straight ducts, and orifice plates. The use of a contoured contraction creates a velocity profile that is typically referred to as a “top-hat” profile; the streamwise velocity profile is uniform except in the shear layers, where the velocity decreases to near zero values [32, 46, 47]. The turbulence intensity profile shows an opposite trend, with the highest turbulence intensity values found in the shear layer of the jet [32, 46–48]. Although the turbulence intensity profile at the jet exit is Reynolds number dependent, the shape of the normalized axial velocity profile is found to be insensitive to Reynolds number in the range of 6000$\leq$ Re_D $\leq$30 000 [32].

Ducts, typically pipes, are another method of creating a jet [31, 34, 47]. By using a sufficiently long duct, the exit velocity profile resembles fully developed pipe flow, with the maximum streamwise velocity measured at the jet centre with a decrease in velocity towards the shear layers [47]. The turbulence intensity profile of the streamwise velocity at the pipe exit has a minimum at the jet centre and increases radially outwards up to a maximum and rapidly decreases to near zero value due to the wall. When the pipe length does not allow for fully developed flow, the velocity and turbulence intensity profiles is similar to the velocity profile created by a contraction [31, 34], however, it is highly dependent on the inlet flow characteristics at the pipe entrance.

One of the less common options for creating a jet flow is the use of an orifice plate. The velocity profile shows acceleration of the flow in the shear layer due to the saddle shaped profile of the orifice nozzle exit [46, 48, 49]. The turbulence intensity profile shows a similar trend to that of the contoured nozzle exit, with less spreading [46]. With all three types of nozzles discussed above, the nozzle exit shape is typically round due to ease of fabrication of such a nozzle.

The characterization of the exit flow conditions for a free jet issued from a slot nozzle in literature is sparse. From the few studies that focus on plane free jets, Gori & Nino [50] presented the velocity and the turbulence intensity profiles at a location half a nozzle width away from the exit. A contracting rectangular nozzle with an aspect ratio of 10 is used to create the plane free jet at a $\mathrm{Re}_B = 7000$ and 11 500. The results match well with those of the round jet created using a contoured nozzle: the velocity profiles show a uniform velocity across the jet exit for both Reynolds numbers. For $\mathrm{Re}_B = 7000$, the turbulence intensity profile is nearly constant, while the turbulence intensity profile for $\mathrm{Re}_B = 11\,500$ shows the typical profile with higher intensity values in the shear layers of the jet.

The works discussed previously that report on the characterization of various nozzle types are used as benchmarks to evaluate the performance of the facility used in the current study. The velocity and turbulence intensity profiles at the nozzle exit are measured and compared in order to make appropriate design changes. The details of the design process and the evaluation of the experimental facility is provided in Chapter 3.

2.2 Impinging Jet Flow

An impinging jet flow is created by placing a rigid surface downstream of a free jet. If the surface is oriented orthogonal to the streamwise direction, a normally impinging jet flow is established. Comparatively, a surface oriented at any other angle will create an oblique jet,

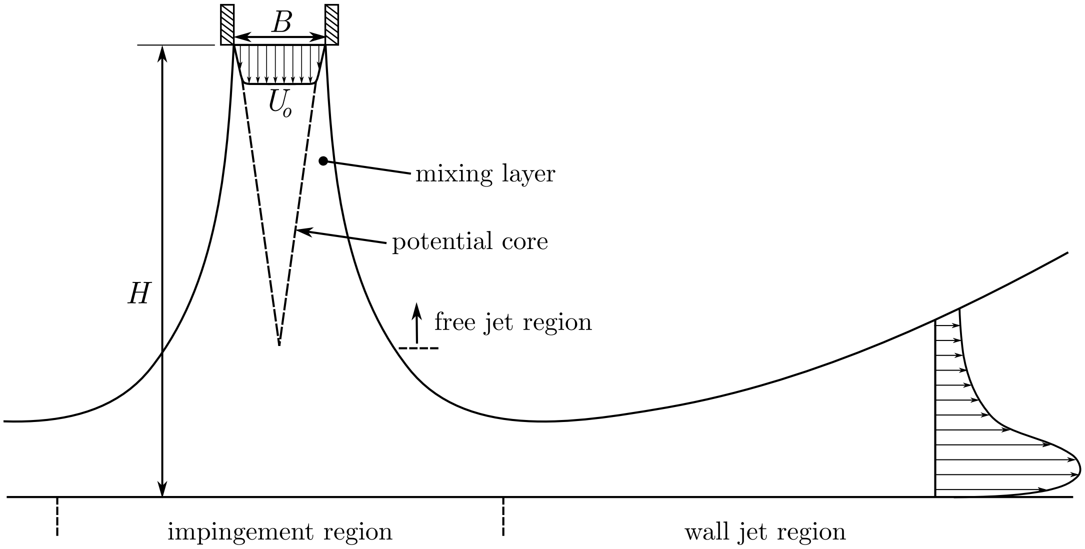

Figure 2.2: Characteristic flow regions of a normally impinging jet flow along with relevant parameters and nomenclature.

while a free jet oriented parallel and sufficiently close to the surface will produce a wall jet. The flow features and dynamics of the oblique jet are not the focus of this study; for more information on the fluid dynamics of oblique jets, the reader is referred to [29, 51, 52]. The background information provided in this section will focus on literature pertaining to normal impinging jet flows, as seen in Fig. 2.2.

There are three characteristic regions that are observed in impinging jet flows: a free jet region, impingement region, and a wall jet region. The features of the free jet and stagnation regions are described in Section 2.2.1, while the wall jet region is discussed in Section 2.2.2. In general, the free jet region initiates at the nozzle exit and extends up to the impingement region, which forms above the wall due to flow stagnation. As the flow approaches the surface, the decrease in velocity is accompanied by the increase in static pressure that affects the upstream flow field. A decrease in static pressure along the surface is then observed and the desirable pressure gradient accelerates the reoriented flow, which promotes the formation of the wall jet region [53, 54].

The non-dimensional numbers that characterize the normal impinging jet flow are the jet Reynolds number (similar to a free jet), Re_D for an axisymmetric jet or Re_B for a planar jet, and the distance between the jet exit and the impinging wall, H, normalized by the jet diameter or width (H/D or H/B). As previously discussed in Section 2.1, the nozzle geometry will also affect the downstream free jet region due to the differences in the exit velocity and turbulence intensity profile generated by different nozzles [46, 49]. In plane impinging jet flow, a Cartesian coordinate system (x, y, z) is used to describe the flow field, while a cylindrical coordinate system (r, y, θ) is used for axisymmetric impinging jets. Directions x and r are oriented parallel to the impinging surface and y is oriented normal to the impinging surface. The spanwise and azimuthal direction are described by z and θ, respectively. In both cases, the origin is placed at the geometric impingement point, where the jet centreline axis intersects the impinging surface.

The transition of impinging jet flows is a complex phenomenon due to the numerous combinations of jet configurations and, as a result, has been considered only in a few studies. The jet Reynolds number at which transition occurs for a normally impinging round jet is reported as $\mathrm{Re}_D = 2500$, independently of other factors, by Polat *et al.* [55]. In the literature survey by Gauntner *et al.* [56], the transition Reynolds number is reported to be 3000. However, it becomes difficult to definitively determine the transition of an impinging jet flow due to the many other factors that affect the transition process: conditions at the nozzle exit (velocity and turbulent intensity), nozzle-to-plate spacing, and impingement angle. A more pragmatic approach is to use the free jet transition definition as discussed in Section 2.1, to classify the impinging jet flow as laminar or turbulent [57], which essentially ignores the effect of the impinging surface. This definition of transition is problematic because the transition length is affected by placement of the impinging surface, which fundamentally changes the flow. Although the transition process in free jet flows has a more concrete definition, the transition of an impinging jet flow is much more complex and remains to be studied through further investigation.

There are many factors that affect the flow development of impinging jet flow, such as Reynolds number, nozzle geometry, nozzle-to-plate spacing, and flow conditions at the nozzle exit. An overview of the effect of Reynolds number and nozzle-to-plate spacing on the impinging jet flow development is provided here, as these two parameters are the most relevant to the current study. Beaubert & Viazzo [58] used a Large Eddy Simulation (LES) of a normally impinging slot jet flow at three Reynolds numbers, $\mathrm{Re}_B = 3000$, 7500, and 13 500, at a fixed nozzle-to-plate spacing of $H/B = 10$. A weak dependency between the Reynolds number and the potential core length is found for $3000 < \mathrm{Re}_B < 7500$ by examining the streamwise velocity along the jet centreline, with the potential core approaching an asymptotic value of $4B$ above $\mathrm{Re}_B = 7500$. No significant trends are observed between Re_B and the jet halfwidth. The numerical velocity field data compares well to the experimental data presented by Maurel & Solliec [59] for $\mathrm{Re}_B = 13500$. Similar observations are made by Medina *et al.* [13] for the streamwise velocity profile at the jet centreline at for a normally impinging round jet with $\mathrm{Re}_D = 3900$, 6290, 9200, and 10 000 and a nozzle-to-plate spacing of $H/D = 3$. However, differences in the vorticity and turbulent kinetic energy fields are apparent between the various Reynolds numbers in [13, 59]. As the Reynolds number is increased, the instabilities in the shear layer breakdown to turbulent eddies [13]. The growth of the eddies increases the magnitude of the fluctuations and consequently alter the turbulent kinetic energy field. The turbulent kinetic energy values in the mixing layer increases with increasing Reynolds number, but shows a decrease at the start of the wall jet region due to the earlier onset of vortex breakdown [13]. Xu & Hangan [14] examined the effect of the Reynolds number within the range of $23\,000 < \mathrm{Re}_D < 190\,000$ for various nozzle-to-plate spacings ($H/B = 1$, 2, 3, and 4) on a normally impinging round jet. When $\mathrm{Re}_D > 27\,000$, the time averaged radial velocity profiles at $r/D = 1$ are found to be insensitive to changes in Re_D, for all nozzle-to-plate spacings. Overall, the Reynolds number effects are not observed in time averaged velocity measurements, but the coherent structures that form in the mixing layer are sensitive to the jet Reynolds number, which consequently affects the turbulence statistics.

The nozzle-to-plate spacing, H, determines the type of impingement. The placement of the impingement surface beyond the end of the potential core length creates transitional impingement; an additional region of velocity decay is observed beyond the length of the potential core, where the mixing layer has grown to its maximum size [37, 60]. By placing the surface within the length of the potential core, the decay region is suppressed; the latter type of impingement is named potential core impingement. Narayanan *et al.* [37] employed single-component LDA to examine the effect of the nozzle-to-plate spacing for a normally impinging slot jet at $\mathrm{Re}_B = 23\,400$ and $H/B = 1$ and 7, which corresponds to potential and transitional impingement, respectively. The main findings indicated that the turbulent stresses increased in the wall jet region ($x/B > 1.5$) at $H/B = 1$, while the time-averaged velocity profiles also showed a higher maximum in the same region. At very low nozzle-to-plate spacings (within a nozzle diameter or width), the flow field of an impinging jet is likened to that of Homann flow [61]. Liu & Sullivan [62] found that at a nozzle-to-plate spacing of 1.125 and a Reynolds number of 12 300, the potential core of the free jet region persists at downstream radial locations up to 1.4 nozzle diameters and the magnitude of the wall jet thickness has matching order with that of the inviscid axisymmetric impinging jet.

2.2.1 Free Jet and Stagnation Regions

The free jet region of an impinging jet consists of the same two characteristic regions observed in a free jet: a shrinking potential core and a widening mixing layer. The difference in impinging jet flow is that the development of the free jet region is dependent on the type of impingement; that is the distance between the nozzle exit and the impinging surface. The nozzle-to-plate distance determines the interaction between the impingement surface and the potential core of the jet. The potential core length definition is widely accepted to be the distance from the jet exit to where dynamic pressure is 95 % of the initial average dynamic pressure for impinging jets [57, 60, 63]. In transitional impingement, the axial velocity decay is governed by the hyperbolic law according to Reichardt [64]. Experimental correlations for the jet width and velocity decay is summarized by Martin [65]. Furthermore, the free jet region behaves much like a normal free jet (Section 2.1), as the effect of the surface does not propagate into the upstream flow field. When the distance between the jet exit and the surface is larger than the vortex formation length, the flow field is only weakly dependent on changes to the distance between the jet exit and the wall [14]. In potential core impingement, the decay region is not observed and the fully developed free jet region may also not be present, if the nozzle-to-plate spacing is less than two nozzle widths [60]. In this configuration, the impinging surface affects the upstream flow conditions due to the high static pressure in the stagnation region [29, 34, 60].

The stagnation region is defined by a region of fluid with near zero velocity magnitude and fluctuations; it is centred about the intersection between the jet centreline and the impingement surface. According to Popiel & Trass [21] and Martin [65], the stagnation region extends a distance of $1.2D$ normal to the wall for a round jet, whereas Cooper *et al.* [26] define it to be $2D - 3D$ above the surface. In accordance with the latter, Fitzgerald & Garimella [66] report a value of $1.5D$ for the height of the stagnation region. Others have used the nozzle-to-plate spacing as an alternative length scale for describing the stagnation region. For a slot jet, Maurel & Solliec [59] define the stagnation region height as $0.13H$ by intersecting two linear sections (decay region and stagnation region) of axial velocity along the jet centreline for a range of nozzle-to-plate spacings. The height was found to be independent of Reynolds number and the nozzle width. Comparatively, in an earlier study by Gutmark *et al.* [67], the impingement region is found to affect an area that extends $0.25H$ normal to the surface for a plane impinging jet. Additionally, the turbulence characteristics also change from equilibrium levels at a height of $0.15H$. The stagnation point is easily identifiable through velocity and pressure measurements as a near zero velocity region or location of highest pressure at the wall, respectively. However a universal definition regarding the extent of the stagnation region in impinging jet flows has not yet been reached.

2.2.2 Wall Jet Region

As shown in Fig. 2.3, the final region associated with impinging jet flows is a wall jet region. The wall jet region will form at any angle of impingement, with its origin at the stagnation point. However, the effect of the nozzle-to-plate spacing was found to be negligible in the wall jet region, outside the potential core impact region ($r/D > 3$), of a round jet for

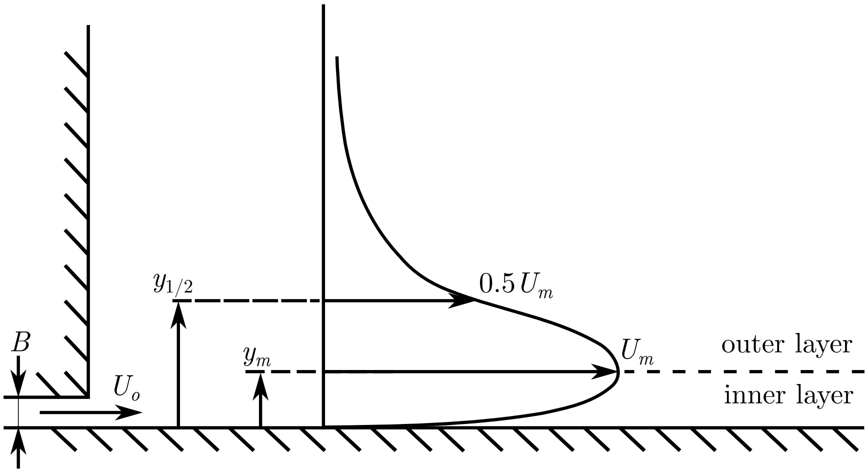

Figure 2.3: Composition and nomenclature of a turbulent planar wall jet.

Reynolds number range of 8500 to 23 000 [66]. For a tangential wall jet, where the jet is issued into quiescent air parallel to the surface, the origin is virtual, located upstream of the exit of the nozzle [68]. Figure 2.3 shows a schematic and relevant parameters of a typical planar wall jet. Two distances and corresponding velocities are typically defined to describe the scale of the wall jet. U_m is the maximum velocity and y_m is the wall normal distance where the maximum velocity occurs. Following the same convention, another wall normal distance, $y_{1/2}$, is defined where the velocity is half of the maximum velocity. Glauert [69] presents one of the first fundamental analyses regarding laminar wall jets, wherein he finds a similarity solution for the wall jet velocity profile, as well as an integral momentum flux relation. He then extends the analysis of the laminar wall jet to give form to the turbulent wall jet by the introduction of an eddy viscosity [69]. The turbulent wall jet consists of two regions separated by the maximum velocity as shown in Fig. 2.3: the near wall inner layer where the effect of the wall is prominent, and an outer layer, which behaves as a free shear layer [54, 70, 71]. The inner layer is dominated by small turbulence scales and behaves similar to a typical boundary layer flow, while the outer layer consists of large turbulence scales [70].

A parameter that is used to characterize the wall jet is the growth rate or the spread rate, defined as the rate of change of the half width along the streamwise direction: $dy_{1/2}/dx$. Launder & Rodi [54] quantify the spread rate for a plane and radial turbulent wall jets to be 0.073 ± 0.002 and 0.090 ± 0.005, respectively, with weak dependence on the jet configuration. In contrast, Eriksson *et al.* [72] report a slightly higher growth rate of 0.078 and Rostamy *et al.* [70] report a value of 0.0791, for the plane wall jet. For a wall jet created using an axisymmetric impinging jet, Cooper *et al.* [26] and Fairweather & Hargrave [73] report growth rates of 0.07 and 0.076, respectively. These results disagree with the findings by

Knowles & Myszko [74], who provide a comprehensive list of growth rates of the wall jet region between 0.0823 and 0.1091, which they created using an impinging jet with various nozzle-to-plate spacings ranging from 2 to 10.

The evolution of the wall jet is facilitated by the momentum supplied by the upstream flow. Additionally, the presence of a steady recirculation zone which rejuvenates the initial formation of the wall jet has been suggested [73]. The recirculation zone, with a length scale of about $40D$ and a non-dimensional time period of $t^* = tU_o/B = 7.22 \times 10^3$, is observed beyond $10D$ from the stagnation point as a region of low negative velocities in the outer layer of the wall jet. The time, t, is the time period of recirculation. In the inner region, U_m reaches a maximum value approximately one jet diameter (or width) away from the stagnation point and decays as the turbulent wall jet is formed beyond three jet diameters (or widths) [24, 25, 62, 66]. The far field wall jet region, beyond four to five nozzle diameters (or widths) is not typically studied in detail. The experimental work by Fairweather & Hargrave [73] is one of the few to measure velocities in the far field wall jet region, up to $r/D = 30$, using PIV at $\mathrm{Re}_D = 18\,800$ and $H/D = 2$. At streamwise locations greater than $r/D = 5$, self similarity in mean velocity components, root mean square (RMS) fluctuating velocities, and Reynolds shear stress is observed [73].

A wall jet flow produced by a nozzle parallel to the surface exhibits unsteady separation prior to transition to turbulence [71]. A similar unsteady separation is observed in the wall jet region produced by an impinging jet in both numerical and experimental work. In a large-eddy simulation (LES) conducted by Hadžiabdić & Hanjalić [19] for a normally impinging round jet at $\mathrm{Re}_D = 20\,000$ and $H/D = 2$, flow separation and reversed flow in the inner region is observed near $r/D = 2$. Comparatively, for a round impinging jet flow that is acoustically excited upstream of the jet exit, Didden & Ho [75] observed flow separation around $r/D = 1.1$ for $\mathrm{Re}_D = 19\,000$, $H/D = 4$, and an excitation frequency of $f_e = 70$ Hz, which corresponds to a non-dimensional frequency of $St_e = f_e D/U_o = 0.35$. At smaller nozzle-to-plate distances of $H \leq 2D$, $\mathrm{Re}_D = 12\,300$, and excitation frequencies of $St_e = 0.8$ and 1.46, flow separation occurs at around $1.3 < r/D < 1.75$ [62]. For an unexcited impinging jet at small nozzle-to-plate spacings of $H \leq 2D$ and $\mathrm{Re}_D = 10\,000$, flow separation develops around $1.0 < r/D < 1.2$ [16]. Additionally, Landreth & Adrian [76] found that the separation point is located around $x/D \approx 2$ for $\mathrm{Re}_D = 6564$ and $H/D = 4$. The location of this unsteady separation is found in the region where the wall jet is decelerating and is characterized by a thickening of the boundary layer, near zero shear stress, and vorticity maximum that is opposite in sign to the vorticity in the mixing layer of the free jet region [19, 75, 76]. Didden & Ho [75] extends this discussion to include the pressure gradient in the region of flow separation ($r/D = 1.1$). They note that an adverse pressure gradient is found prior to the point of flow separation ($r/D = 0.9$), which then reaches a maximum immediately after separation ($r/D = 1.2$). They conclude that the unsteady pressure gradient is caused by the passage of vortices in the outer region of the wall jet rather than the separation itself.

2.3 Vortex Dynamics in Impinging Jet Flows

The mixing layer, as shown in Fig. 2.2, initiates at the exit of the nozzle, where the high momentum fluid comes into contact with the nearly stagnant ambient fluid. Due to the velocity difference between the jet and the ambient fluid, the free shear layer is inviscidly unstable, as initially proven by Kelvin [42] following the hypothesis by von Helmholtz [43], commonly referred to as the Kelvin-Helmholtz instability. In parallel shear flows, the velocity ratio is defined as $R = \Delta U / 2\bar{U}$, where ΔU is the velocity difference between the two flows and $\bar{U}$ is their average velocity [77]. In the mixing layer of impinging jets, the ambient air has near zero velocity and the velocity ratio R approaches unity. Terra-Homem & Erdélyi [77] found that a critical velocity ratio exists, where parallel flows with $R < 1.315$ are convectively unstable. In accordance with this discovery, the Kelvin-Helmholtz instabilities describe a convective amplification of perturbations in impinging jet flow as shown in Fig. 2.4.

The amplification of unstable disturbances that initiate at the nozzle exit, leads to shear layer roll-up and formation of vortices, referred to as primary vortices, as shown by the

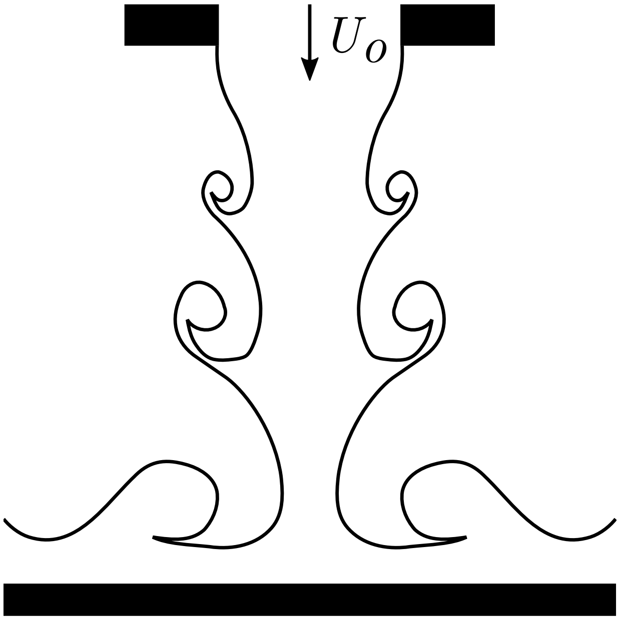

Figure 2.4: Vortex formation due to growth of Kelvin Helmholtz Instability adapted from the flow visualization by Popiel & Trass [21].

exceptional flow visualization experiments by Popiel & Trass [21]. A high aspect ratio nozzle exit produces vortices that are elongated in the spanwise direction and the behaviour of the vortices model two dimensional rollers. The natural frequency of the shear layer roll-up is characterized by the Strouhal number $St = fL/U_o$, where f is the frequency of the vortex roll-up, L is a characteristic length defining the nozzle based on the geometry, and U_o is the characteristic velocity. For round and plane jets, nozzle diameter D, or nozzle width B, is used as a length scale to obtain St_D or St_B, respectively. The natural frequency is dependent on Reynolds number, initial velocity profile, turbulence state at the nozzle, and nozzle-to-plate distance; thus, a range of Strouhal numbers have been reported in literature for various jet configurations [19]. Sodjavi *et al.* [17] found that the vortices are shed at $\mathrm{St}_D = 0.57$ for a round jet at $\mathrm{Re}_D = 5620$ and $H/D = 2$ using PIV, which matched the highest frequency at the impinging surface measured by electrodiffusion in the same experimental setup. A shedding frequency of $\mathrm{St}_D = 0.72$ has been reported by Violato *et al.* [8] for $\mathrm{Re}_D = 5000$ and $H/D = 4$. In the numerical investigation by Tsubokura *et al.* [78], a distinct unstable mode associated with vortex shedding is found at $\mathrm{St}_D = 0.37$ for a round jet, while the plane jet exhibited an unstable mode at $\mathrm{St}_B = 0.44$, with both jets at $\mathrm{Re}_B = \mathrm{Re}_D = 6000$ and $H/B = H/D = 10$. The coherent structures are convected downstream by the mean flow at approximately half the jet core velocity and are seemingly insensitive to the jet configuration [8, 12, 79].

Downstream of the formation, vortex merging events are observed, where the mechanism of merging is similar to that of the free jet [8, 80]. As Roux *et al.* [22] observed for a round jet, the primary vortices with a shedding frequency of $\mathrm{St}_D = 1.2$ merge producing a vortex with a characteristic frequency equivalent to that of the preferred mode of a round jet ($\mathrm{St}_D \approx 0.3$) [35, 81]. In contrast, others have shown that the characteristic frequency of the merged vortex is not strictly equivalent to the frequency of the preferred mode, but is half of the formation frequency [8, 16, 23].

The merging process of two vortices is divided into four stages [82, 83]. In the first stage, vortices diffuse due to viscosity, increasing in diameter a, while remaining at a constant separation distance b. Once a critical core-to-separation distance is attained, the two vortices become unstable and deform, then begin to merge in the convective stage marked by the consolidated vorticity fields. Through this stage, the two vortices maintain two distinct maxima of vorticity with a rapidly decreasing separation distance. The third stage is identified by the emergence of a singular vorticity maximum. At the onset of merging, thin filaments of vorticity form at the outer edges of the vortices, which then spiral around the outer edge of the merged vortex [82]. The last stage is the diffusion of the single merged vortex, where the process restarts with another nearby vortex, as observed in many shear flows. By using consistent scaling factors for the vortex core size, the critical distance ratio $(a/b)_c$, where the vortex pair merges, collapses to 0.22 [83]. Comparable values of critical distance ratios using various scalings are reported in the literature for both numerical and experimental studies pertaining to co-rotating vortices, where there is no background flow [82, 84, 85]. In impinging jet flows, where there is a significant mean flow, the merging process of two vortices is different to that of the merging of a co-rotating vortex pair. However, the merging process outlined here provides a basis for understanding the merging process of vortices in impinging jets.

The passage of primary vortices in the wall jet outer shear layer induces the formation of a secondary vortices with opposing signs of vorticity at the wall, as seen in Fig. 2.5. The formation of the secondary vortices is reported in a wide variety of impinging jet configurations using experimental techniques such as particle image velocimetry, laser doppler velocimetry, hot wire anemometry, and surface pressure measurements [12, 17–19, 24, 25, 62, 75, 76, 86]. Secondary vortex formation has also been observed in plane wall jet flows, with the formation process following a similar mechanism to that of the impinging jet secondary vortex [71]. The passing of the primary vortices leads to the presence of strong adverse pressure gradients, which decelerate a thin fluid layer at the wall that subsequently rolls up to form secondary vortices [19, 75]. As discussed in Section 2.2.2, the onset of unsteady flow separation near $x/B = r/D \approx 1$ to 2 marks the formation of the secondary vortex. Although the secondary vortex has been observed in numerous studies, not many have tried to characterize the dynamics of secondary vortices and their interactions with primary vortices. For a jet configuration of $\mathrm{Re}_D = 19\,000$ and $H/D = 4$, Didden & Ho

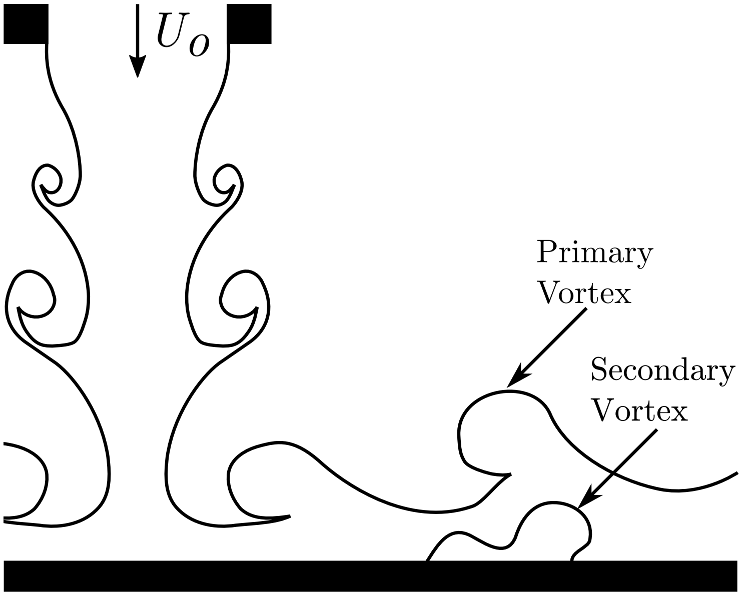

Figure 2.5: Schematic of secondary vortex formation at the wall due to passing of primary vortices adapted from the flow visualization by Popiel & Trass [21].

[75] determined that the the secondary vortex is convected downstream at a constant convective speed of $0.72U_o$, which is higher than the convective velocity of the primary vortex, $0.6U_o$. However, Hall & Ewing [12] found that the convective velocity of the primary vortex decreased in the wall jet region due to the secondary vortex. The ejection of the secondary vortices from the surface leads to coupling with the primary vortices, which initiates the breakdown of the planar structures into turbulence [21, 75, 76].

Chapter 3

Experimental Methodology

In the present study, the fluid dynamics of a normally impinging planar air jet is experimentally investigated in a specialized jet facility, with particular focus on vortex dynamics. Flow field measurements are collected for two Reynolds numbers, $\mathrm{Re}_B = 3000$ and 6000, and two nozzle-to-plate distance ratios, $H/B = 2$ and 4, to quantify the effect of the jet configuration on the flow topology. The centreline velocity, U_c, is used as the characteristic velocity, U_o, at the jet exit. Particle image velocimetry (PIV) is used to characterize the development of the planar jet and the coherent structures. This chapter describes the experimental setup and the measurement techniques that are employed during the current investigation.

3.1 Experimental Setup

Experiments are performed in the newly commissioned jet facility, seen in Fig. 3.1, at the University of Waterloo. The jet facility is designed and fabricated as part of the current work, which included extensive testing, modification, and validation prior to the maiden experimental campaign. The jet facility is a miniaturized open loop blower-type wind tunnel designed to be configurable for studying normally impinging jet flows, oblique jets, wall jets, and free jets. As seen in Fig. 3.1, there are four major components that make up the jet facility: a structural frame, the jet nozzle assembly, the impinging plate, and a blower. Both the jet nozzle assembly and the impinging plate are mounted in a cubic aluminum frame measuring 1 m^3, for ease of alignment and stability during operation without blocking optical access. The structural frame also serves to adjust the alignment of the jet nozzle assembly and the impinging plate, while providing rigidity to the facility. The impinging surface, measuring $50B \times 63B$, is made from a precision machined cast aluminum plate

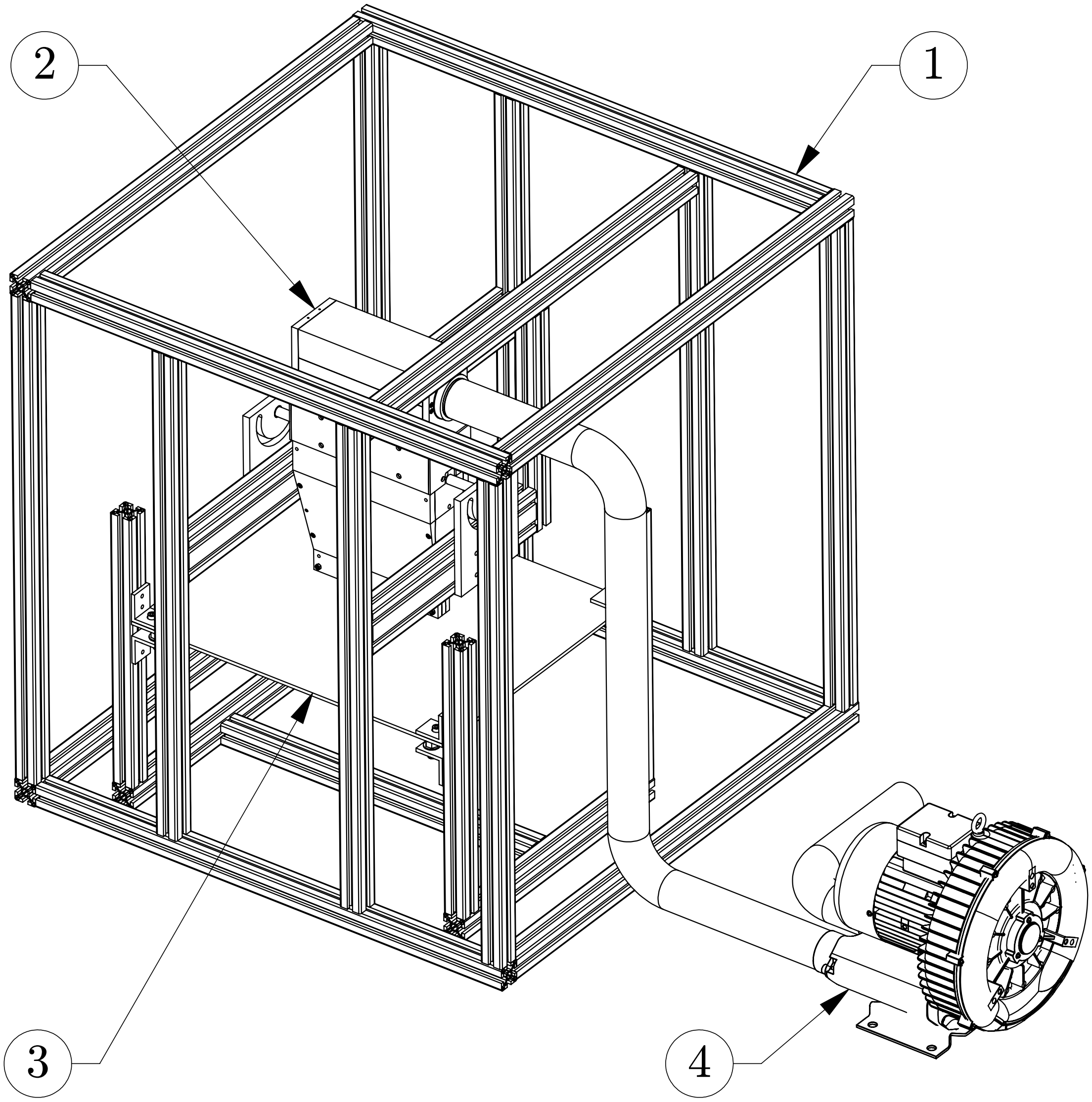

Figure 3.1: Jet facility used in the current investigation. ① Structural frame; ② jet nozzle assembly; ③ impinging plate; ④ regenerative blower.

to ensure a consistent surface finish with smoothness of 0.5 µm and a maximum flatness deviation of 0.381 mm. A decorative black dye coating is applied through anodization to minimize light reflections.

Air is supplied by a regenerative blower (ring compressor), which is controlled by an Allen-Bradley variable frequency drive that also monitors the rotational speed of the blower impeller. A gate valve is installed at the intake of the blower to act as a throttle, allowing control of the flow velocity while operating the blower at a constant impeller rotational speed. It is necessary to control the flow rate independently of the impeller rotational speed, as the blade-pass frequency affects the behaviour of the coherent structures downstream by acting as a source of forced excitation. By using a higher impeller rotational speed, the blade-pass frequency can be shifted into a frequency range of $\mathrm{St}_B > 1.25$, which is greater than the frequencies of interest, $\mathrm{St}_B \leq 0.5$.

The air supplied by the blower is directed through a flexible hose to the inlet of the jet nozzle assembly, leading to a plenum and settling chamber section. Figure 3.2 shows the jet nozzle assembly and internal components of the plenum and settling chamber. The plenum section contains a flow distribution tube used to distribute the flow evenly across the span of the nozzle. The tube has three sets of azimuthal holes with varying diameters along its span and a separation angle of 60°, which are aimed at the top of the plenum. The top of the plenum is shaped as a half cylinder, coaxial to the flow distribution tube. This configuration of the tube allows the flow to be directed downward towards the settling chamber after mixing in the top part of the plenum. The use of a flow distribution tube offers a more compact solution compared to the traditional method of placing a diffuser ahead of the settling chamber [87]. A similar design is used by Hassaballa & Ziada [88] and Arthurs & Ziada [89] for studying self-excited oscillations in jets at speeds of $\mathrm{Ma} > 0.4$.

The production of the settling chamber and the contraction relies heavily on the design guidelines outlined by Mehta & Bradshaw [87] and Bradshaw & Pankhurst [90] for low speed wind tunnels. As seen in Fig. 3.2, the settling chamber section consists of a honeycomb screen and four mesh screens that improve flow uniformity and reduce velocity fluctuations in the incoming flow. The cell length-to-diameter ratio of the hexagonal honeycomb structure is 8.7, which is comparable to the suggested optimal range of 6-8 [87]. Two different pairs of steel mesh screens are used downstream of the honeycomb as seen in Fig. 3.2, with open area ratios, β, of 0.68 and 0.70, due to availability. The screens with the larger open area ratio are placed downstream of the screen with the smaller open area ratio. The open area ratios of the screens are greater than the minimum of 0.57 suggested by Bradshaw & Pankhurst [90] for attenuating the growth of disturbances due to flow instabilities.

After the flow passes through the settling chamber and the series of flow conditioning elements, it enters the contraction section. The contraction has a total length of $L_c = 0.25$

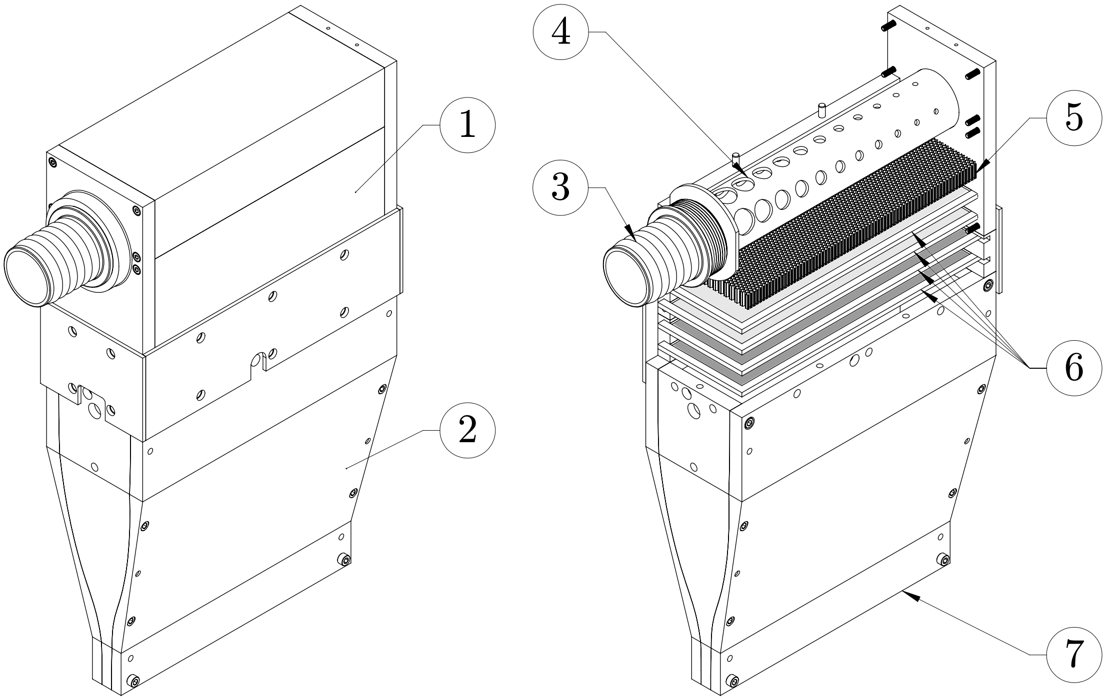

Figure 3.2: Jet nozzle assembly and flow conditioning elements. ① Plenum and settling chamber; ② contraction and nozzle exit; ③ inlet; ④ flow distribution tube; ⑤ honeycomb; ⑥ steel mesh screens (light gray and dark gray indicates $\beta = 0.68$ and 0.7, respectively) ⑦ rectangular nozzle outlet.

m, with smooth profiles for each internal surface created using two cubic profiles, connected with matching gradients at a point located $0.72L_c$ downstream of the contraction inlet. The profiles are machined using a Computer Numerical Control (CNC) mill in order to maintain a good surface finish and high tolerances. The contraction has an inlet-to-outlet area ratio of 9:1, which further homogenizes the flow conditions at the exit, while also increasing the speed of the flow. The rectangular profile of the contraction exit, which measures 10 mm in width (B) and 200 mm in span (L), is extended 38.10 mm beyond the length of the contraction in order to further reduce non-uniformities, as suggested by Mehta & Bradshaw [87]. This section is comparable to the test section that follows the contraction in the traditional design of a wind tunnel.

The facility is calibrated and characterized prior to the start of the main experimental campaign; details of the process are provided in Appendix A and summarized here. Calibration and characterization is completed in a free jet configuration, where the jet nozzle assembly is rotated 90° about its centre of mass in order to allow the jet to spread without interference from the surroundings. Two different Cartesian coordinate systems are used for each jet configuration, as seen in Fig. 3.3, which follows the convention in the literature for each type of jet. In a free jet, the coordinate system origin is placed at the centre of

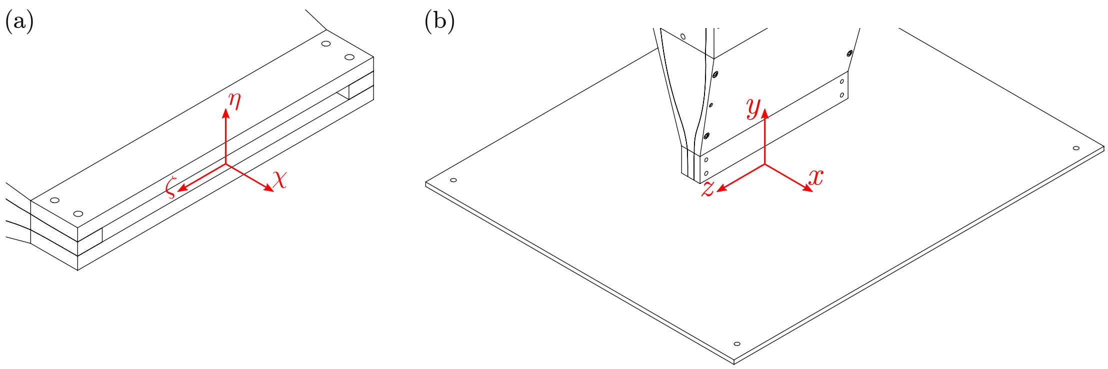

Figure 3.3: Coordinate system. (a) Free jet configuration with the origin at the centre of the nozzle exit and (b) impinging jet configuration with the origin at the geometric stagnation point on the impinging surface.

the nozzle exit. In the impinging jet configuration, the coordinate system is attached to the impinging surface, with the origin placed at the geometric stagnation point. Along the spanwise centreline, a uniformity of ±0.5% for 95% of the nozzle span is measured using a Pitot-static tube positioned at the nozzle exit. The Pitot-static tube has an inner diameter of 1.5 mm and is mounted on a three axis traverse with a translational resolution of 0.005 mm, which allows for precise alignment of the Pitot tube to the nozzle exit. A linear calibration fit is obtained between the static pressure drop across the contraction and the dynamic pressure at the center of the nozzle, as measured by the Pitot-static tube used for assessing spanwise uniformity. Based on the calibration, the jet centerline velocity has an associated relative uncertainty of less than 6.7%. During operation of the facility, the blower and jet nozzle assembly has a warm up period, where the outlet flow temperature increases before reaching a constant value. Consequently, in order to correctly set the Reynolds number of the jet, the flow temperature at the exit is measured using a Type-K thermocouple, which has a standard accuracy of ±0.75%. The flow temperature is allowed to stabilize with a warm up period of approximately one hour, during which the temperature is measured every five minutes. The same procedure is followed during the experimental campaign, with a warm up period observed after changing the Reynolds number.

Hot wire anemometry is used to assess the streamwise turbulence characteristics in the free jet configuration. The hot wire system is calibrated in the jet facility, which is susceptible to temperature variation as the speed of the facility is changed. Therefore, the temperature correction method outlined by Hultmark & Smits [91] is applied, which uses similarity variables for velocity and voltage to produce a single calibration curve valid for different temperatures:

$$\frac{U}{\nu} = f\left(\frac{E}{k\Delta T}\right). \tag{3.1}$$

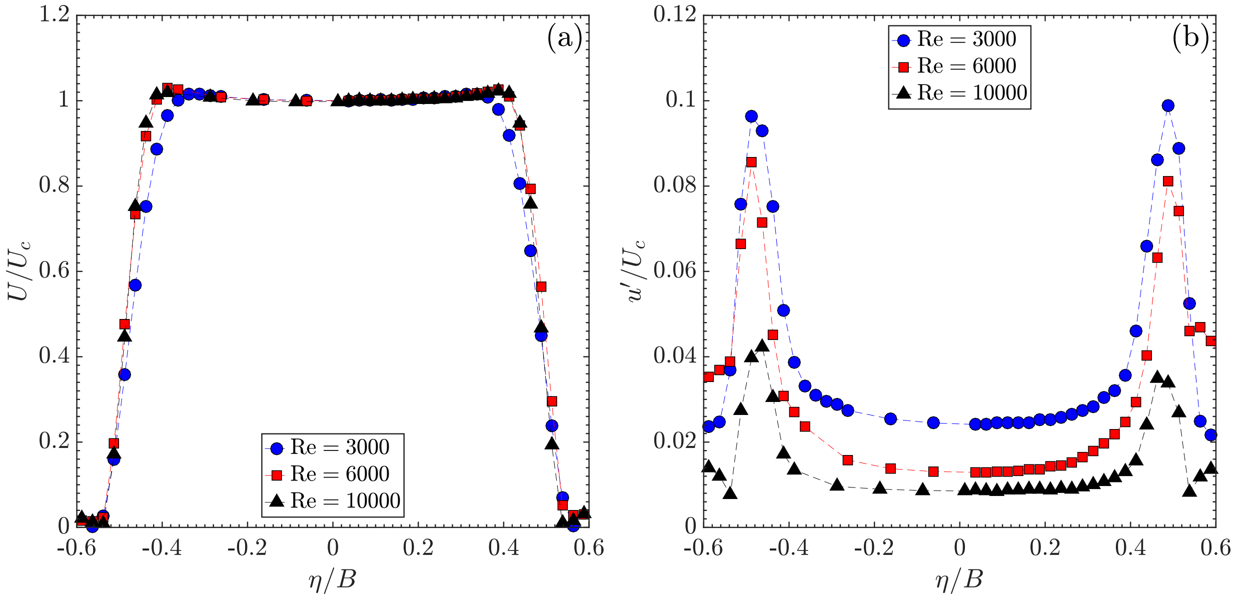

Figure 3.4: Profiles of normalized streamwise (a) velocity and (b) turbulence intensities along the transverse direction measured using Hot Wire Anemometry in the free jet configuration.

Streamwise velocity (U) is normalized by the kinematic viscosity (ν). Voltage (E) is normalized by thermal conductivity of air (k) and the temperature difference (ΔT) between the hot wire temperature and the flow. Figure 3.4 shows the streamwise velocity profile and the turbulence intensity measured at the mid-span, $0.5B$ downstream of the nozzle exit, for $\mathrm{Re}_B = 3000$, 6000, and 10 000. The profiles are normalized by the centreline velocity, U_c. The desired "top-hat" velocity profile is seen with a transverse uniformity of ±2% for all Reynolds numbers tested in Fig. 3.4a. Flow acceleration is observed in the shear layers of the jet indicated by the higher velocities in the shear layer, when compared to velocity at the center of the jet. The local flow acceleration in the shear layers of the jet is attributed to the jet-nozzle interaction in converging nozzles [17]. Figure 3.4b shows that turbulence intensity in the region $-0.35 < \eta/B < 0.35$ is less than 2% of U_c for $\mathrm{Re}_B = 3000$ and 6000, while the profile for $\mathrm{Re}_B = 10\,000$ shows that the turbulence intensity is less than 4% of U_c for $-0.4 < \eta/B < 0.4$. The turbulence intensities in the mixing layer and the potential core near the nozzle exit of the slot jet in the current study match well with previous studies that examined round free jets for similar Reynolds numbers [31, 32, 34].

3.2 Particle Image Velocimetry

Time resolved, planar PIV is utilized to capture two components of velocity in an impinging jet flow. The reader is directed to the works by Westerweel *et al.* [6], Adrian & Westerweel

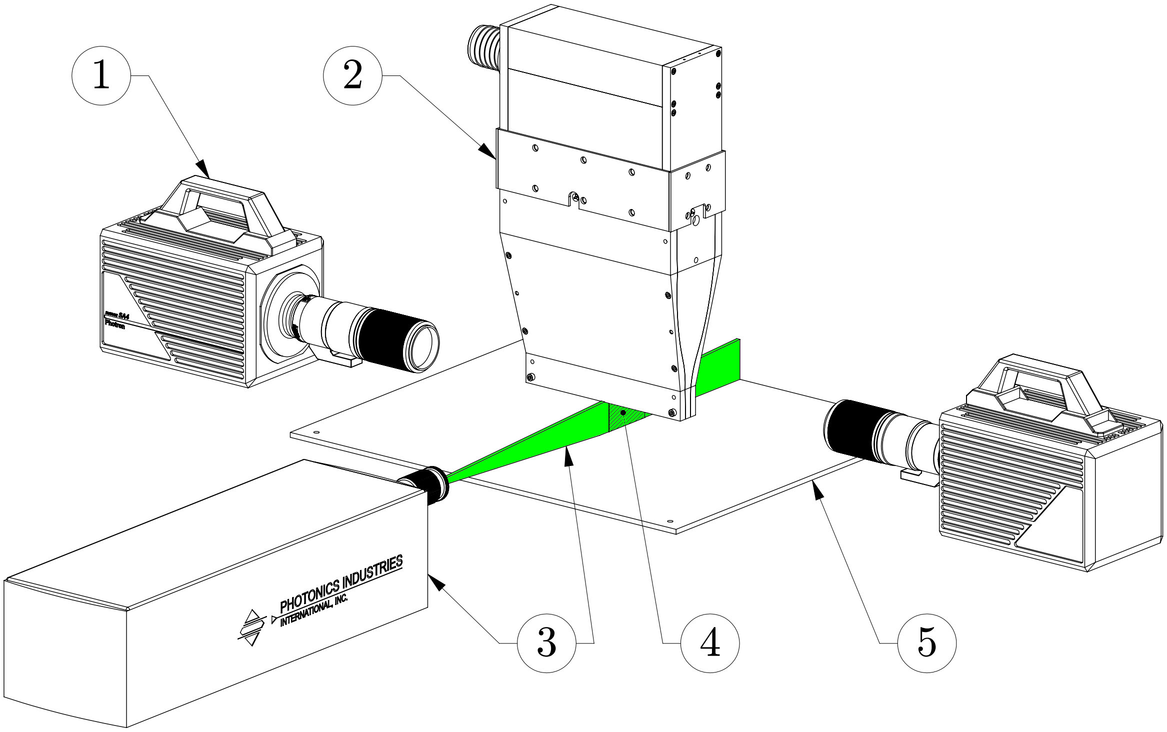

Figure 3.5: Optical equipment configuration for velocity measurements using PIV. The nozzle is oriented normal to the impinging plate. ① High speed camera; ② jet nozzle assembly; ③ laser system and beam; ④ field of view; ⑤ impinging plate.

[92], Prasad [93], and Willert & Gharib [94] for details on the operating principles and evolution of the method in the last quarter century. The general arrangement of the optical imaging equipment shown in Fig. 3.5 is used for both $H/B = 2$ and 4 configurations. The jet nozzle assembly is oriented such that the jet impinges normally and a laser sheet is projected across the mid span of the nozzle. The laser beam is produced by a Photonics DM20-257 Nd-YLF dual pulsed laser and a sheet is created by a LaVision focusing lens and a concave lens placed in the path of the laser beam. The laser is placed on a manually adjustable heavy duty lab jack, allowing for precise vertical alignment of the laser sheet. The laser is positioned at a distance greater than $63B$ from the jet mid span centreline, beyond the edge of the impinging surface, in order to avoid any flow blockage. The flow is seeded with glycol-water based particles with mean diameters of 1 µm. As the seeding cannot be sufficiently recirculated due to rapid dissipation into the surroundings, the enclosure where the experimental facility resides is seeded prior to recording every set of particle images.

Two Photron SA4 high speed cameras, with a full sensor size of 1024×1024 px^2 each, are placed successively downstream on opposite sides of the laser sheet. Doing so allows for the field of view (FOV) of the cameras to be overlapped without the use of an optical adapter. The upstream camera captures the free jet and stagnation region, while the downstream camera captures the wall jet region. The cameras are mounted on heavy duty optical rails that allow for translation of the cameras in all three axes and a mount that rotates about two axes. Each camera is equipped with a 105 mm fixed focal length Nikon lens, set to its maximum numerical aperture of $f_{\#} = 2.8$. Figure 3.6 shows the coordinate system and FOV arrangement for the two flow configurations of $H/B = 2$ and 4. Note that the coordinate system origin is placed where the centreline orthogonally intersects the impinging surface, with x and y directed parallel and normal to the impinging surface, respectively. For $H/B = 2$, a combined FOV of $7.5B \times 2B$ is imaged with a magnification factor of $M = 0.4$ for both cameras. Each camera sensor is cropped to 896×512 px^2, resulting in an approximate FOV of $4B \times 2B$ per camera and a lengthwise overlap of 12.5%. For $H/B = 4$, the sensor is cropped to 640×640 px^2 and the cameras are repositioned to capture the extended nozzle-to-plate spacing, resulting in a new magnification factor of $M = 0.32$ and an approximate FOV of $4B \times 4B$ for each camera. The combined FOV is $7.5B \times 4B$, with a lengthwise overlap of 12.5%.

The choice of the cropped sensor sizes factors into the trade off between maximizing spatial resolution, acquisition frequency, and the illumination power. The chosen sensor sizes allow image acquisition at $f_s = 3200$ Hz, which is 6 times the maximum vortex shedding frequency detected using hot wire anemometry. At this frequency, 6656 image pairs are collected with sufficient temporal resolution to capture the behaviour of the coherent structures. In order to obtain uncorrelated velocity fields for improved statistical convergence of time-averaged properties, low-repetition rate data acquisition is also performed at $f_s = 125$ Hz to obtain 5000 image pairs. The added benefit of operating at a lower acquisition

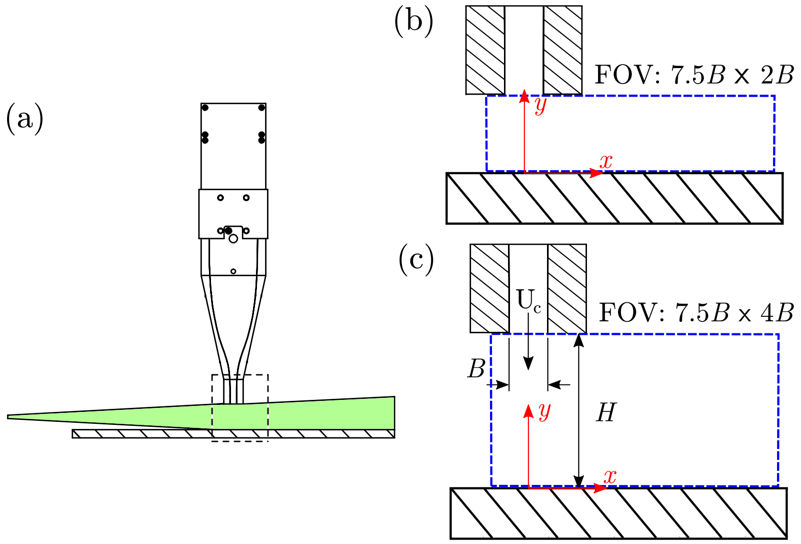

Figure 3.6: Schematic of PIV setup. (a) Side view of laser sheet along with FOV of (b) $H/B = 2$ and (c) $H/B = 4$.

frequency is that the laser power is increased per pulse, which improves the quality of the particle images. All images are captured in double-frame mode at the two frequencies specified. The frame separation time (Δt) is chosen for each flow configuration in order to maintain a consistent particle displacement (Δs) in the jet potential core. The frame separation times and the particle displacement in the jet potential core for each set of flow conditions are summarized in Table 3.1.

For each nozzle-to-plate height ratio, the cameras are calibrated using a calibration target grid with 0.01 mm grid spacing and common reference points in the overlap region, verified to be visible to both cameras. Additional reference points are also used for each respective FOV. The calibration target is placed parallel to the laser sheet, such that the laser sheet illuminates the target surface for one camera. Alignment of the target is achieved by using the external machined surface of the nozzle as a datum and a mounting surface. Once the first camera is calibrated, the calibration target is shifted spanwise along the datum, such that the laser sheet illuminates the other side of the calibration target. Once the second camera is focused on the calibration target, the calibration scaling is applied in DaVis 8. The focus is adjusted by a small increment to capture particles with an imaged diameter of approximately $2-3$ px for both cameras.

The illumination and imaging equipment are synchronized using a LaVision high speed controller and DaVis 8 software, with the latter also being used for processing of particle images. The particle images are preprocessed by applying a sliding minimum subtraction with a image kernel size of 51. Intensity normalization is also applied to offset the difference in the illumination for each frame, which is inherent to the laser. The impinging surface and areas of low light at the top edges of the light sheet are excluded from processing by applying a mask. The particle images are processed to produce velocity fields by implementing a multi-pass, sequential cross correlation algorithm with a decreasing window size. A final window size of 16×16 px^2 with 75% overlap is used for both nozzle-to-plate heights, which results in a vector pitch of $0.018B$ for $H/B = 2$ and $0.026B$ for $H/B = 4$.The instantaneous vector fields from each camera are aligned and stitched together by using the imaged impinging surface as a reference. Cross correlation in the overlap region is also used to verify the stitching of the vector fields. The velocities in the overlap region are blended using a cosine weighted function, in order to minimize undesirable artifacts at the edges of the FOV from each camera. The uncertainty in the relevant regions of the instantaneous velocity fields, calculated by PIV, is estimated to be $\pm 6\%$ of U_c, for both nozzle-to-plate spacings. For full details of the uncertainty analysis, refer to Appendix B. A summary of the PIV parameters that are detailed in this section are presented in Table 3.2.

Table 3.1: Frame separation time and particle displacement.

	$H/B = 2$		$H/B = 4$	
	$Re_B = 3000$	$Re_B = 6000$	$Re_B = 3000$	$Re_B = 6000$
Δt [µs]	80	35	100	50
Δs [px]	10	10	9	9

Table 3.2: PIV experimental parameters.

Parameter	$H/B = 2$	$H/B = 4$	Unit
Laser	Photonics DM20-527 Nd-YLF		
Camera(s)	2 × Photron SA4		
Lens focal length	105		mm
Lens aperture	2.8		
Magnification	4		
Sensor size per camera	896 × 512	640 × 640	px^2
Field of view	$7.5B \times 2B$	$7.5B \times 4B$	
Sample rate	3.2 *		kHz
	0.125 †		kHz
Samples	6656 *		
	5000 †		
Frame separation time	See Table 3.1		
Particle displacement			
Final Window size	16 × 16 (75% overlap)		px^2
Vector pitch	$0.018B$	$0.025B$	

* Data set used to capture time resolved behaviour
† Data set obtained for improved statistical convergence

Chapter 4

Results and Discussion

In this chapter, the results of experiments described in Chapter 3 are presented. Experiments are performed at $\mathrm{Re}_B = 3000$ and 6000 for two nozzle-to-plate distances, $H/B = 2$ and 4, resulting in four different combinations of jet flow conditions. Data recorded using planar PIV are analyzed to provide a description of the pertinent flow features of impinging jets. First, high speed flow visualization and time-resolved sequences of vorticity are used to describe the flow development and provide a qualitative description of the evolution of coherent structures in Section 4.1. In Section 4.2, the time-averaged quantities are used to characterize the effect of the nozzle-to-plate distance and the Reynolds number on the mean flow properties. Connections between the time-averaged quantities and the behaviour of the coherent structures are also established. Next, the quantitative analysis pertaining to coherent structure dynamics is presented in Section 4.3. Lastly, POD analysis is employed in order to extract information related to the most energetic coherent structures and is discussed in Section 4.4. In all field quantities, the region near the nozzle exit is excluded from the analysis (shown in grey in flow field contour plots) due to the low amount of illumination and reflections from the nozzle causing an excessive amount of erroneous vectors to appear. The excluded region accounts for approximately 25% of the nozzle-to-plate distance for both nozzle-to-plate height ratios.0.

4.1 Coherent Structure Evolution

In impinging jet flows, the Kelvin-Helmholtz instability that initiates in the free jet mixing layer gives rise to the shedding of coherent structures. The complex dynamics of these structures have been the focus of many studies [16–19, 21, 24, 25, 28, 95] due to their influence on local transfer properties, transition to turbulence, and the thermal field of

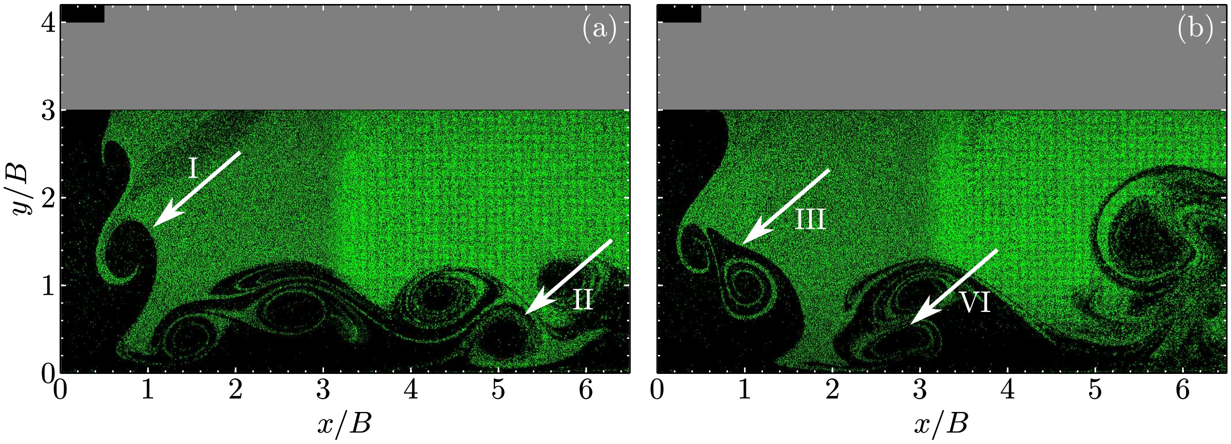

Figure 4.1: Flow visualization created by over seeding the ambient environment for $H/B = 4$ and $\mathrm{Re}_B = 3000$. The two frames are non-sequential and show (a) vortex formation and (b) vortex merging events. The nozzle is show in black and dark areas indicate unseeded jet flow.

impinging jet flows. The development of the coherent structures has been visualized previously by Popiel & Trass [21] and Cornaro *et al.* [34] by introducing smoke at the jet exit. In the present study, flow visualization images of the impinging jet at $H/B = 4$ and $\mathrm{Re}_B = 3000$ are created by over-seeding the ambient fluid (jet flow is unseeded) and imaging using the PIV system, two non-sequential snapshots of which are portrayed in Fig. 4.1. Figure 4.1a shows the formation of primary vortices (indicated by I) in the free jet mixing layer due to the growth of the Kelvin-Helmholtz (K-H) instability. These vortices enhance momentum transfer through the entrainment of nearly stagnant fluid in the surroundings. The primary vortices are convected downstream by the mean flow and approach the impinging surface. Near the surface, the primary vortices deform slightly as the structures are reoriented before convecting downstream along the impingement surface. The passage of the primary vortices in the wall jet region induces the formation of a secondary vortex (indicated by II). The formation is attributed to the strong adverse pressure gradients induced by the passage of primary vortices in the outer shear layer [19, 75], which causes the deceleration and roll-up of a thin layer of fluid near the wall. The formation of secondary vortices has been observed for various other flow conditions, including both round and slot nozzle geometries [24, 25, 75]. Two vortex merging events, labelled III and IV, are observed in Fig. 4.1b. The arrow labelled III shows the onset of merging in the flow reorientation region above the stagnation region, while IV shows two vortices merging near $x/B = 3$. In both cases, the vortex merging process is not complete, as two distinct dark elliptical shapes surrounded by the seeding (marking the vortex cores) are observed.

The spatio-temporal development of the coherent structures is visualized by a series of vorticity contour snapshots in Figs. 4.2 and 4.3, in order to examine the development of the coherent structures in more detail. Each frame is separated by a non-dimensional time defined by $t^* = tU_c/B$ and at least one full shedding cycle is shown. Vorticity is calculated using the circulation method by employing an 8-point line integral at each point of the velocity vector grid; vorticity along the boundary is estimated using a central differencing scheme [96]. Although vorticity facilitates the visualization of coherent structures, it is not able to distinguish between pure shearing and swirling motion [17]. A more robust definition of a vortex proposed by Jeong & Hussain [97], known as the λ_2-criterion, uses the three eigenvalues of the tensor $S^2 + \Omega^2$. Here S and Ω are the symmetric and anti-symmetric tensors obtained from the velocity gradient tensor. At each point in the flow, three ranked eigenvalues λ_i, are identified such that $\lambda_1 \geq \lambda_2 \geq \lambda_3$. A point in the flow is part of a vortex if at least two of the eigenvalues at that point are negative, i.e. $\lambda_2 < 0$. The λ_2-criterion accurately identifies the vortex core and the associated pressure minimum for a wide range of Reynolds numbers in unsteady flows. Therefore, the λ_2-criterion method is applied to assist in coherent structure identification for the vorticity sequences in Figs. 4.2 and 4.3, where the solid black lines mark iso-contours when $\lambda_2 < 0$. In addition, dashed lines are used to facilitate the tracking of individual coherent structures.

The behaviour of the coherent structures at $H/B = 2$ and $\mathrm{Re}_B = 3000$ is depicted in Fig. 4.2a. Vortex A_1 shows the shedding of a primary vortex, which begins in the mixing layer of the free jet region around $x/B = 0.6$ and $y/B = 0.95$. Prior to shedding, the primary vortex A_1 is elongated in the streamwise direction. As the primary vortex A_1 approaches the stagnation region, the shear layer is deflected by the impinging surface. Vortex shedding is observed near $x/B = 0.4$ and $y/B = 0.7$. The shedding process spans approximately four frames, which equals to an estimated shedding period of $t_0^* = 2.81$ and a shedding frequency of $St_{B,0} = 0.36$. During the primary vortex shedding process the convective velocity remains relatively constant as indicated by the constant slope of the dashed line that follows the location of vortex A_1. Once the shedding process is complete, the primary vortex travels downstream from the flow reorientation region into the wall jet region, where secondary vortex formation and primary vortex merging is observed.

As a primary vortex C_1 passes in the outer shear layer of the wall jet region, it induces the roll up of the wall attached vorticity, forming vortex D_1 near $x/B = 3.2$. The shedding of D_1 is indicated in the successive frames in Fig. 4.2a. The secondary vortex D_1 pairs up with the primary vortex C_1 in the outer shear layer and the vortex pair follows a trajectory away from the wall. Vortex E_1 is a previously shed secondary vortex, which is paired with a primary vortex. Both vortices D_1 and E_1 show a constant convective velocity as indicated by the dashed lines. A merging event is observed between two primary vortices B_1 and C_1.

The collective interaction between vortices B_1, C_1, and D_1 causes the leading vortex to

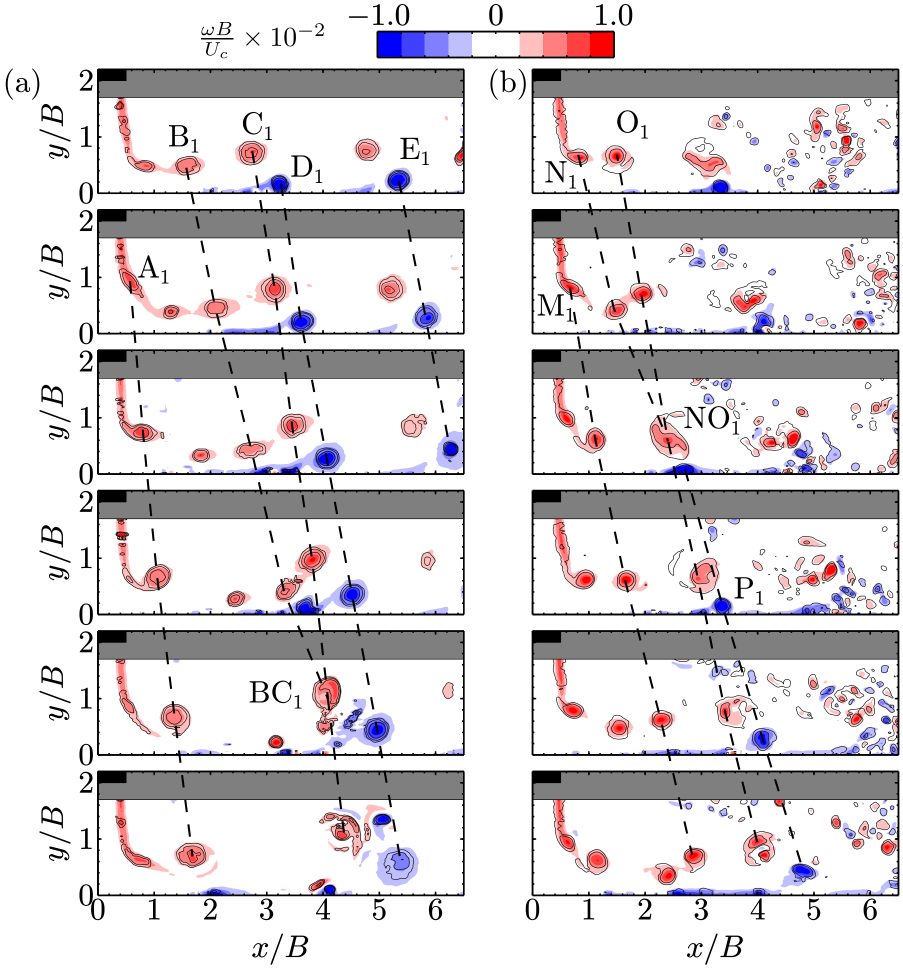

Figure 4.2: Representative example of instantaneous contours of vorticity and λ_2 for $H/B = 2$ at (a) $\mathrm{Re}_B = 3000$ and (b) $\mathrm{Re}_B = 6000$, where each consecutive image is separated by $t^* = 0.94$ and 1.32, respectively.

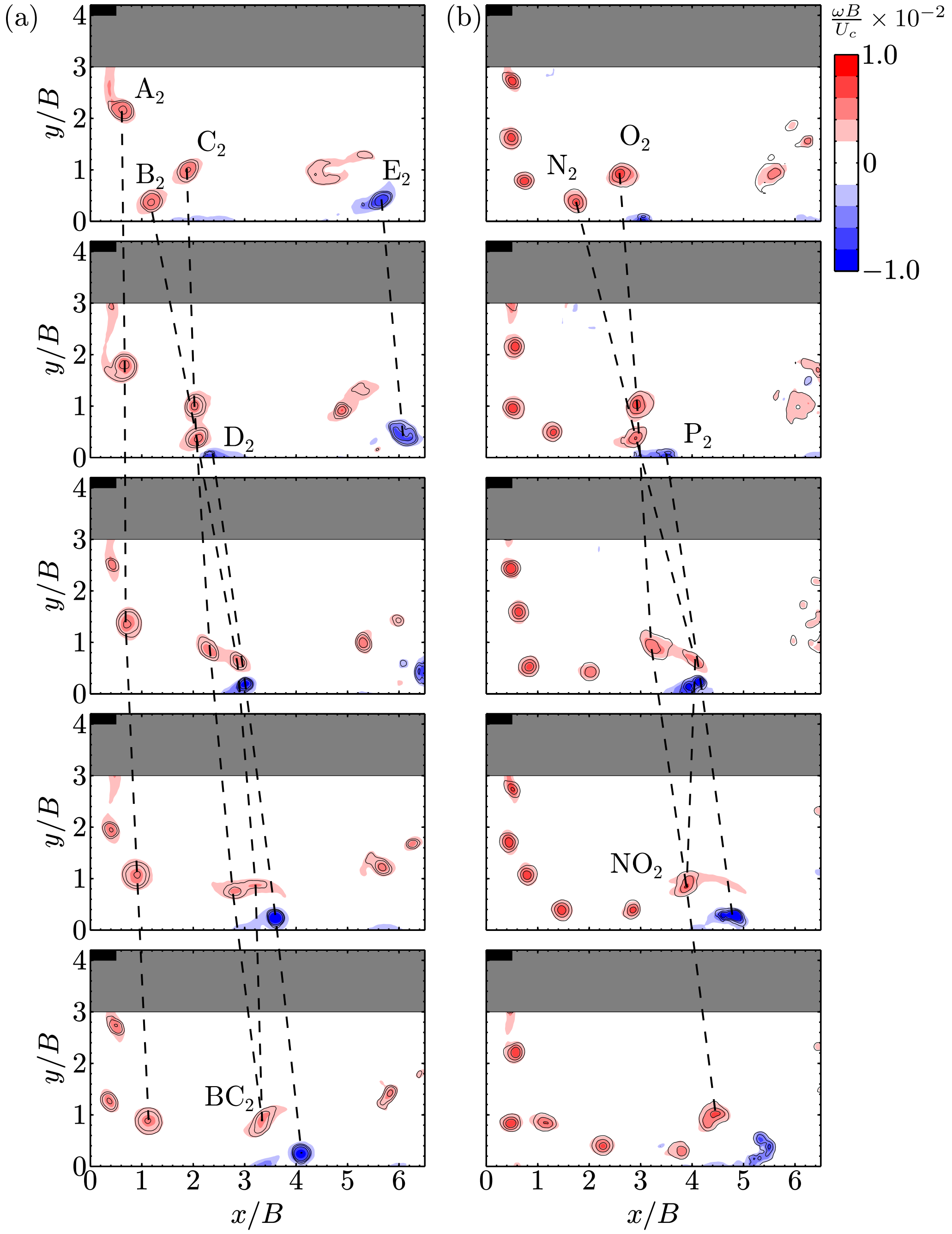

Figure 4.3: Representative example of instantaneous contours of vorticity and λ_2 for $H/B = 4$ at (a) $\mathrm{Re}_B = 6000$ and (b) $\mathrm{Re}_B = 6000$, where each consecutive image is separated by $t^* = 1.03$ and 1.31, respectively.

decelerate and vortex merging initiates as a critical distance is reached between vortices B_1 and C_1 [82, 83]. The mean flow also aids in decreasing the distance between the two vortex cores B_1 and C_1. As these primary vortices merge, opposing signed wall vorticity is shed from the surface which interacts with vortex D_1. The interaction of these smaller scale structures with the larger primary and secondary vortices leads to the complex behaviour that is observed in the last frame of Fig. 4.2a.

Figure 4.2b shows the development of the coherent structures for $H/B = 2$ when the Reynolds number is increased to 6000. As the Reynolds number is increased, the shedding location is expected to shift upstream towards the nozzle due to the faster growth of the K-H instability. In the time-resolved sequences, the shift in the vortex shedding location is difficult to detect qualitatively; however, the mean properties in Section 4.2 show a shift in the shedding location. The convective velocities of primary vortices appear to be similar in the two Reynolds number cases, as primary vortex M_1 travels a larger distance in a proportionately larger time. The length scale of the primary vortices also remains similar when the Reynolds number is increased. However, the shedding frequency shows an increase with increasing Reynolds number: vortex M_1 completes its shedding within two frames resulting in $t_0^* = 1.32$ and $St_{B,0} = 0.76$.

A vortex merging event between vortices N_1 and O_1 is observed in Fig. 4.2b, while secondary vortices are shed in the wall jet region. The merged vortex NO_1 and secondary vortex P_1 pair up and follow a common trajectory away from the wall, at a nearly constant speed, similar to the lower Reynolds number case. As the Reynolds number is increased, the vortex breakdown process is expedited as observed by the plethora of smaller scale structures when $x/B > 5$. The emergence of these small scale structures indicates the transition into a more turbulent and three dimensional flow.

Similar flow features are observed when the nozzle-to-plate distance is increased to $H/B = 4$. Figure 4.3a shows the evolution of the coherent structures when $H/B = 4$ and $\mathrm{Re}_B = 3000$. The shedding of the primary vortices shifts upstream to the mixing layer of the free jet region as the increased nozzle-to-plate distance allows the shear layer to develop normal to the surface for a larger distance. The shedding of primary vortices is observed in the free jet mixing layer at $x/B = 0.7$ and $1.5 < y/B < 2.5$. The only changes to the primary vortex shedding is the shift in the shedding location. The time and length scales remain nearly constant; the shedding frequency is estimated to be $St_{B,0} = 0.49$ for the instance shown in Fig. 4.3a. A vortex merging event is also observed as shown by vortices B_2 and C_2 and the convective velocities are comparable to when $H/B = 2$ and $\mathrm{Re}_B = 3000$. In the instance shown in Fig. 4.3a, vortex merging occurs further upstream but the mechanism appears to be the same: the collective interaction between the two primary vortices and the secondary vortex causes the distance between the two primary vortices to reach a critical value, at which point vortex merging initiates. Once more, the primary and secondary vortices pair up and move away from the wall as they convect downstream. As the nozzle-to-plate distance is increased, the onset of vortex breakdown is observed near the edge of the FOV for $\mathrm{Re}_B = 3000$. Beginning near $x/B \approx 4.5$, the structures deform and stretch in the surface parallel direction, while the length scales decrease.

Lastly, Fig. 4.3b shows the development of the coherent structures when $H/B = 4$ and $\mathrm{Re}_B = 6000$. Most notably, the primary shedding location shifts upstream with increasing Reynolds number as expected due to the accelerated growth of the Kelvin-Helmholtz instability. The shear layer roll up process is beyond the FOV, with only the later stages of primary vortex shedding captured at $y/B = 3$ in the free jet mixing layer. Vortices N_2 and O_2 show a vortex merging event, which follows the behaviour for vortex merging at the other flow conditions. The secondary vortex formation is also observed near $x/B = 4$, however the structures appear to be highly deformed and break down earlier when compared to the the lower Reynolds number case. At the higher Reynolds number, the wall jet is much more energetic and the secondary vortex formation process is less prominent. Vortex breakdown is also observed at the edge of the FOV ($x/B = 6.5$), determined by the small length scales of the structures observed.

4.2 Time-Averaged Flow Field Characteristics

In this section, time averaged quantities of non-dimensional velocity magnitude ($\|\vec{U}\|/U_c$), Reynolds normal stresses ($\overline{u'u'}/U_c^2$ and $\overline{v'v'}/U_c^2$), Reynolds shear stress ($\overline{u'v'}/U_c^2$), turbulence production (PB/U_c^3), and vorticity ($\omega B/U_c$) are presented. All results presented in this section are calculated using the velocity measurements collected using planar PIV at a sample rate of 0.125 Hz, allowing for uncorrelated snapshots to be collected and thus improving the convergence of the statistics.

Figure 4.4 shows the non-dimensional time-averaged velocity magnitude, where the typical flow topology of an impinging jet is observed. In all cases, the stagnation region is characterized by the near zero velocity magnitude region that forms at the wall, centred around the intersection of the jet centreline and the surface. The size of the stagnation region is not significantly different between the four cases, however the effect of the stagnation region on the free jet region is more prominent when $H/B = 2$. The fully developed free jet and decay region are not observed, as expected by potential core impingement at low nozzle-to-plate spacings [60]. The mixing layer of the free jet region shows a higher velocity than the jet centreline, forming a dip in the streamwise velocity profile at the jet centreline at $y/B \approx 1.5$. As the higher velocity flow in the mixing layer approaches

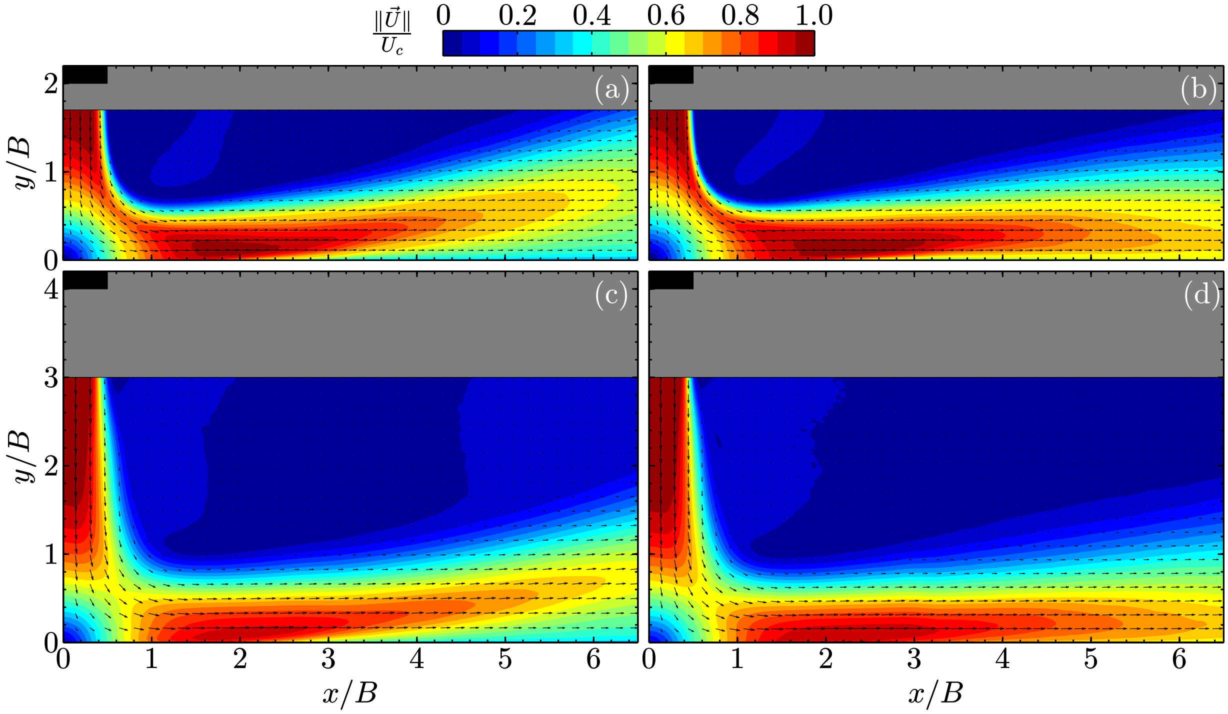

Figure 4.4: Time averaged velocity magnitude. (a) $H/B = 2$, $\mathrm{Re}_B = 3000$, (b) $H/B = 2$, $\mathrm{Re}_B = 6000$, (c) $H/B = 4$, $\mathrm{Re}_B = 3000$, and (d) $H/B = 4$, $\mathrm{Re}_B = 6000$.

the impinging surface, it is deflected above the stagnation region and reoriented in the surface parallel direction forming the wall jet region. Comparatively, when $H/B = 4$, the effect of impingement on the free jet region is lessened and the potential core is maintained further downstream of the nozzle exit. Similar to when $H/B = 2$, the decay region is not observed and the dip in the the centreline velocity of the streamwise velocity profile is less exaggerated.

The suppression of the potential core region due to the lower nozzle-to-plate distance is observed in Fig. 4.5a by the surface normal velocity along the jet centreline. Using the location where the dynamic pressure reaches 95% of its initial value as the measure, the end of the potential core for $H/B = 2$ is $y/B = 1.35$ and 1.45 for $\mathrm{Re}_B = 3000$ and 6000, respectively. For $H/B = 4$, the potential core is observed for a larger portion of the nozzle-to-plate distance, ending at $y/B = 1.7$ for both Reynolds numbers. Following the end of the potential core, the streamwise jet centerline velocity exhibits a similar linear decrease spatially after normalization by U_c for all cases. The linear decay of the centerline velocity has been observed previously by others for both round and plane jets at various flow conditions [17, 24, 37, 59].

The wall jet region originates between $1 < x/B < 2$ and is marked by the reorientation and re-acceleration of the flow parallel to the impingement surface due to the momentum

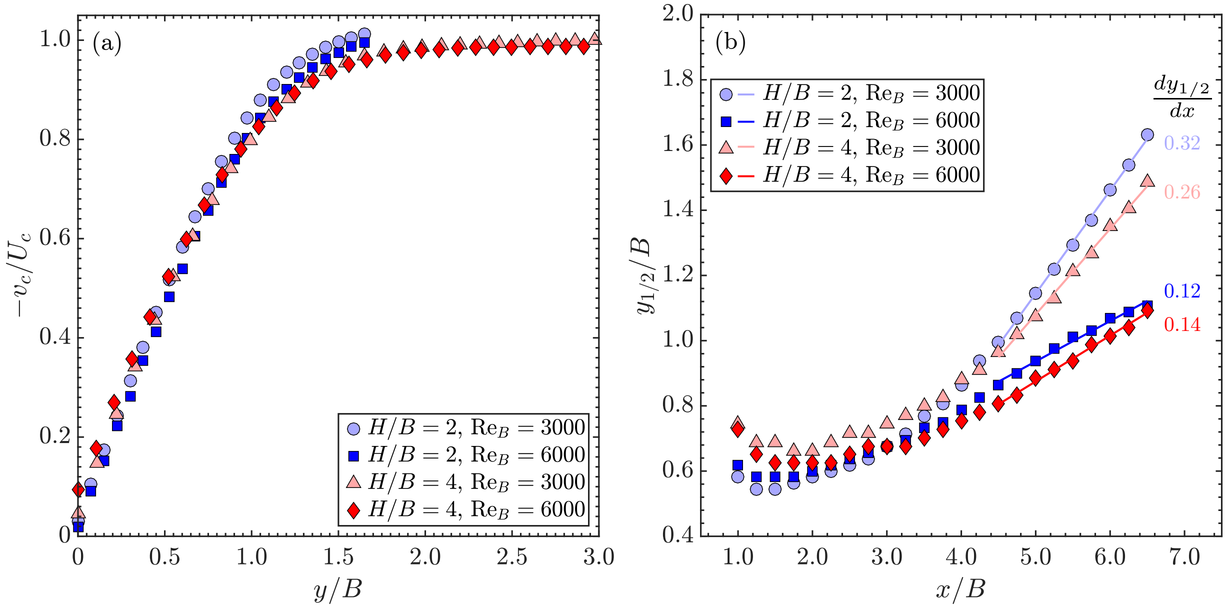

Figure 4.5: Free jet and wall jet structure. (a) Streamwise velocity along the free jet centreline; and (b) wall jet half width ($y_{1/2}$), where the lines indicate a least square linear curve fit for $y/B > 4.5$ where the wall jet region is self-similar.

supplied by the upstream flow. The wall jet region is characterized by the presence of a maximum velocity above the impinging surface, which divides the flow into the inner and outer layer, as seen in Fig. 2.3. Fitzgerald & Garimella [66] reported that for a round jet, the characteristics of the wall jet region beyond $r/D > 3$ are independent of the Reynolds number in the range of 8500 to 23 000. In contrast, the present study shows that changing the Reynolds number from 3000 to 6000 has a notable effect on the velocity magnitude contours of the wall jet region for both impingement heights.

At the lower Reynolds number, the deceleration of the flow in the inner layer of the wall jet initiates at $x/B = 3$ for both nozzle-to-plate distances and the wall jet is deflected away from the impingement surface. The region of low velocity magnitude corresponds to the location of secondary vortex formation, as observed in the instantaneous snapshots in Figs. 4.2 and 4.3. In the impinging jet flow, a transient adverse pressure gradient is induced in the wall jet region due to the passage of the primary vortices, leading to the formation of the secondary vortices from the slower moving flow near the wall [71, 75]. This slower moving flow is expected to deflect the higher velocity flow approaching from the stagnation region away from the wall, forming a low magnitude velocity region where secondary vortices are shed. As the secondary vortices become less coherent and more deformed with increasing Reynolds number and nozzle-to-plate spacing, the deflection of the wall jet also decreases.

According to Baydar [98], for a confined impinging jet at $\mathrm{Re}_D = 2700$ and 5000 and

$H/D = 2$, a sub-atmospheric mean pressure region exists between $3 < r/D < 5$, but is not detected at $H/D = 4$. For an axisymmetric impinging jet at $\mathrm{Re}_D = 19\,000$ and $H/D = 2$, Didden & Ho [75] found a favourable pressure gradient that asymptotically approached zero, but data was obtained only up to $r/D = 1.6$. From these studies, if an adverse pressure gradient is present, it is expected to become weaker with increasing Reynolds number and impingement height. However for $H/B = 4$ and $\mathrm{Re}_B = 3000$, at $x/B = 3$, where the mean pressure gradient is expected to be nearly zero according to Baydar [98], a low velocity magnitude region and flow separation is observed, which indicates that a mean adverse pressure gradient is present beyond $x/B = 3$. The discussion of mean flow separation in terms of the mean adverse pressure gradient requires further investigation of the flow with wall pressure measurements.

The deflection of the wall jet observed in Fig. 4.4 is quantified by the wall jet growth rate. It is characterized by a constant value of $dy_{1/2}/dx$ [53, 54], and is shown in Fig. 4.5b for each of the flow conditions. When estimating the growth rate, a least squares linear fit is applied to $y_{1/2}$ in the region where the wall jet is found to be self-similar ($y/B > 4.5$) and is represented by the four lines in Fig. 4.5b. As expected, the two largest growth rates are observed when $\mathrm{Re}_B = 3000$ with $dy_{1/2}/dx = 0.32$ and 0.26 for $H/B = 2$ and 4, respectively. At $\mathrm{Re}_B = 6000$, the growth rates decrease to $dy_{1/2}/dx = 0.12$ and 0.14 for $H/B = 2$ and 4, respectively. To the knowledge of the author, the growth rate of the wall jet region created by a planar impinging jet has not been reported. The growth rate of a wall jet created by an axisymmetric impinging jet at Reynolds numbers ranging from 18 800 to 90 000 has been reported [26, 73, 74], which agrees with the constant value of 0.073 put forth by Launder & Rodi [54] for a wall jet created by a jet oriented parallel to the surface. The growth of the wall jets observed in the present study is $2 - 4$ times larger than the widely accepted growth rates reported by Launder & Rodi [54] for a planar wall jet. The discrepancies in the wall jet growth rate is attributed the to significantly larger Reynolds numbers of the impinging jets found in the literature. At the higher Reynolds numbers, the secondary vortex formation is expected to be suppressed and the flow will remain more parallel to the surface.

The surface parallel component of Reynolds normal stress ($\overline{u'u'}$) contour plot in Fig. 4.6 shows the amplification of surface parallel velocity fluctuations downstream of the nozzle exit. For $H/B = 2$, the fluctuations are mainly concentrated in the wall jet region and are nearly zero in the mixing layer downstream of the nozzle for both Reynolds numbers. In the flow reorientation region, the growth of velocity fluctuations associated with the shedding of primary vortices is observed. At $H/B = 2$ and $\mathrm{Re}_B = 3000$ (Fig. 4.6a), a bimodal distribution of $\overline{u'u'}$ in the wall jet region ($x/B > 3$, $y/B < y_{1/2}$) is observed. The intense amplification of the near wall velocity fluctuations coincides with the formation of

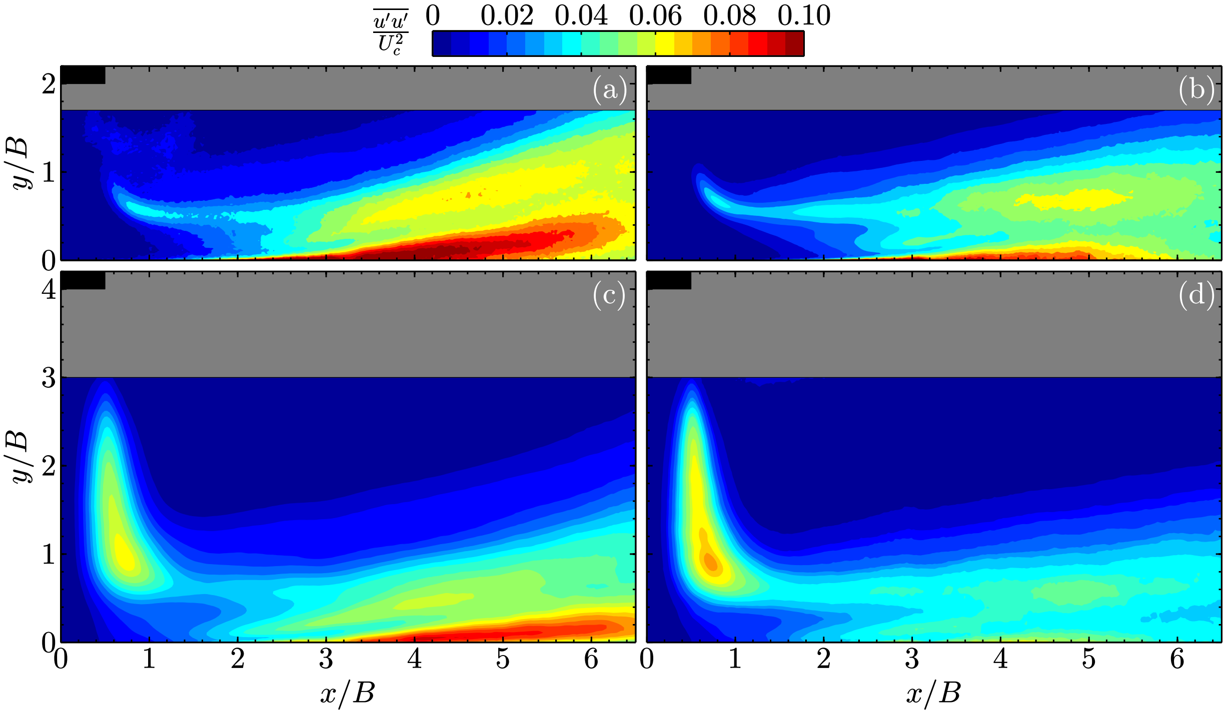

Figure 4.6: Surface parallel component of Reynolds normal stress. (a) $H/B = 2$, $\mathrm{Re}_B = 3000$, (b) $H/B = 2$, $\mathrm{Re}_B = 6000$, (c) $H/B = 4$, $\mathrm{Re}_B = 3000$, and (d) $H/B = 4$, $\mathrm{Re}_B = 6000$.

the secondary vortex, which causes the low velocity magnitude region observed in Fig. 4.4. Similarly, the second peak in the fluctuations near the outer shear layer is associated with the passage of primary vortices. The near wall surface parallel velocity fluctuations are approximately 40% larger than the fluctuation levels in the outer shear layer.

As the Reynolds number is increased to 6000 (Fig. 4.6b), for $H/B = 2$, the velocity fluctuations levels in the wall jet region decrease due to the earlier breakdown of the paired up primary and secondary vortices. The fluctuations near $x/B = 6$ decrease significantly when the Reynolds number is increased, as this region is dominated by small vortical structures following the onset of vortex breakdown. The shift of the vortex shedding upstream with increasing Reynolds number is also observed as the local maximum of the velocity fluctuations in the flow reorientation region moves slightly upstream as the Reynolds number is increased. In comparison, as the nozzle-to-plate distance is increased for each Reynolds number, the onset of the velocity fluctuation amplification shifts upstream in to the free jet mixing layer and flow reorientation region, which is consistent with a shift in the shedding location of the coherent structures upstream. Similar to $H/B = 2$, at $H/B = 4$, a bimodal distribution in the surface parallel velocity fluctuations is observed in the wall jet region due to the presence of both primary and secondary vortices. Furthermore, as the Reynolds number is increased from 3000 to 6000 for $H/B = 4$, a decrease in the fluctuations

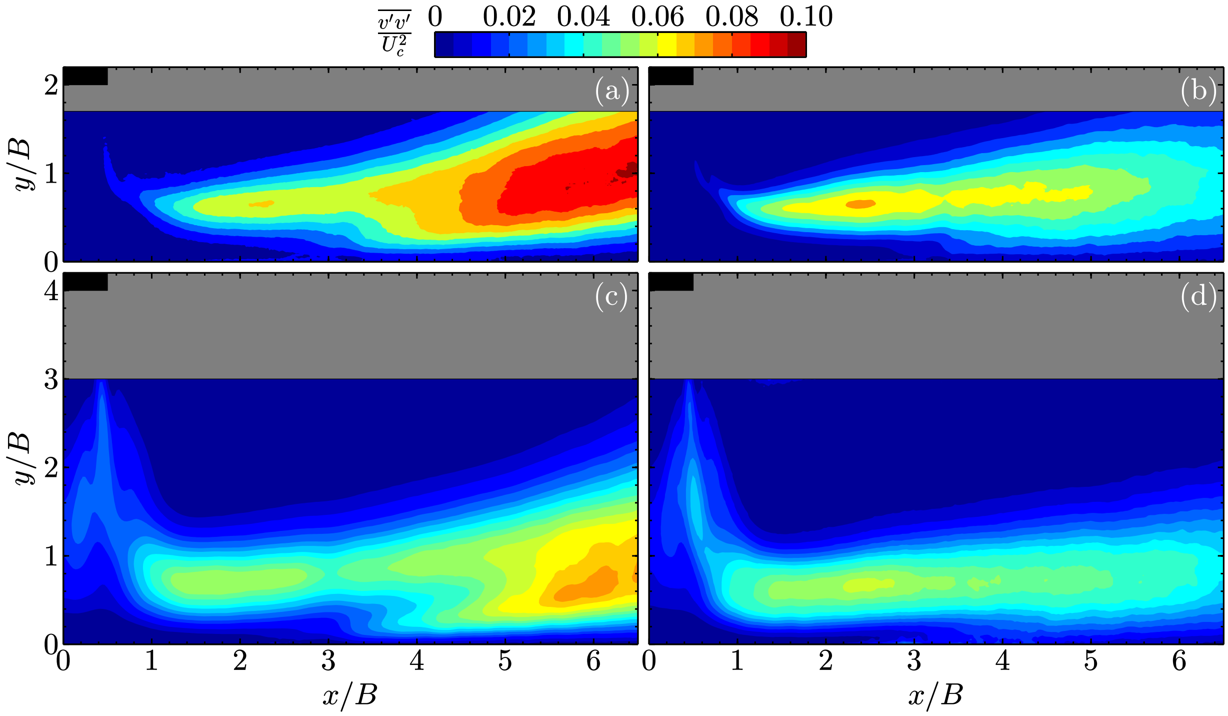

Figure 4.7: Surface normal component of Reynolds normal stress. (a) $H/B = 2$, $\mathrm{Re}_B = 3000$, (b) $H/B = 2$, $\mathrm{Re}_B = 6000$, (c) $H/B = 4$, $\mathrm{Re}_B = 3000$, and (d) $H/B = 4$, $\mathrm{Re}_B = 6000$.

is observed due to the relatively lower energy of the structures when compared to the mean flow.

Figure 4.7 shows the surface normal component of the Reynolds normal stress. In all flow configurations, the surface normal fluctuations show a low magnitude in the near wall region due to the damping effect of the wall [14, 37, 54, 99]. As the flow develops downstream of the nozzle, the mixing layer is characterized by near zero values of surface normal velocity fluctuations for $H/B = 2$ and increases when $H/B = 4$, as expected, due to vortex shedding in the mixing layer at the higher nozzle-to-plate spacing. The change of flow conditions has a dramatic effect on the surface normal fluctuations in the wall jet region. At $H/B = 2$ and $\mathrm{Re}_B = 3000$, a peak in the fluctuations is observed at $x/B = 2.2$ in the outer shear layer, which coincides with primary vortex shedding and merging. An intense amplification of the velocity fluctuations is observed when $x/B > 5$. As discussed previously, primary vortices (single or merged) pair up with secondary vortices that are shed from the wall and follow a common trajectory away from the wall. This process is complicated by the fact that some vortex breakdown is also observed as these vortices convect downstream. The pairing up and breakdown of primary and secondary vortices have been observed prior to the sudden transition to turbulence in plane wall jet flows [71, 100], but the relatively large lengths scales of the structures observed when $H/B = 2$ and

$\mathrm{Re}_B = 3000$ would suggest that the flow in the wall jet region has not fully transitioned to turbulence. The complex behaviour of these structures contribute to the amplification of the surface normal velocity fluctuations observed in this region.

When the Reynolds number is increased to 6000 while $H/B = 2$, the fluctuations decrease in the later stages of the wall jet region due to the more turbulent nature of the flow. At the higher Reynolds number, the vortex breakdown process is more violent and the region has an abundance of small scale structures, which contribute less to the surface normal velocity fluctuations in the plane of measurements. A similar amplification of the wall normal fluctuations is also observed at $H/B = 4$ and $\mathrm{Re}_B = 3000$, however, the magnitude of the fluctuations are lower when compared to $H/B = 2$ and $\mathrm{Re}_B = 3000$. This indicates that the structures become less energetic as the nozzle-to-plate distance is increased when compared to the mean flow, due to the increased momentum diffusion during the lengthened trajectory. As the Reynolds number is increased to 6000 at $H/B = 4$, an overall decrease in the fluctuations is observed in the wall jet region. A maximum in the fluctuations is observed near $x/B = 2.5$, likely due to primary vortex merging, before monotonically decreasing in the wall jet region where vortex breakdown is observed. The overall decrease of the velocity fluctuations in the wall jet region indicates that the flow has transitioned to a more turbulent regime with increasing Reynolds number at $H/B = 4$.

The normalized Reynolds shear stress ($\overline{u'v'}/U_c^2$) shown in Fig. 4.8 exhibits a similar distribution to the Reynolds normal stresses in Figs. 4.6 and 4.7. Near zero values are observed close the wall for all flow conditions, due to the dampening of the surface normal velocity fluctuations by the impinging surface. Furthermore, zero values of Reynolds shear stress are observed in the stagnation region and in the potential core of the free jet. For $H/B = 2$, low magnitude negative values of Reynolds shear stress are observed around $x/B \approx 0.7$ and $y/B \approx 1$, where the flow is reoriented above the stagnation region. For $H/B = 4$, low negative values of Reynolds shear stress are also found in the free jet mixing layer, while comparable positive values characterize the flow reorientation region. In the wall jet region, when $x/B > 3$, the Reynolds shear stress values amplify (positively) as the flow develops and maxima are observed near y_m. $H/B = 2$ and $\mathrm{Re}_B = 3000$ exhibits the largest positive value (0.05) of Reynolds shear stress in the wall jet region and increasing the nozzle-to-plate ratio and the Reynolds number, decreases the magnitude of the Reynolds shear stress (positive) in the wall jet region.

The turbulence production shown in Fig. 4.9 is computed based on measured planar velocity as:

$$P = -\left(\overline{u'u'}\frac{\partial \overline{U}}{\partial x} + \overline{u'v'}\frac{\partial \overline{U}}{\partial y} + \overline{u'v'}\frac{\partial \overline{V}}{\partial x} + \overline{v'v'}\frac{\partial \overline{V}}{\partial y}\right) \tag{4.1}$$

A positive value of P indicates energy transfer according to the direct energy cascade from

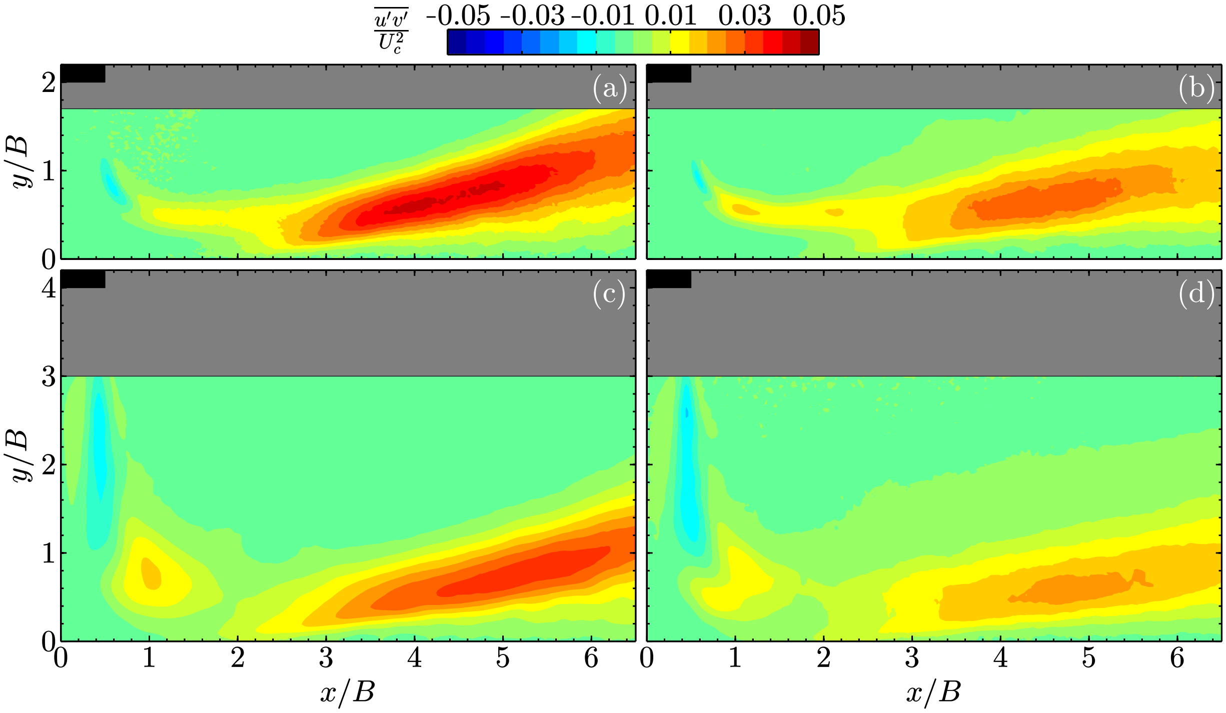

Figure 4.8: Reynolds shear stress. (a) $H/B = 2$, $\mathrm{Re}_B = 3000$, (b) $H/B = 2$, $\mathrm{Re}_B = 6000$, (c) $H/B = 4$, $\mathrm{Re}_B = 3000$, and (d) $H/B = 4$, $\mathrm{Re}_B = 6000$.

the mean flow to the velocity fluctuations. In the mixing layer of the free jet region, an increase in the turbulence production is observed, which coincides with the formation of primary vortices. A local maximum value in the turbulence production is also observed in the wall jet region, in the outer shear layer in all cases when $x/B > 3$. The two local turbulence production maxima are located in regions of high Reynolds stresses and mean velocity gradients, as expected. In these regions energy is transfered from mean flow into the fluctuations, as growth in the fluctuations is observed downstream of the nozzle exit and in the outer shear layers of the wall jet region. The coherent structures that advect through these regions are energized by the mean flow. An opposite behaviour is observed near the surface when $x/B > 3$, for all cases, where negative values of turbulence production near the surface coincide with the regions of low velocity magnitude and large surface parallel fluctuations. The negative values near the surface have been observed in previous studies of impinging jets [24, 27, 99].

For $H/B = 2$, as the Reynolds number is increased from 3000 to 6000, turbulence production shifts upstream due to the vortex shedding location also shifting upstream. For $x/B > 5$, the turbulence production in the outer shear layer decreases with increasing Reynolds number due to vortex breakdown. Furthermore, as the Reynolds number is increased, the near wall turbulence production magnitude decreases in the region $x/B > 3$

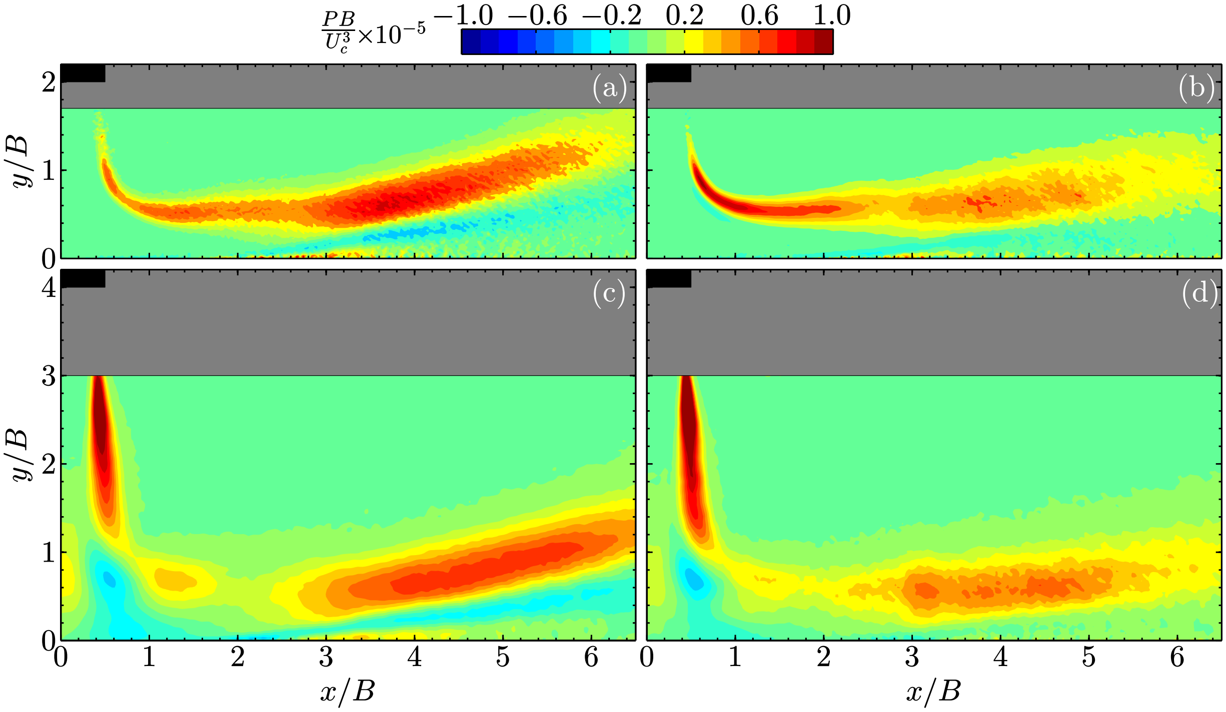

Figure 4.9: Turbulence generation term where positive indicates transfer of energy from mean flow to velocity fluctuations. (a) $H/B = 2$, $\mathrm{Re}_B = 3000$, (b) $H/B = 2$, $\mathrm{Re}_B = 6000$, (c) $H/B = 4$, $\mathrm{Re}_B = 3000$, and (d) $H/B = 4$, $\mathrm{Re}_B = 6000$.

and is attributed to a weaker secondary vortex shedding process. A similar behaviour is observed for $H/B = 4$ as the Reynolds number is increased. As H/B is increased from 2 to 4, a region of negative turbulence production is observed in the flow stagnation region. At the higher H/B, the primary vortices are shed above the stagnation region and, as the structures convect through it, the low energy fluid in the region is energized by the coherent structures.

The time-averaged vorticity fields in Fig. 4.10 show the development of the outer shear layer (red) and the inner shear layer of the wall jet region (blue). The shear layer trajectories are indicated by a dashed line for the outer shear layer and a dash-dot line for the inner shear layer. The outer shear layer trajectories are determined by using a piecewise smoothing spline fit to the locations of maximum vorticity. The inner shear layer is treated differently due to the wall; the minimum vorticity is always observed near the wall and is not indicative of the growth of the inner shear layer. Therefore, a more geometric definition is used for the inner shear layer trajectories: the height of the shear layer, extracted using the maximum non-zero vorticity contour, is divided by two in order to estimate the centre of the inner shear layer at each x/B location. Again, a smoothing spline fit is used to estimate the trajectory of the inner shear layer. In all cases, as the flow approaches the impinging surface,

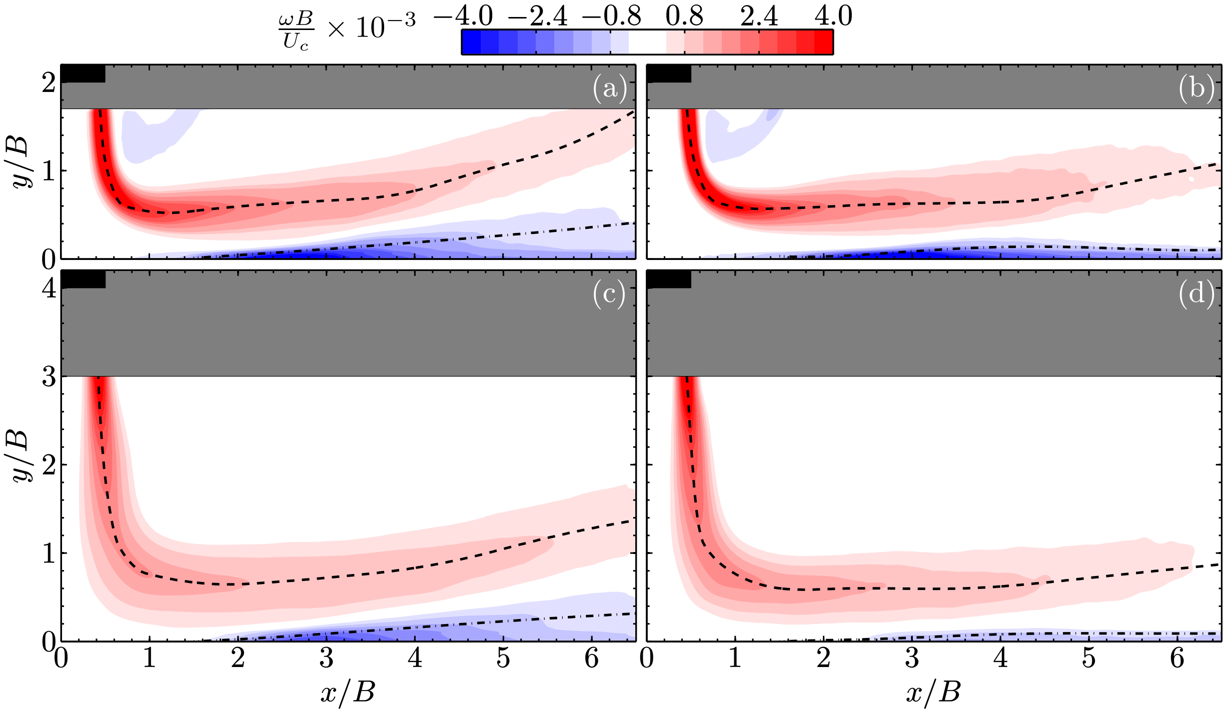

Figure 4.10: Time-averaged vorticity (a) $H/B = 2$, $\mathrm{Re}_B = 3000$, (b) $H/B = 2$, $\mathrm{Re}_B = 6000$, (c) $H/B = 4$, $\mathrm{Re}_B = 3000$, and (d) $H/B = 4$, $\mathrm{Re}_B = 6000$. Shear layer trajectories are indicated by dashed lines: free shear layer (−−) and inner shear layer of the wall jet region (−·).

the outer shear layer is reoriented parallel to the wall. Next, the outer shear layer is deflected away from the surface in the wall jet region and the amount of deflection is correlated with the maximum height of the inner shear layer trajectory. This behaviour is observed in the instantaneous snapshots when the primary and secondary vortices pair and veer away from the wall. For both nozzle-to-plate spacings, as the Reynolds number is increased, the inner shear layer height decreases and consequently the outer shear layer deflection lessens. This is most apparent when $H/B = 4$ and $\mathrm{Re}_B = 6000$, where the inner shear layer height is less than $0.15B$ and the vorticity levels are minimal. The increase in the Reynolds number causes the secondary vortices to become more deformed and stretched, leading to an earlier breakdown of the vortex pair. With the increase of small scale structures, the flow remains more attached to the surface. The increase of the nozzle-to-plate spacing has less of an effect on the development of the shear layers in the wall jet region. However, the shear layers show increased diffusion with increasing H/B in the free jet region and the outer shear layer extends into the stagnation region at $H/B = 4$. This is attributed to the shift in the vortex formation location upstream in to the free jet region with increasing H/B, which aids in the transfer of momentum from the centre of the jet to the ambient flow, widening the shear layers.

4.3 Dynamics of Coherent Structures

The instantaneous snapshots presented in Section 4.1 demonstrate the unsteady nature of the flow due to the shedding of vortical structures. In order to characterize the behaviour of the primary and secondary vortices, time-resolved velocity measurements are used for the analysis presented in this section.

The streamwise evolution of the coherent structures is analyzed by computing the power spectra of velocity fluctuations at various points in the outer shear layer and inner shear layer trajectories identified in Fig. 4.10. Different components of the velocity fluctuations are used for the outer and inner shear layers in order to compute the power spectra using the streamwise normal velocity fluctuations. In the free jet region, surface parallel fluctuation signals are used to compute the power spectral density, while surface normal fluctuations are used in the wall jet region ($x/B > 1$). All power spectra are computed using Welch's averaged, modified periodogram approach [101]. The velocity signal at each location is divided into six windows of 2^{10} samples with 75% overlap, which results in a frequency resolution of $\Delta f = 3.1$ Hz for all flow conditions. In terms of the non-dimensional frequency resolution, this corresponds to $\Delta \mathrm{St}_B = 0.006$ and 0.003 for $\mathrm{Re}_B = 3000$ and 6000, respectively.

The result of power spectral analysis for $H/B = 2$ and $\mathrm{Re}_B = 3000$ is shown in Fig. 4.11. The power spectra profiles pertain to several locations along the outer and inner shear layers, indicated in the figure inset as points P_i and S_i, respectively. In unforced jet flow, three dominant peaks are expected with the highest associated with vortex shedding and the lower peaks associated with the frequencies at which coherent structures pass following merging [16, 32, 102]. However, at $H/B = 2$ and $\mathrm{Re}_B = 3000$, the power spectra in the outer shear layer (Fig. 4.11a) shows the amplification of a band of frequencies between $0.4 < \mathrm{St}_B < 0.50$, for the signals at P_3 and P_4, which is located in the region associated with vortex shedding. The discrepancy between the broader peak observed in Fig. 4.11a compared to the dominant peaks observed in previous studies is believed to be associated with Reynolds number differences. Han & Goldstein [103] showed that for a axisymmetric free jet, as the Reynolds number is increased from $\mathrm{Re}_D = 8000$ to 120 000, the peaks in the spectra associated with vortex shedding became more prominent.

As the flow develops downstream into the wall jet region, the band of amplified disturbances shifts to lower frequencies due to vortex merging [19, 30]. For example, at P_6, most pronounced disturbances are found within a range of frequencies between $0.15 < \mathrm{St}_B < 0.25$. The shift to the lower frequencies is associated with the primary vortex merging process that is observed in the wall jet region (Fig. 4.2a). The power spectra profile of P_8 shows a relatively broadband peak located in a frequency range between $0.06 < \mathrm{St}_B < 0.225$ and is

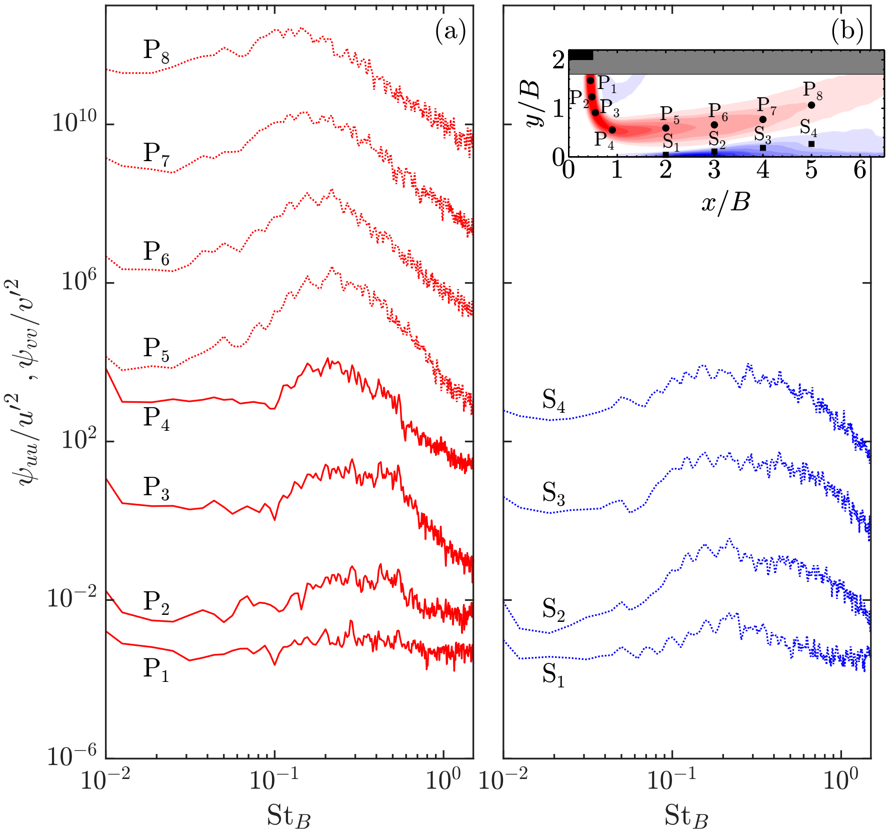

Figure 4.11: Frequency spectra of the streamwise normal fluctuating velocity for $H/B = 2$ and Re$_B$ = 3000 at several locations in the (a) outer shear layer and (b) inner shear layer shown in the inset image. Each spectrum is stepped by two orders of magnitude. Solid lines and dotted lines indicated spectra computed from surface parallel and normal fluctuation signals, respectively.

associated the complex interaction between the primary and secondary vortices that remain as orderly structures, which are identifiable in instant snapshots in Fig. 4.2a.

The spectra at four locations in the inner shear layer is shown in Fig. 4.11b in order to characterize the secondary vortex shedding process. The power spectra of the streamwise velocity fluctuations at S_2 shows high energy content in a band of frequencies between $0.1 < \mathrm{St}_B < 0.25$, which is equivalent to the higher energy band of frequencies corresponding to merged primary vortices in the spectra at P_6. The distribution of the energy content across similar frequency bands in the power spectra shown in Fig. 4.11 reflects that the secondary vortices are shed in the same frequency band as the merged vortices, which is supported by the pairing with primary vortices observed in the instantaneous snapshots.

As the Reynolds number is increased to 6000, while the nozzle-to-plate distance is kept constant at $H/B = 2$, the vortex shedding process is altered, as shown by the power spectra is Fig. 4.12. Figure 4.12a shows the growth of the fluctuations in a narrower band of frequencies with a more discernible peak in the spectra from P_1 to P_4, when compared to the lower Reynolds number. A dominant spectral peak is observed at P_3 and P_4, where vortex shedding is observed, centred at a non-dimensional frequency of $\mathrm{St}_B = 0.5$ with an approximate bandwidth of $\Delta\mathrm{St}_B \approx 0.1$. Another peak is also observed at $\mathrm{St}_B \approx 0.75$, which contains less energy than the peak $\mathrm{St}_B = 0.5$. This higher frequency peak is associated with a subharmonic of the blade passage frequency, where the fundamental blade passage frequency is estimated from motor specifications to be approximately $\mathrm{St}_B = 1.4$. The peak at $\mathrm{St}_B = 0.5$ is associated with the roll-up of vortices near P_3 and P_4 observed in the instantaneous snapshots in Fig. 4.2b. A subharmonic peak is observed at a frequency of $\mathrm{St}_B = 0.25$, that initially forms at P_3 and grows compared to the highest energy peak at $\mathrm{St}_B = 0.5$, which decays as the flow develops into the wall jet from P_3 to P_5.

The emergence of more energetic and narrow peaks in the power spectra with the increase in Reynolds number suggests that the vortex shedding and merging processes have lower cycle-to-cycle variation when compared to $H/B = 2$ and $\mathrm{Re}_B = 3000$. As the flow develops downstream ($x/B > 4$), the power spectra at P_7 and P_8 show a broadband distribution of spectral energy characteristic of a developing turbulent flow compared to $\mathrm{Re}_B = 3000$. This is corroborated by the decrease in the magnitude of Reynolds stresses (Figs. 4.6b, 4.7b, and 4.8b) for $x/B > 4$ and the breakdown into small scale structures observed in the vorticity sequences (Fig. 4.2b) for $\mathrm{Re}_B = 6000$ and $H/B = 2$. Figure 4.12b, shows the power spectra in the inner shear layer. Compared to $\mathrm{Re}_B = 3000$, the spectral energy distribution in the inner shear layer is more broadband for $\mathrm{Re}_B = 6000$. The power spectra in the wall jet region prior to secondary vortex shedding at S_1 and S_2 show slight peaks in the spectra at $\mathrm{St}_B = 0.25$ and 0.5 associated with primary vortex merging and passing, respectively. The passage of primary vortices (merged and single) contributes

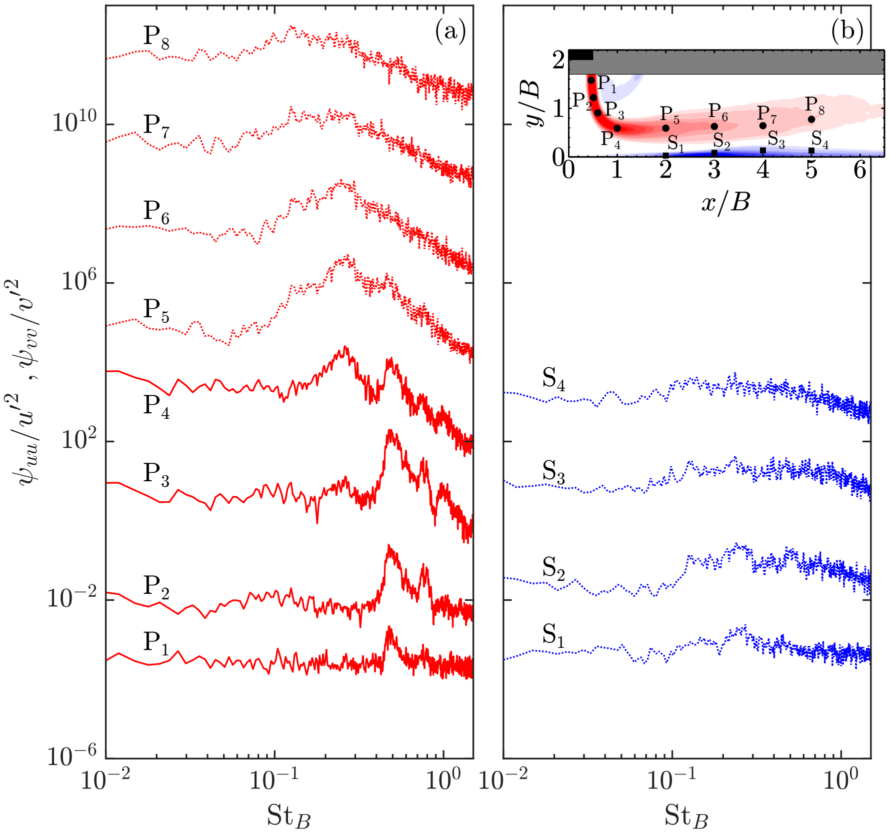

Figure 4.12: Frequency spectra of the streamwise normal fluctuating velocity for $H/B = 2$ and $\mathrm{Re}_B = 6000$ at several locations in the (a) outer shear layer and (b) inner shear layer shown in the inset image. Each spectrum is stepped by two orders of magnitude. Solid lines and dotted lines indicated spectra computed from surface parallel and normal fluctuation signals, respectively.

to the velocity fluctuations in the inner shear layer and promotes the formation of the secondary vortex as seen in the instantaneous snapshots in Fig. 4.2b. The secondary vortex shedding process shows a lower periodicity when compared to the shedding of primary vortices as no dominant peaks are observed in the spectra in the inner shear layer. Once the secondary vortex sheds, it pairs with a primary vortex in the outer shear layer before immediately breaking down in to smaller structures (Fig. 4.2b), which is reflected by the broadband spectra characteristic of a fully turbulent flow at S_3 and S_4.

Figure 4.13 shows the power spectra in outer and inner shear layer for $H/B = 4$ and $\mathrm{Re}_B = 3000$. Compared to the results for $H/B = 2$ and $\mathrm{Re}_B = 3000$, the power spectra in Fig. 4.13a show a similar trend in both the outer and inner shear layer, indicating that the structures behave similarly as the nozzle-to-plate distance is doubled from $2B$ to $4B$. This is expected since both H/B values investigated are within the potential core impingement range. The spectra in the outer shear layer show a broad peak in the mixing layer and as the flow develops, the broad peak shifts to lower frequencies due to vortex merging. Figure 4.13b features a broad peak in the inner shear layer spectra between $0.1 < \mathrm{St}_B < 0.95$, reflecting fluctuations induced by both primary and secondary vortices in the near wall region. In power spectra at P_2 to P_3 in Fig. 4.13a, two slight peaks are observed at $\mathrm{St}_B \approx 0.27$ and 0.40. From power spectra at P_2 to P_3, the higher frequency peak diminishes while the lower frequency peak is remains identifiable. This is similar to the vortex shedding behaviour observed when $H/B = 2$ and $\mathrm{Re}_B = 6000$, where the higher frequency peak is associated with vortex shedding and the lower frequency peak is associated with vortex merging; however, the lower frequency peak is not an even subharmonic of the higher frequency peak, in this case (Fig. 4.13a). Both O'Donovan & Murray [16] and Han & Goldstein [103] found odd subharmonics in the power spectra of the velocity fluctuations in the mixing layer an axisymmetric free jet, which they associated with passage of vortex merging events. Based on the shedding frequency estimates from the instantaneous snapshots in Fig. 4.3a, the spectral peak at $\mathrm{St}_B \approx 0.40$ is associated with vortex shedding, while the peak at $\mathrm{St}_B \approx 0.27$ is associated with vortex merging events.

As the Reynolds number is increased from 3000 to 6000 at $H/B = 4$, the primary vortex shedding and merging exhibits stronger periodicity, characterized by the narrower peaks of the power spectra in Fig. 4.14 at $\mathrm{St}_B = 0.25$ and 0.5, similar to when $H/B = 2$ (Fig. 4.12a). The two highest energy peaks are identified in the spectra (Fig. 4.14a) from P_1 to P_3 at $\mathrm{St}_B = 0.25$ and 0.5, associated with primary vortex merging and shedding, respectively. As vortex merging occurs in the flow reorientation region and the wall jet region, the spectra show a redistribution of the energy towards $\mathrm{St}_B = 0.25$. Downstream of P_6, the spectra are characteristic of a more turbulent flow. The spectra at S_1 (Fig. 4.14b) located in the inner shear layer at $x/B = 2$, show small spectral peaks at $\mathrm{St}_B = 0.25$ and 0.5, with the

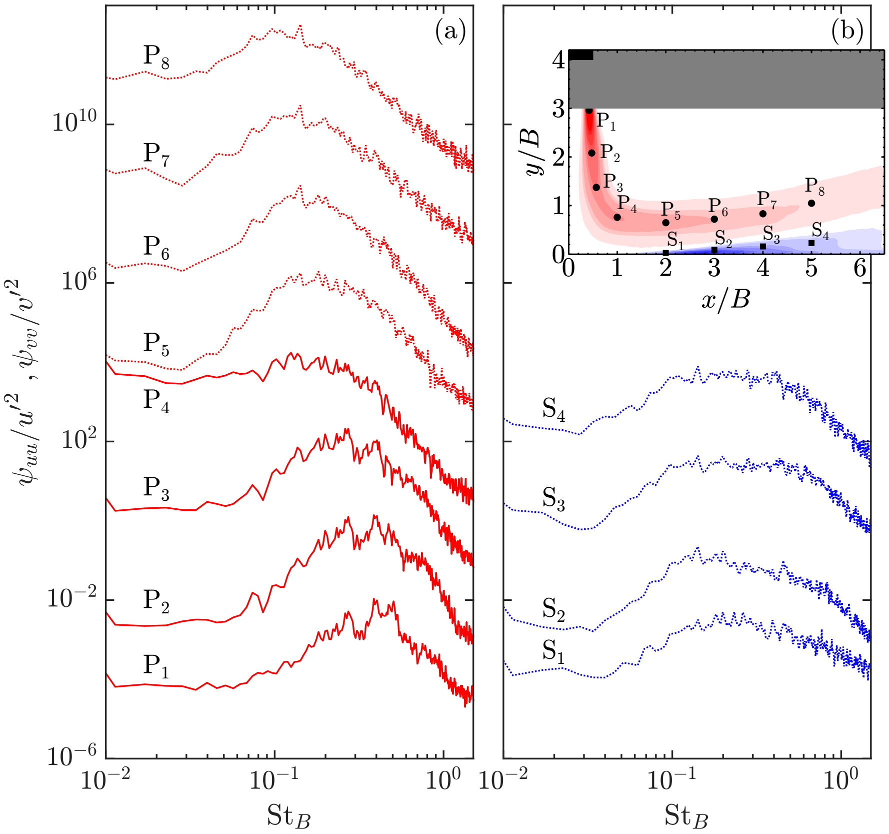

Figure 4.13: Frequency spectra of the streamwise normal fluctuating velocity for $H/B = 4$ and $\mathrm{Re}_B = 3000$ at several locations in the (a) outer shear layer and (b) inner shear layer shown in the inset image. Each spectrum is stepped by two orders of magnitude. Solid lines and dotted lines indicated spectra computed from surface parallel and normal fluctuation signals, respectively.

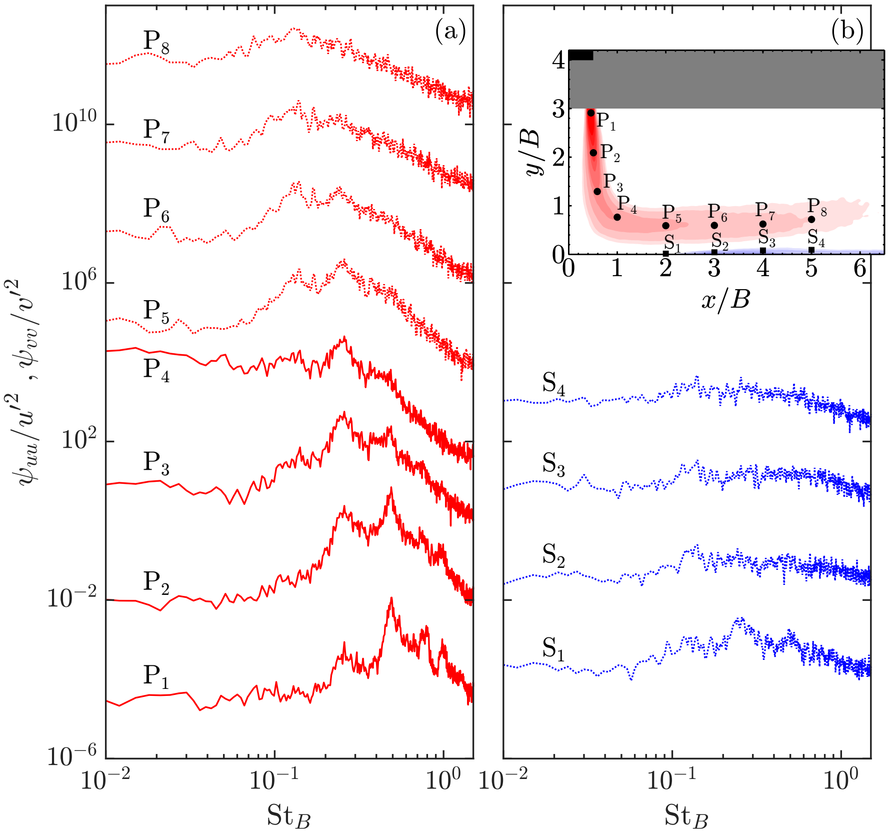

Figure 4.14: Frequency spectra of the streamwise normal fluctuating velocity for $H/B = 4$ and $\mathrm{Re}_B = 6000$ at several locations in the (a) outer shear layer and (b) inner shear layer shown in the inset image. Each spectrum is stepped by two orders of magnitude. Solid lines and dotted lines indicated spectra computed from surface parallel and normal fluctuation signals, respectively.

more energetic peak located at $\mathrm{St}_B = 0.25$. The primary vortices passing in the outer shear layer have previously merged in the free jet mixing layer, reflected by the higher spectral peaks at $\mathrm{St}_B = 0.25$, and contribute to the fluctuations in the inner shear layer. Compared to $H/B = 2$, the primary vortex merging process appears to shift upstream of the wall jet region with increasing H/B; however, the primary vortex merging events occur at approximately two nozzle diameters downstream from the shedding location along the streamwise trajectory in all cases, as characterized by the growth of the subharmonic peak and decay of the primary vortex shedding frequency.

Table 4.1 summarizes the frequencies associated with shedding and merging of primary vortices. All cases exhibited a distinct maximum in the spectral peaks but the spectra for $H/B = 2$ and $\mathrm{Re}_B = 3000$ featured a broad peak with no discernible maximum spectral energy value (Fig. 4.11), reflective of a greater cycle-to-cycle variation in the vortex shedding and merging activities when compared to other cases. No significant variations in the shedding and merging frequencies are observed with changes in nozzle-to-plate spacing. In close agreement with the results presented here, in a numerical study of a plane impinging jet at $\mathrm{Re}_B = 6000$ and $H/D = 10$, Tsubokura *et al.* [78] reported a vortex shedding frequency of $\mathrm{St}_B = 0.44$ from results obtained using DNS and LES. In an LES study by Hadžiabdić & Hanjalić [19], a vortex shedding frequency of $\mathrm{St}_D = 0.64$ is reported for an axisymmetric impinging jet at $\mathrm{Re}_D = 20\,000$ and $H/D = 2$. For a round free jet configuration in experimental studies by Yule [30] and Han & Goldstein [103], vortex shedding was observed in the frequency range of $0.6 < \mathrm{St}_D < 0.65$ with merging activities occurring between $0.33 < \mathrm{St}_D < 0.4$ for a wide range of Reynolds numbers from 8000 to 120 000. A significantly higher shedding frequency of $\mathrm{St}_D = 1.6$ is reported by O'Donovan & Murray [16] for an axisymmetric free jet, with an applicable Reynolds number range between 10 000 to 30 000. Consequently, two spectral peaks at $\mathrm{St}_D = 0.6$ and 1.1 were associated with fluctuations in the free jet mixing layer due to vortex merging events, which are significantly larger than the values in Table 4.1. The large variation in the vortex shedding and merging frequencies reported by O'Donovan & Murray [16] is attributed to the differences in the experimental configuration. The jet flow is issued from a pipe of length 20 diameters and has a turbulence intensity of up to 20% of the jet centerline velocity

Table 4.1: Characteristic frequencies associated with primary vortex shedding and merging.

		$H/B = 2$		$H/B = 4$	
		$\mathrm{Re}_B = 3000$	$\mathrm{Re}_B = 6000$	$\mathrm{Re}_B = 3000$	$\mathrm{Re}_B = 6000$
St_B	Shedding	0.40-0.50	0.50	0.40	0.50
	Merging	0.15-0.25	0.25	0.27	0.25

at $\mathrm{Re}_D = 10\,000$ [104], while in the current study, the maximum turbulence intesity for $\mathrm{Re}_B = 10\,000$ is approximately five times smaller. Without knowing the exact details of the experimental configurations, it is difficult to evaluate the differences in the shedding and merging frequencies reported by others. In general, the shedding and merging frequencies observed in the current study show good agreement with the results from both numerical and experimental studies in literature that pertain to impinging and free jets.

In order to identify regions associated with activity at frequencies corresponding to vortex shedding and merging, the velocity fluctuation fields are band-pass filtered with a bandwidth of $\Delta\mathrm{St}_B = 0.1$, centred at the shedding and merging frequencies. The band-pass filtered velocity fluctuation fields are calculated by computing the power spectra using Welch's modified averaged periodogram approach [101], using the same parameters as mentioned previously for each vector position obtained from PIV. Next, an average energy content at each vector location is obtained for the two frequency bands, representing the magnitude of band-pass filtered velocity fluctuations. The two components of the filtered velocity fluctuations are represented by $\tilde{u}$ and $\tilde{v}$ for surface parallel and normal components, respectively.

Figure 4.15 shows the spatial distribution of the fluctuating velocity components $\tilde{u}$ and $\tilde{v}$ pertaining to frequency bands associated with vortex shedding ($\mathrm{St}_B = 0.45 \pm 0.05$) and merging ($\mathrm{St}_B = 0.20 \pm 0.05$) for $\mathrm{Re}_B = 3000$ and $H/B = 2$. The surface parallel velocity fluctuations filtered at $\mathrm{St}_B = 0.45$ (Fig. 4.15a) shows localization of the energy content in the shear layer of the free jet region and in the inner shear layer of the wall jet region, which is associated with primary and secondary vortex shedding, respectively. The surface normal component of the velocity fluctuations at $\mathrm{St}_B = 0.45$ (Fig. 4.15b) shows a higher value in the fluctuations between $1 < x/B < 2$, compared to the surface parallel component, as the primary vortices shedding causes larger fluctuations in the surface normal direction. A second grouping of the energy content is observed in the wall jet region when $x/B > 3$ in the surface normal velocity fluctuations filtered at $\mathrm{St}_B = 0.45$ and is associated with the fluctuations due to the pairing and passage of primary and secondary vortices. In the fluctuations filtered at $\mathrm{St}_B = 0.45$ (Figs. 4.15a and 4.15b), the spatial growth of $\tilde{v}$ in the outer shear layer is matched by a decrease in the inner layer fluctuations due to the vortex pair being deflected away from the surface.

Relative to the velocity fluctuations filtered at the vortex shedding frequency, the energy content of the velocity fluctuations filtered at the vortex merging frequency (Figs. 4.15c and 4.15d) is higher and distributed throughout the flow reorientation region and wall jet region. In $\tilde{u}$ filtered at $\mathrm{St}_B = 0.20$, two regions of high energy content are observed in the wall jet region. The velocity fluctuation maximum near $x/B \approx 3.2$ and $y/B \approx 0.3$ is associated with vortex merging events, while the maximum in the inner shear layer is

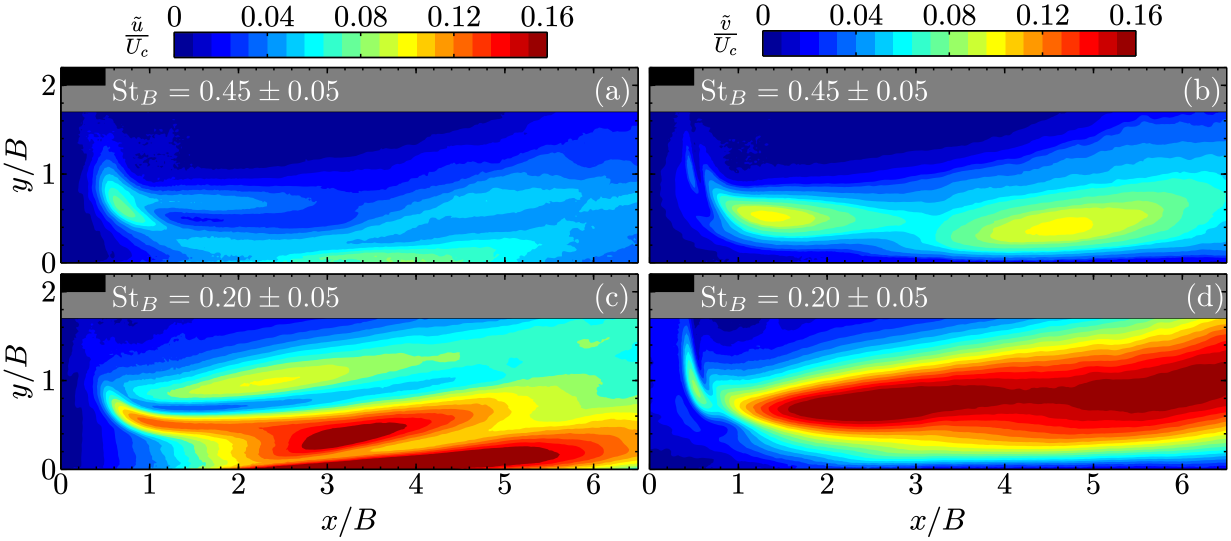

Figure 4.15: Band-pass filtered spectral energy distribution of u (left) and v (right) for $H/B = 2$ and $\mathrm{Re}_B = 3000$, at (a-b) $\mathrm{St}_B = 0.45 \pm 0.05$ and (c-d) $\mathrm{St}_B = 0.20 \pm 0.05$.

associated with secondary vortex shedding that is observed in the instantaneous snapshots in Fig. 4.2a. The $\tilde{v}$ filtered at $\mathrm{St}_B = 0.20$ (Fig. 4.15d) show a distribution of the energy content throughout the outer shear layer of the wall jet region, indicative of passage of merged primary vortices and pairing with secondary vortices shed in the same frequency band. In both frequency bands, $\tilde{u}$ (Figs. 4.15a and 4.15c) show higher energy in the inner shear layer due to secondary vortex shedding following passage of single and paired primary vortices.

Figure 4.16 shows the band-pass filtered velocity fluctuation components $\tilde{u}$ and $\tilde{v}$, as the Reynolds number is increased to 6000 at $H/B = 2$. The spatial distribution of the energy content associated with velocity fluctuations in both frequency bands are more balanced when compared to the lower Reynolds number, where the fluctuations associated with the merging frequency was dominant in the wall jet region. Figures 4.16a and 4.16b show localization of $\tilde{u}$ and $\tilde{v}$ at $\mathrm{St}_B = 0.50$ in the mixing layer and the flow reorientation region, which is associated with primary vortex shedding. The higher values of $\tilde{u}$ and $\tilde{v}$ at a Reynolds number of 6000 in a bandwidth centred at $\mathrm{St}_B = 0.50$ characterizes the lower periodicity of the shedding activities when compared to the lower Reynolds number, since more spectral energy is contained within the same bandwidth. A similar magnitude of $\tilde{u}$ is found in the inner shear layer where secondary vortices are shed as the Reynolds number is increased, however the outer shear layer shows a decrease in magnitude. This is in agreement with the surface normal filtered velocity fluctuation distribution, which shows a decrease in the magnitude from the vortex shedding location to the end of the FOV.

The decrease in $\tilde{u}$ and $\tilde{v}$ filtered at $\mathrm{St}_B = 0.50$ (Figs. 4.16a and 4.16b) when $x/B > 2$ is

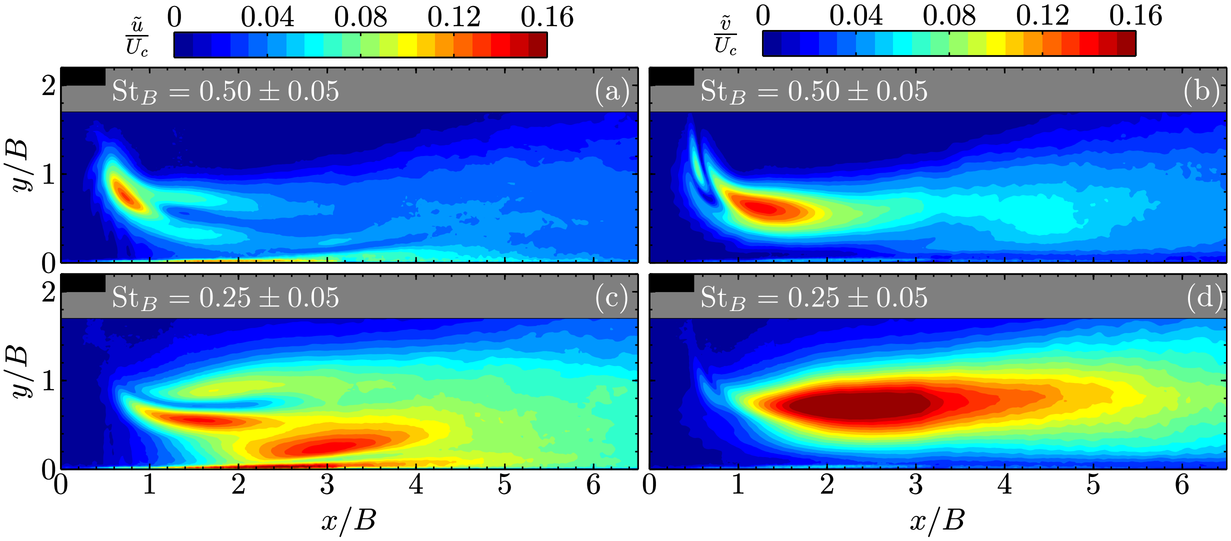

Figure 4.16: Band-pass filtered spectral energy distribution of u (left) and v (right) for $H/B = 2$ and $\mathrm{Re}_B = 6000$, at (a-b) $\mathrm{St}_B = 0.50\pm0.05$ and (c-d) $\mathrm{St}_B = 0.25\pm0.05$.

attributed to transfer of energy into the lower frequencies due to vortex merging. Although $\tilde{u}$ and $\tilde{v}$ at the subharmonic frequency band (Figs. 4.16c and 4.16d) shows a higher magnitude in the filtered velocity fluctuations between $2 \leq x/B \geq 3$, an eventual decrease in magnitude is observed beyond $x/B > 4$. The higher magnitude of $\tilde{u}$ and $\tilde{v}$ at the subharmonic frequency for $2 \leq x/B \geq 3$, corresponds to vortex merging events observed in the instantaneous snapshots. The decrease in these values are associated with vortex breakdown, which is observed for the higher Reynolds number from instantaneous snapshots (Fig. 4.2b). The spectral energy of the velocity fluctuations in the vortex shedding and frequency bands shift to frequencies that characterize the smaller scales emerging from vortex breakdown, which explains the decrease in the filtered velocity fluctuations at the vortex shedding and merging frequency bands.

Figures 4.17 and 4.18 shows the spatial distribution of the band-pass filtered velocity fluctuation for $\mathrm{Re}_B = 3000$ and 6000, respectively at $H/B = 4$. As the nozzle-to-plate spacing is increased, $\tilde{u}$ related to the vortex shedding frequency shows localization of the velocity fluctuations in the mixing layer of the free jet prior to impingement, which corresponds to the vortex shedding location observed in the instantaneous vorticity fields. Furthermore, $\tilde{u}$ at the vortex merging frequency shows a concentration of the velocity fluctuations in the free jet mixing layer, which corresponds to vortex pairing in this region [19, 78]. A vortex merging event in the free jet mixing layer can be observed in the flow visualization images for $\mathrm{Re}_B = 3000$ and $H/B = 4$ in Fig. 4.1. The $\tilde{v}$ contours at both frequency bands of interest showed activity in the potential core of the free jet region. Further, $\tilde{v}$ at the vortex merging frequency showed comparable magnitudes in the stagnation

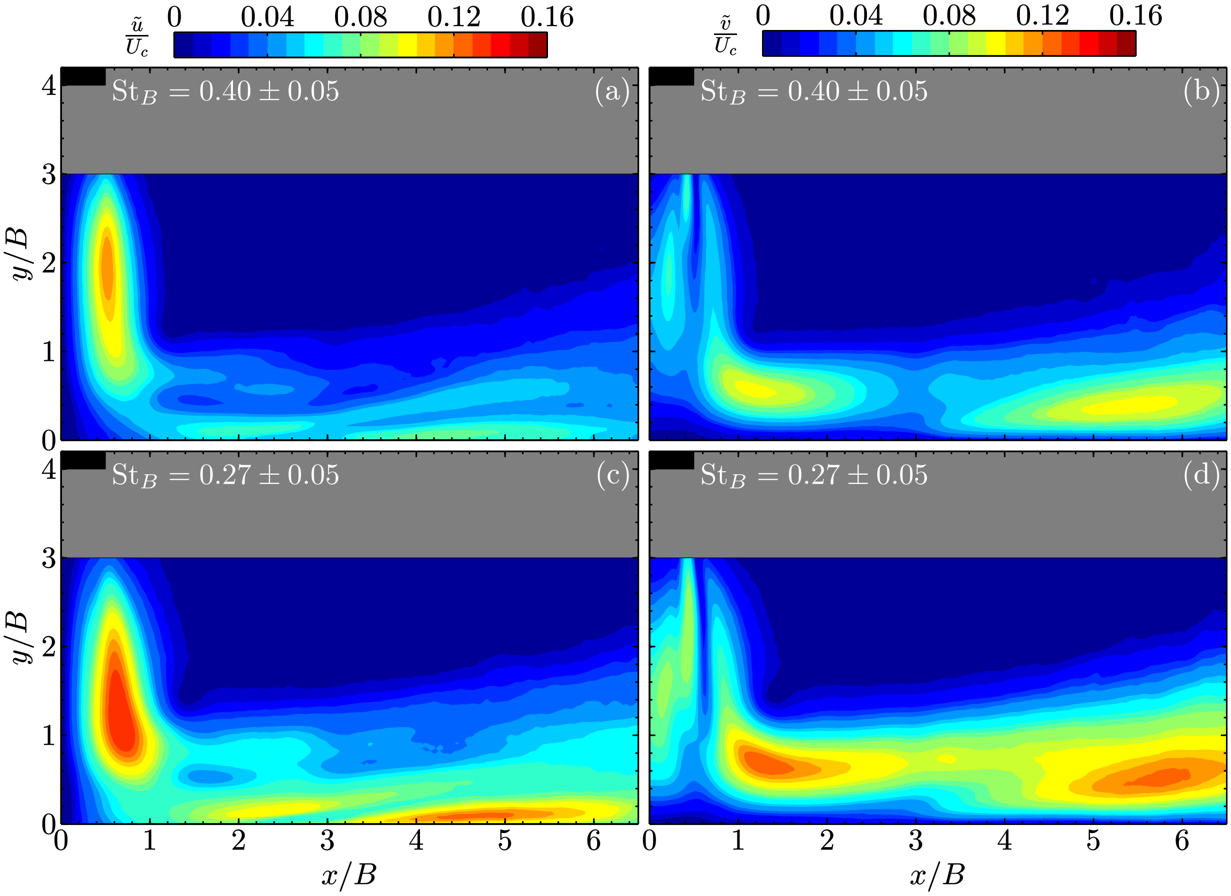

Figure 4.17: Band-pass filtered spectral energy distribution of u (left) and v (right) for $H/B = 4$ and $\mathrm{Re}_B = 3000$, at (a-b) $\mathrm{St}_B = 0.4 \pm 0.05$ and (c-d) $\mathrm{St}_B = 0.27 \pm 0.05$.

region to that of the free jet mixing layer. The instantaneous vorticity fields revealed that some primary vortices will tend to travel towards the jet centreline as they approach the impinging surface, which has been observed in the literature for similar Reynolds numbers and nozzle-to-plate spacings [13, 19, 37]. The meandering of the primary vortices through the jet centreline is then attributed to the presence of velocity fluctuations observed near the jet centreline and stagnation region when $H/B = 4$. In contrast, the velocity fluctuations at the both frequency bands are not observed near the jet centreline and stagnation region when $H/B = 2$, since vortices are shed downstream of the stagnation region. The velocity fluctuations centred at the vortex merging frequency are not associated with the flapping of the jet about the centreline axis [105], since symmetric shedding is observed for all flow conditions. Other than the differences in the free jet region, the filtered velocity fluctuations at the higher H/B show similar trends in the wall jet region compared to the lower H/B, including changes in the flow due to variations in the Reynolds number.

To extract the convective velocities and wavelengths of the primary and secondary vor-

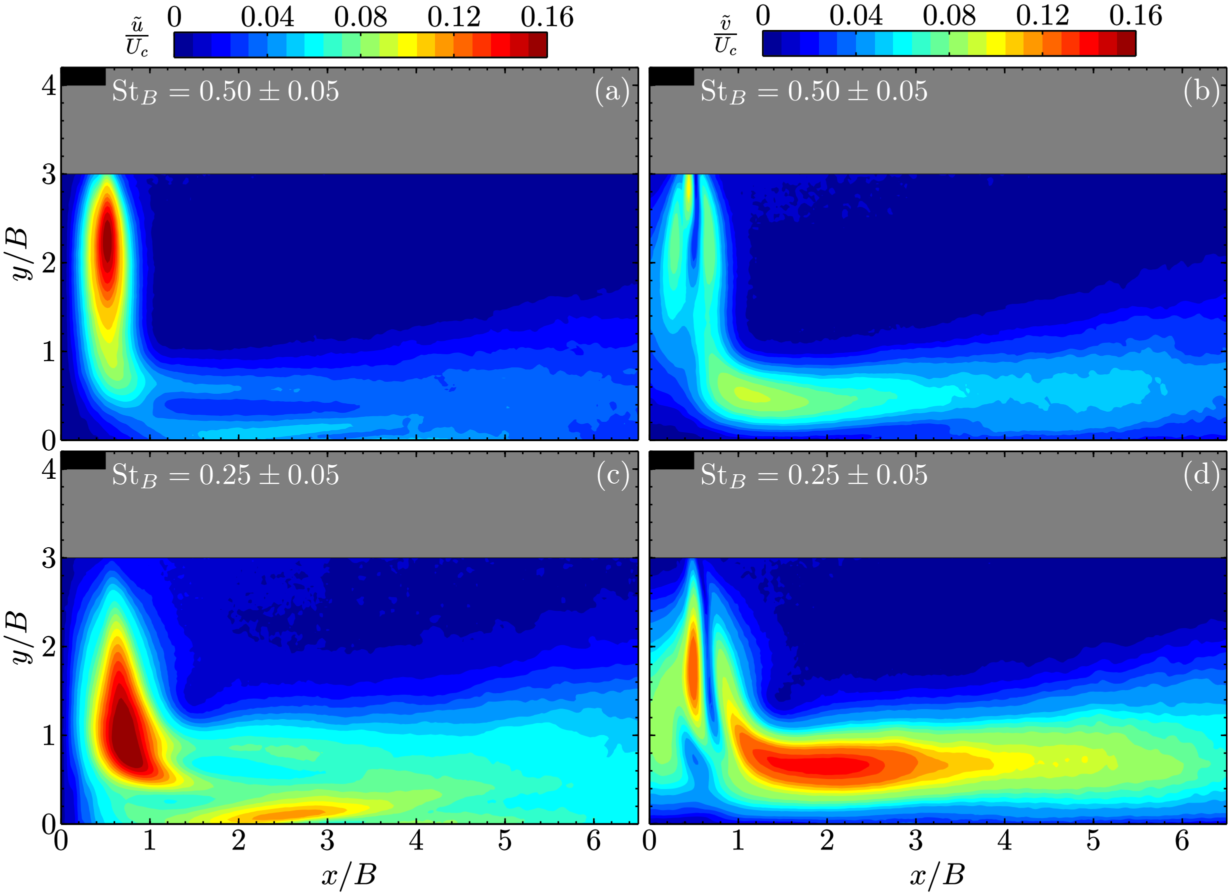

Figure 4.18: Band-pass filtered spectral energy distribution of u (left) and v (right) for $H/B = 4$ and $\mathrm{Re}_B = 6000$, at (a-b) $\mathrm{St}_B = 0.50 \pm 0.05$ and (c-d) $\mathrm{St}_B = 0.25 \pm 0.05$.

tices, two-dimensional wavenumber-frequency spectra are computed. The two-dimensional spectra are calculated along the estimated mean shear layer trajectories identified in Fig. 4.10, using the velocity magnitude fluctuations for the outer shear layer since the primary vortices travel bi-directionally. Surface normal velocity fluctuations are used along the inner shear layer trajectories associated with secondary vortices, which travel mostly in the surface parallel direction. Figures 4.19 and 4.20 show two-dimensional wavenumber-frequency spectra computed along the outer and inner shear layer trajectories, which are associated with primary and secondary vortices, respectively. In all cases, a window size of $2^6 \times 2^{10}$ points in space and time, respectively, is used with a 50% overlap, resulting in a frequency resolution of $\Delta\mathrm{St}_B = 0.006$ and 0.003 for $\mathrm{Re}_B = 3000$ and 6000, respectively, and a wavenumber resolution of $\Delta kB = 0.87$ and 0.63 for $H/B = 2$ and 4, respectively. Figures 4.19 and 4.20 do not show an appreciable difference in the energy distribution with increasing nozzle-to-plate spacing, however, with increasing Reynolds number, the energy is distributed over a broader range of wavenumbers.

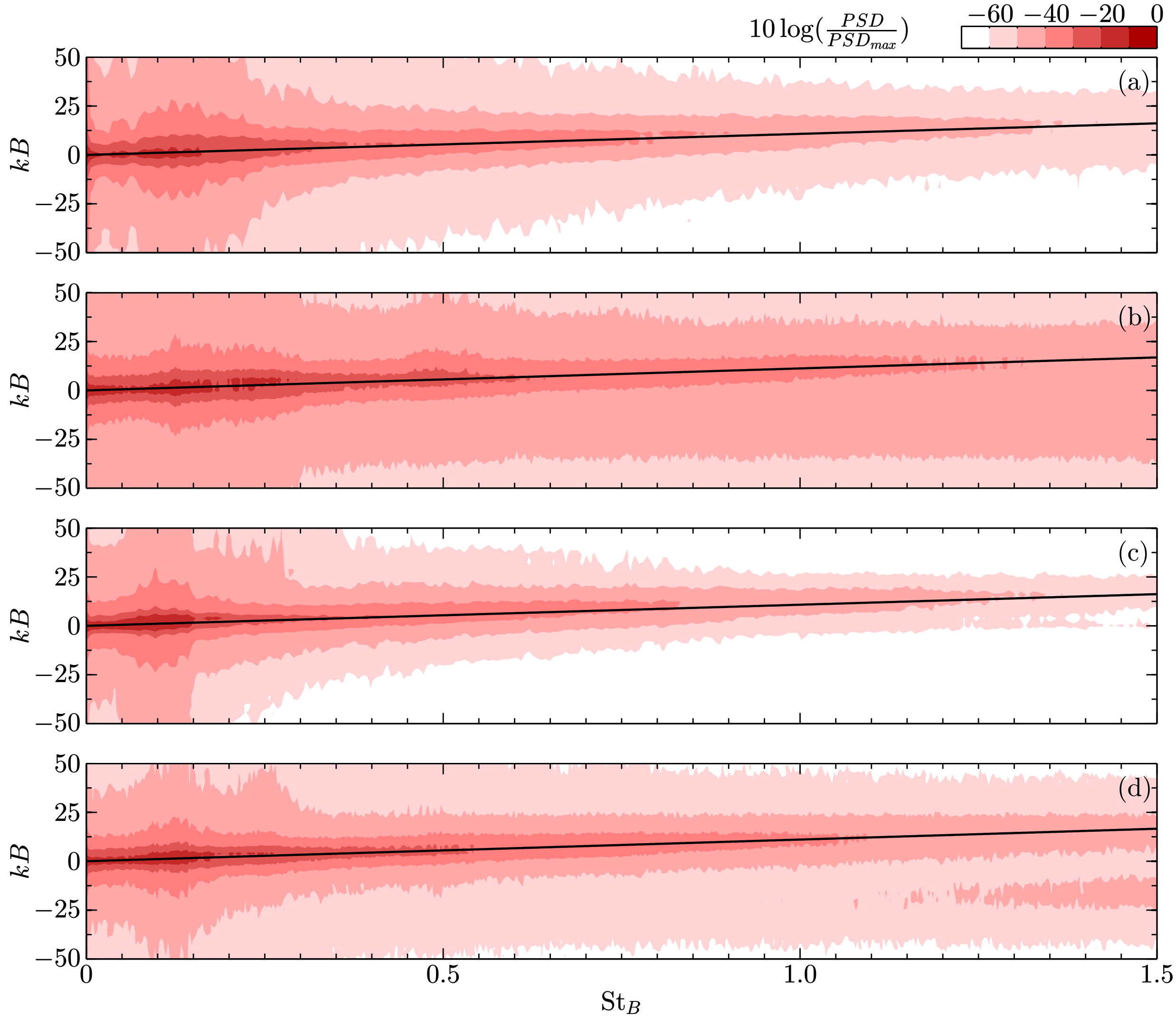

Figure 4.19: Wavenumber-Frequency spectrum of velocity magnitude fluctuations in the outer shear layer for (a) $H/B = 2$, $\mathrm{Re}_B = 3000$ (b) $H/B = 2$, $\mathrm{Re}_B = 6000$ (c) $H/B = 4$, $\mathrm{Re}_B = 3000$ (d) $H/B = 2$, $\mathrm{Re}_B = 6000$. The black solid line is a linear fit to the locations of maximum energy.

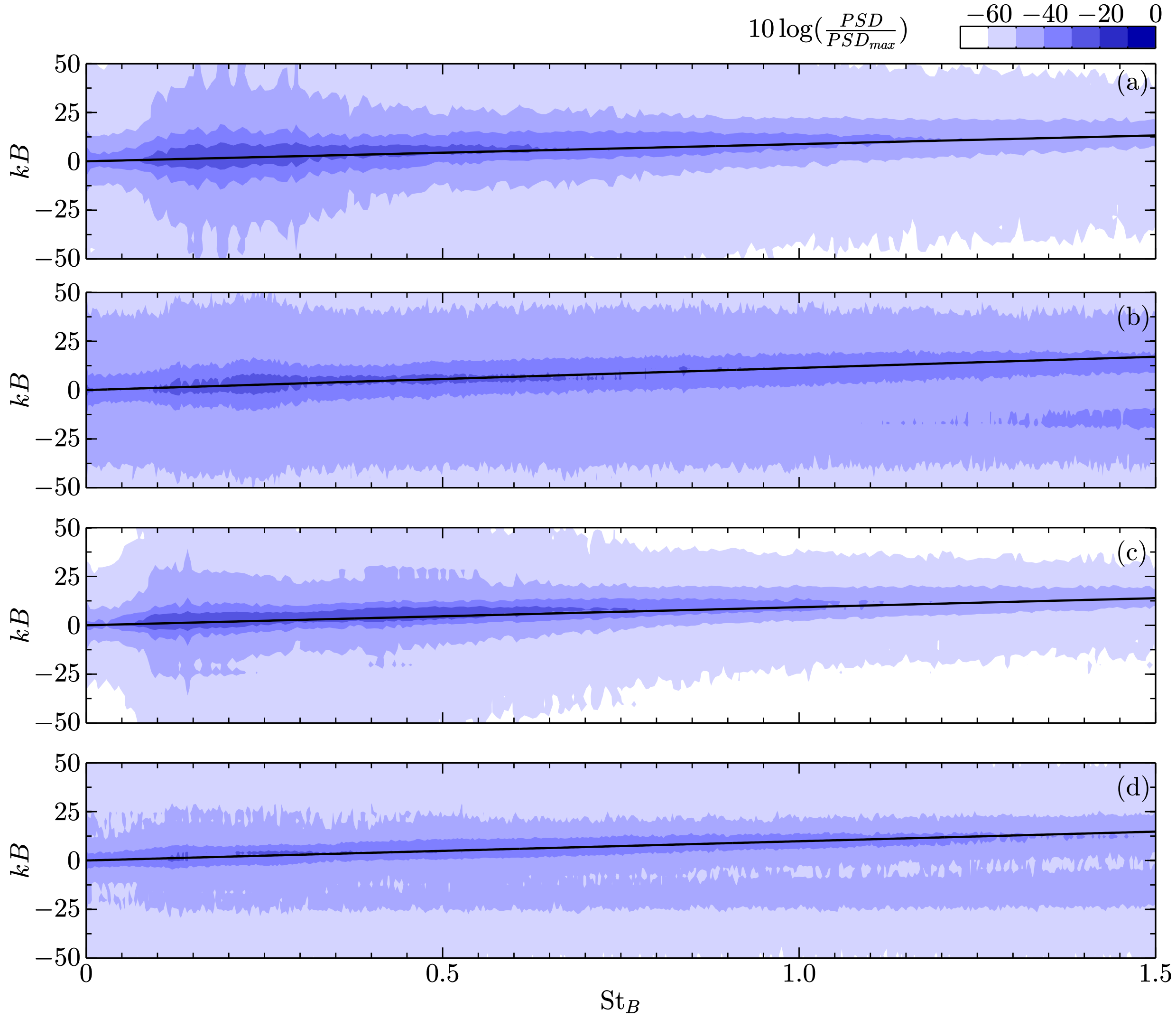

Figure 4.20: Wavenumber-Frequency spectrum of velocity magnitude fluctuations in the inner shear layer (a) $H/B = 2$, Re$_B$ = 3000 (b) $H/B = 2$, Re$_B$ = 6000 (c) $H/B = 4$, Re$_B$ = 3000, and (d) $H/B = 2$, Re$_B$ = 6000. The black solid line is a linear fit to the locations of maximum energy.

In Figs. 4.19 and 4.20, a maximum value of spectral energy shows a linear trend across a range of frequencies; this is known as the convective ridge [106] and is a feature of a convective perturbation that can be used to describe surface velocities of gravity waves [107] and convection of atmospheric waves [108]. Note that a secondary convective ridge is observed when $\mathrm{Re}_B = 6000$ at negative wavenumbers, which emerges due to aliasing. The true convective ridge is highlighted by the black lines, which is a linear fit to the locus of energy maxima, where the slope of the line represents the group velocity of a wave packet, i.e., the convective velocity of the primary and secondary vortices for impinging jet flow. Along the linear fit, the convective velocity, U_{cv} is defined by the wave equation, $U_{cv} = 2\pi f/k$, relating the perturbation wavenumber, k, and frequency, f. Convective velocities of primary and secondary vortices, normalized by the jet centreline velocity, are tabulated in Table 4.2. The convective velocities of the primary vortices do not show a discernible difference between any cases and have an average value of $U_{cv,P} = 0.57U_c$. The average convective velocity falls within the range of convective velocities reported in the literature between $0.35 < U_{cv,P}/U_c < 0.62$ for primary vortices observed in various normally impinging jet configurations [8, 75, 79, 109, 110]. In contrast, the convective velocities of the secondary vortex vary notably. In particular, a maximum value of $0.71U_c$ in the secondary vortex convective velocity is estimated for $H/B = 2$ and $\mathrm{Re}_B = 3000$. The convective velocity of the secondary vortices shows a decrease with increasing Reynolds number at each nozzle-to-plate spacing. At the higher Reynolds numbers, the secondary vortex is less pronounced and remains in the viscous inner layer of the wall jet region, where it interacts with the surface. This interaction is responsible for the reduction in the convective velocity. In general, the convective velocities of the secondary vortex is consistent with the observations of Hall & Ewing [12] and Didden & Ho [75], who estimated convective velocities through two point correlations of velocity fluctuations to be $0.6 < U_{cv,S}/U_c < 0.73$ for round impinging jets.

The two-dimensional wavenumber-frequency spectra presented in Figs. 4.19 and 4.20 also allow characteristic wavelengths, which correspond to wavenumbers at specific frequencies, to be calculated. Only the wavelengths associated with the primary vortices are discussed due to the more dominant peaks in the one-dimensional spectra presented in Figs. 4.11–14,

Table 4.2: Convective velocity estimates using wavenumber-frequency spectra.

	$H/B = 2$		$H/B = 4$	
	$\mathrm{Re}_B = 3000$	$\mathrm{Re}_B = 6000$	$\mathrm{Re}_B = 3000$	$\mathrm{Re}_B = 6000$
$U_{cv,P}/U_c$	0.58	0.56	0.58	0.57
$U_{cv,S}/U_c$	0.71	0.55	0.68	0.64

which are associated with primary vortex shedding and passing presented in Table 4.1. In the case of $H/B = 2$ and $\mathrm{Re}_B = 3000$, a characteristic frequency of $\mathrm{St}_B = 0.45$ is used, which is the median of the frequency range associated with vortex shedding. By rearranging the wave equation which defines the convective ridge (represented by the black line in Fig. 4.19), a wavenumber is determined for each shedding frequency and the wavelength, λ, is calculated according to $\lambda = 2\pi/k$. The characteristic wavelength of the primary vortex associated with the fundamental vortex shedding frequency is summarized in Table 4.3. The results show that characteristic wavelengths are most sensitive to changes in Reynolds number; with increasing Reynolds number, the characteristic wavelength decreases as the frequency of vortex shedding increases as confirmed by the series of instantaneous vorticity snapshots in Figs. 4.2 and 4.3. Furthermore, the characteristic wavelengths show good agreement with the range of vortex separation distances observed in the instantaneous snapshots presented in Figs. 4.2 and 4.3. The estimated wavelengths are marginally lower than the results for round impinging jets, which typically has a vortex separation of $1.5 < \lambda/D < 1.8$ [19, 35, 75, 111] and is attributed to the effect of the nozzle geometry as shown by Tsubokura *et al.* [78], who reported a characteristic wavelength of $\lambda/B = 1.3$ for a jet issued from a slot nozzle at $\mathrm{Re}_B = 2000$ and 6000.

To quantify the impact of the flow conditions on the secondary vortex formation process, contour plots of maximum normalized cross-correlation values are presented in Fig. 4.21. Two-point correlations are calculated between the surface normal velocity fluctuation signals at a fixed point in the wall jet region and all other points in the FOV for all time shifts, τ. The fixed point is located on the the time-averaged inner shear layer trajectory indicated by the dot-dash line in Fig. 4.21 at a surface parallel location of $x/B = 3$. The maximum correlation value of one is found at the fixed point and indicates the auto-correlation of the fluctuating velocity signal at this point. Overall, the correlation maps show a decrease in the values along the estimated outer shear layer trajectory associated with the primary vortices with increasing Reynolds number. A correlation value of 0.58 is found in the outer shear layer trajectory at surface parallel location of $x/B = 3$ for $H/B = 2$ and $\mathrm{Re}_B = 3000$

Table 4.3: Wavelengths and corresponding shedding frequencies of the primary vortices from wavenumber-frequency spectra.

H/B	Re_B	$St_{B,0}$	λ/B
2	3000	0.45	1.3
	6000	0.50	1.1
4	3000	0.40	1.5
	6000	0.50	1.1

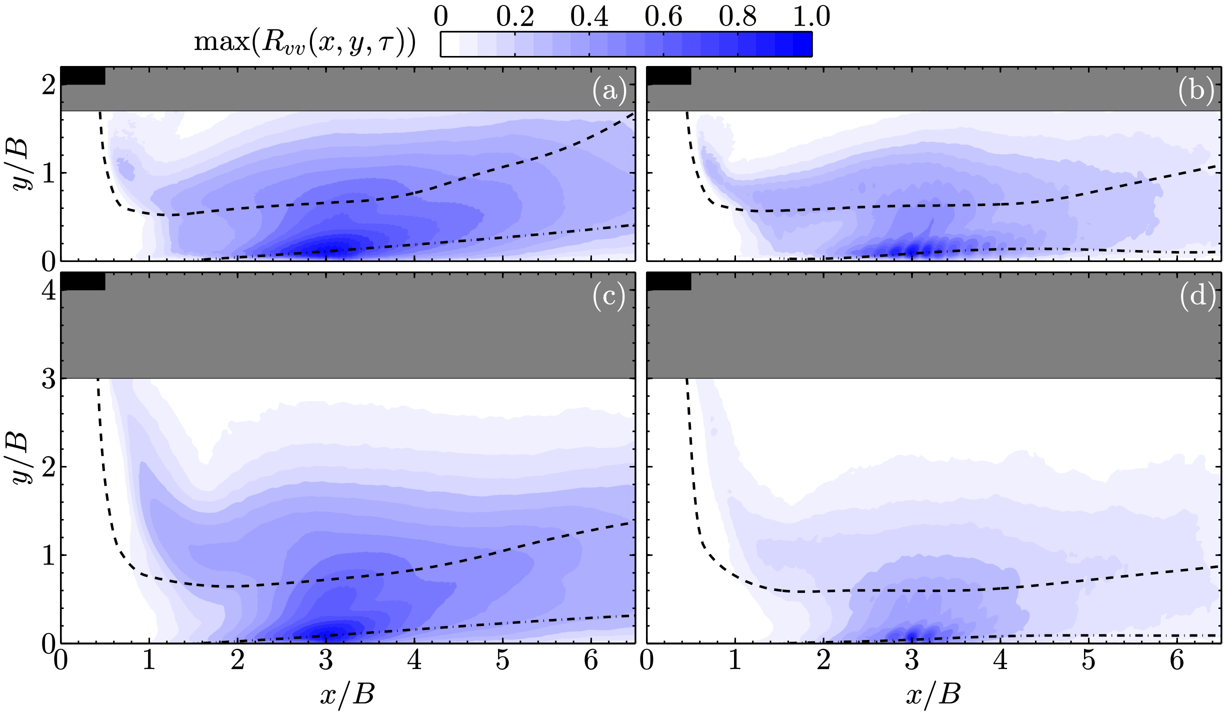

Figure 4.21: Maximum value of normalized two point correlation $R_{vv}(x, y, \tau)$ for (a) $H/B = 2$, $\mathrm{Re}_B = 3000$, (b) $H/B = 2$, $\mathrm{Re}_B = 6000$, (c) $H/B = 4$, $\mathrm{Re}_B = 3000$, and (d) $H/B = 4$, $\mathrm{Re}_B = 6000$ between a point located on the inner shear layer trajectory (−·) and all other points in domain. The outer shear layer trajectory is shown by a dashed line (−−).

in Fig. 4.21a. Figure 4.22a shows that as the primary vortex passes through $x/B = 3$, the maximum value of the correlation value is found at a negative time due to the primary vortex located slightly more upstream of $x/B = 3$ inducing the secondary vortex. As the Reynolds number is increased, the maximum correlation value at $x/B = 3$ in the outer shear layer decreases to 0.45 (Fig. 4.21b) as the secondary vortex formation is less orderly due to the more turbulent nature of the flow. Figure 4.22b shows that with increasing Reynolds number the frequency of the oscillations increase, which is consistent with the results of spectral analysis as the primary vortices are shed with lower periodic variation.

At the higher nozzle-to-plate spacing, maximum correlation values of 0.58 and 0.35 are found in the outer shear layer trajectory for $\mathrm{Re}_B = 3000$ and 6000, as observed in Figs. 4.21c and 4.21d, respectively. Similar to $H/B = 2$, the maximum correlation values found in Figs. 4.22c and 4.22d occur at similar negative time lag values, indicating the mechanism of secondary vortex formation remains unaffected by changes in nozzle-to-plate spacing, whereas increases in Reynolds number notably decreases the correlation value. The correlation maps in Fig. 4.21 also show that as the Reynolds number is increased, the correlation values downstream of $x/B = 3$ decreases, but more rapidly for $H/B = 4$,

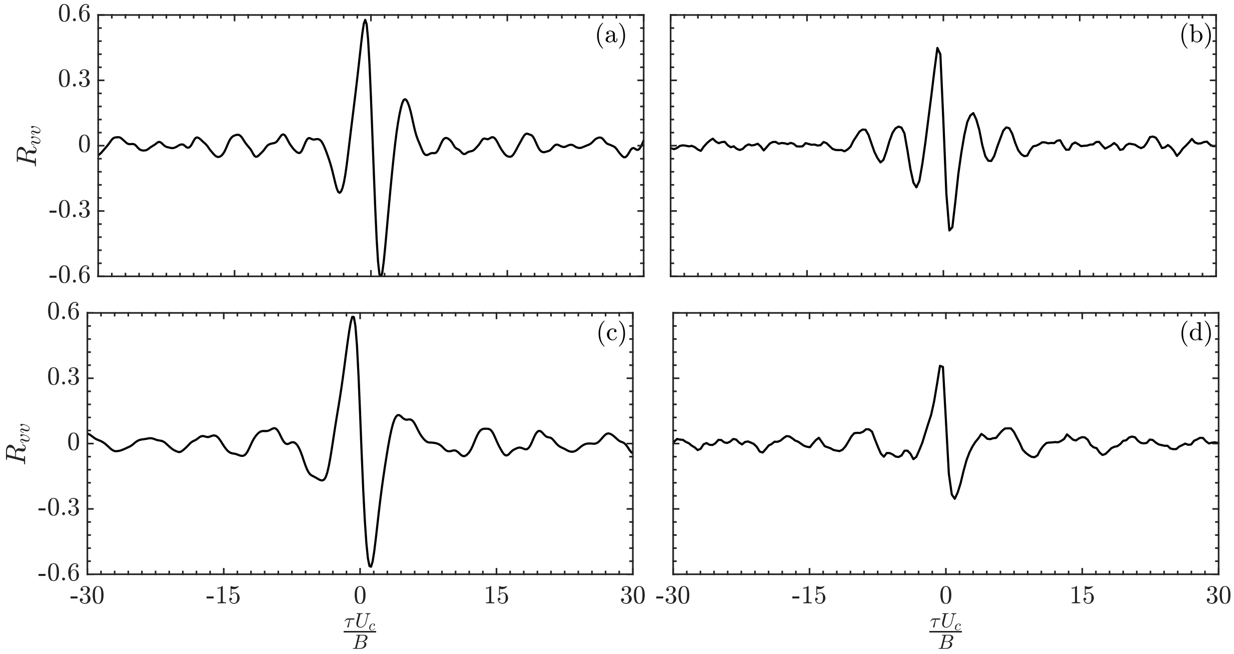

Figure 4.22: Normalized two-point correlations of surface normal velocity fluctuations associated with primary and secondary vortices for (a) $H/B = 2$, $\mathrm{Re}_B = 3000$ (b) $H/B = 2$, $\mathrm{Re}_B = 6000$ (c) $H/B = 4$, $\mathrm{Re}_B = 3000$, and (d) $H/B = 2$, $\mathrm{Re}_B = 6000$. Correlations are computed from points on the outer and inner shear layer trajectories at $x/B = 3$ (see Fig. 4.21).

marking the onset of primary and secondary vortex breakdown observed in the series of instantaneous vorticity snapshots in Figs. 4.2 and 4.3. This is consistent with the findings of Hall & Ewing [12], who found that cross-correlation values in the surface pressure of an axisymmetric impinging jet did not vary significantly between $H/D = 2$ and 4 at $\mathrm{Re}_D = 23\,300$, but at $H/D = 4$, a higher rate of decrease in the cross-correlation value were observed due to earlier vortex breakdown.

4.4 Proper Orthogonal Decomposition

Initially popularized in the fluid mechanics field, particularly in the study of turbulence and coherent structures [112], Proper Orthogonal Decomposition (POD) is a modal decomposition method that is used to extract coherent structures using experimentally or numerically derived flow fields. A brief overview on the method of snapshots used to perform the POD is provided here and the reader is directed to other publications, such as [45, 113, 114], for additional information. The method of snapshots solves the eigenvalue problem of the covariance matrix of the velocity fluctuations, $\vec{u}^{\mathsf{T}}\vec{u}$, to obtain eigenvalues, λ_i, and spatial modes, ψ_i (from the eigenvectors). The eigenvalues and spatial modes

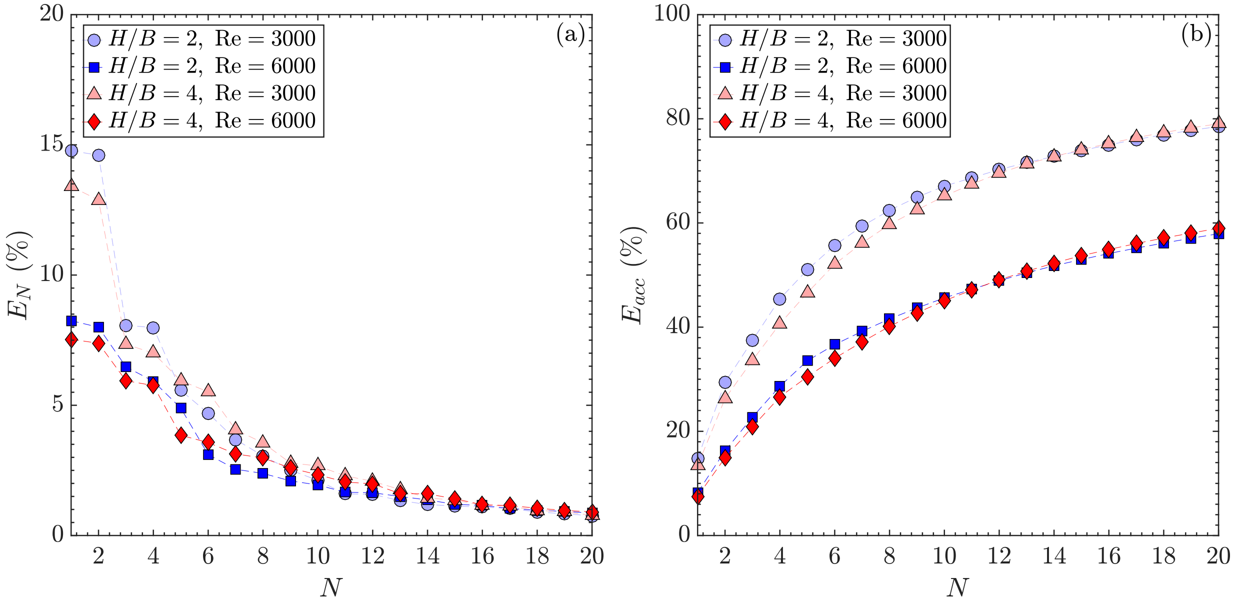

Figure 4.23: Relative turbulent kinetic energy. (a) Mode energy distribution (b) Cumulative mode energy

represent the relative turbulent kinetic energy and the spatial distribution in each mode, respectively. The modes are organized according to descending magnitude of the eigenvalues such that the most energetic flow behaviour can be extracted (*e.g.*, coherent structures). The fluctuating velocity fields can be related back to the temporal coefficients, a_i, and spatial modes, $\vec{\psi}_i$, according to $\vec{u}(x, y, t) = \sum_{i=1}^{N} a_i(t)\vec{\psi}_i(x, y)$, where i is the mode number. The temporal coefficient is a product of the spatial mode and the fluctuating velocity snapshot. In this section, the results of applying the method of snapshots to the planar velocity measurements of a normally impinging slot jet collected using time-resolved PIV at an acquisition frequency of 3.2 kHz are presented with the goal of extracting the dynamics of the most energetic coherent structures.

The relative turbulent kinetic energy of each spatial mode is shown in Fig. 4.23a, while the cumulative turbulent kinetic energy is shown in Fig. 4.23b for the first 20 POD modes. Mode pairing, indicative of oscillatory modes [115], is observed for modes one to four, manifesting in the nearly equivalent values in relative energies for these mode pairs. The energy content in the first four modes changes with H/B and Re_B. When $H/B = 2$ and $\mathrm{Re}_B = 3000$, the first two modes contain approximately 30% of the total energy. At the same H/B, when the Reynolds number is increased to 6000, the energy in the first two modes decreases to 16%. A similar trend is observed when $H/B = 4$, where the first two modes contain 26% and 15% of the total energy for $\mathrm{Re}_B = 3000$ and 6000, respectively. The increase in the Reynolds number causes the flow to become more turbulent and the relative energy to be distributed over a larger number of modes (Fig. 4.23b) [115].

A less notable effect is observed in the energy content of the first four modes when H/B is varied while Re_B is constant. At each Reynolds number, an increase in the nozzle-to-plate distance leads to a decrease in the energy content of the first four modes, with the largest relative energy difference of 1% observed for the first two spatial modes when $\mathrm{Re}_B = 3000$. At the higher nozzle-to-plate spacing, the velocity flucttutations are lower, represented by the Reynolds stress components (Figs. 4.6 and 4.7), when compared to $H/B = 2$, which lowers the energy in the first four modes at the larger impinging distance. This energy decrease is small when compared to the effect of varying the Reynolds number at each nozzle-to-plate spacing, where the difference is greater than 10% and indicates that the changes in nozzle-to-plate distance likely does not significantly affect the coherent structures.

Figure 4.24 shows power spectra of the temporal coefficients for the four most energetic modes. The pairing of the first four POD modes observed in the relative turbulent kinetic energy distribution in Fig. 4.23a is supported by the similar spectral content of the temporal

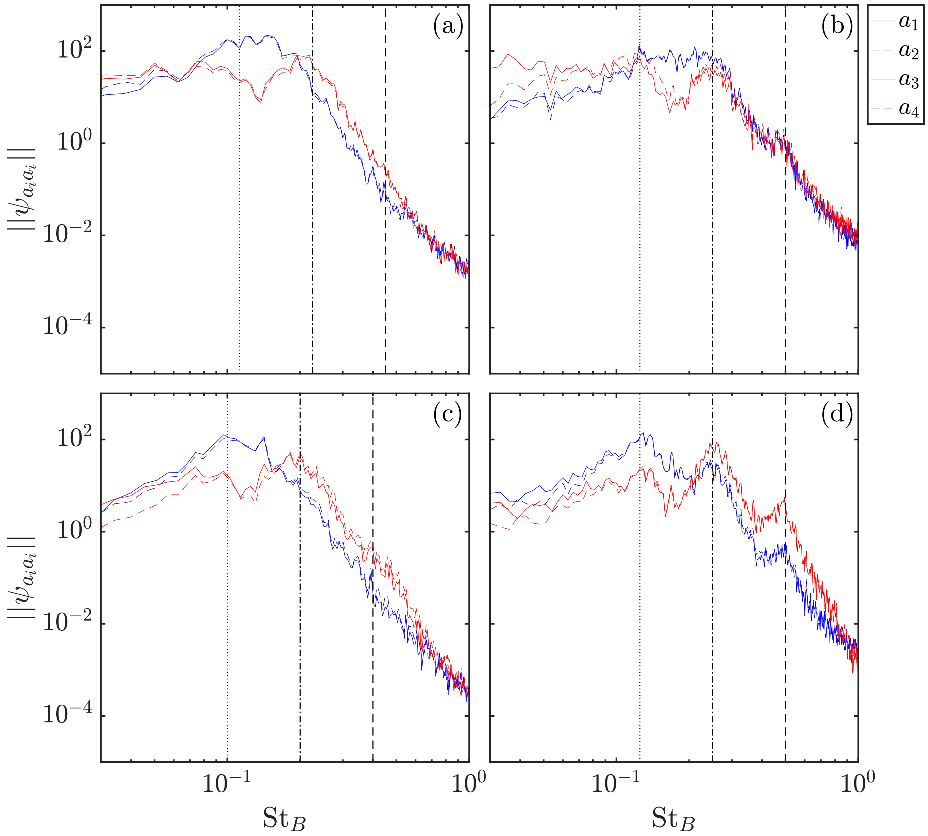

Figure 4.24: Power spectral density of the temporal coefficient a_i for mode i. The spectra corresponds to (a) $H/B = 2$, $\mathrm{Re}_B = 3000$, (b) $H/B = 2$, $\mathrm{Re}_B = 6000$, (c) $H/B = 4$, $\mathrm{Re}_B = 3000$, and (d) $H/B = 4$, $\mathrm{Re}_B = 6000$. Dashed lines indicate fundamental (−−), subharmonic (−·), and second subharmonic (···) frequencies associated with vortex shedding according to Table 4.1.

coefficients of each mode pair. At a Reynolds number of 3000, the spectra associated with the temporal coefficient of the first mode pair (Figs. 4.24a and 4.24c) show a broad peak centred at a frequency between the first and second subharmonic of the vortex shedding frequency identified in Table 4.1. As the Reynolds number is increased to 6000, the power spectra of the first mode pair (Figs. 4.24b and 4.24d) show emergence of local spectral peaks at the first subharmonic frequency of the primary vortex shedding frequency. The spectra associated with the temporal coefficient of the second mode pair show a broad peak centred at the first subharmonic of the shedding frequency in all flow conditions. An increase in Reynolds number leads to development of a spectral peak at the vortex shedding frequency and no significant changes are observed in the spectra with variations in the nozzle-to-plate spacing.

Figures 4.25 and 4.26 show the surface parallel and normal component of the first spatial mode pair, respectively, normalized by the absolute maximum eigenmode values in the domain. Similar topological features are observed in the components of the spatial modes for all flow conditions with a phase difference of approximately $\pi/2$ between modes in a mode pair and confirms the oscillatory nature of the mode pair. The spatial modes show a high concentration of energy in the wall jet region for all cases; as the Reynolds number is increased from 3000 to 6000 for each nozzle-to-plate the energy shifts upstream. Notably, when $H/B = 4$, the increase in Reynolds number causes the energy to redistribute slightly into the free jet region, which was previously observed in the band-pass filtered spectral energy distributions in Figs. 4.17 and 4.18 and suggested the shift of vortex merging upstream. The surface parallel wavelengths that are observed in the wall jet region of the first mode pair, associated with primary vortices, range between approximately 2.1 to 2.9 nozzle widths, depending on the flow conditions. The wavelength values are double that of the most energetic disturbance wavelengths at the primary vortex shedding frequency, extracted from the wavelength-frequency spectra in Fig. 4.19. A summary of the surface parallel wavelengths are provided in Table 4.4. Combined with the dominant spectral energy of the temporal coefficients observed between the first and second subharmonic of the vortex shedding frequency, this suggests that merged vortices are captured in the first mode pair.

Figures 4.27 and 4.28 show the surface parallel and normal components, respectively, of the second POD spatial mode pair. Similar to the first mode pair, the second mode pair exhibit a phase offset of $\pi/2$, but shows a decrease in the characteristic surface parallel wavelengths. As summarized in Table 4.4, the wavelength values range from 1.7 to 2.2 nozzle widths for the second mode pair, which is approximately 1.5 times the characteristic wavelengths extracted from the wavelength-frequency spectra in Fig. 4.19. However, the spectra of the temporal coefficient in Fig. 4.24 showed that the spectral

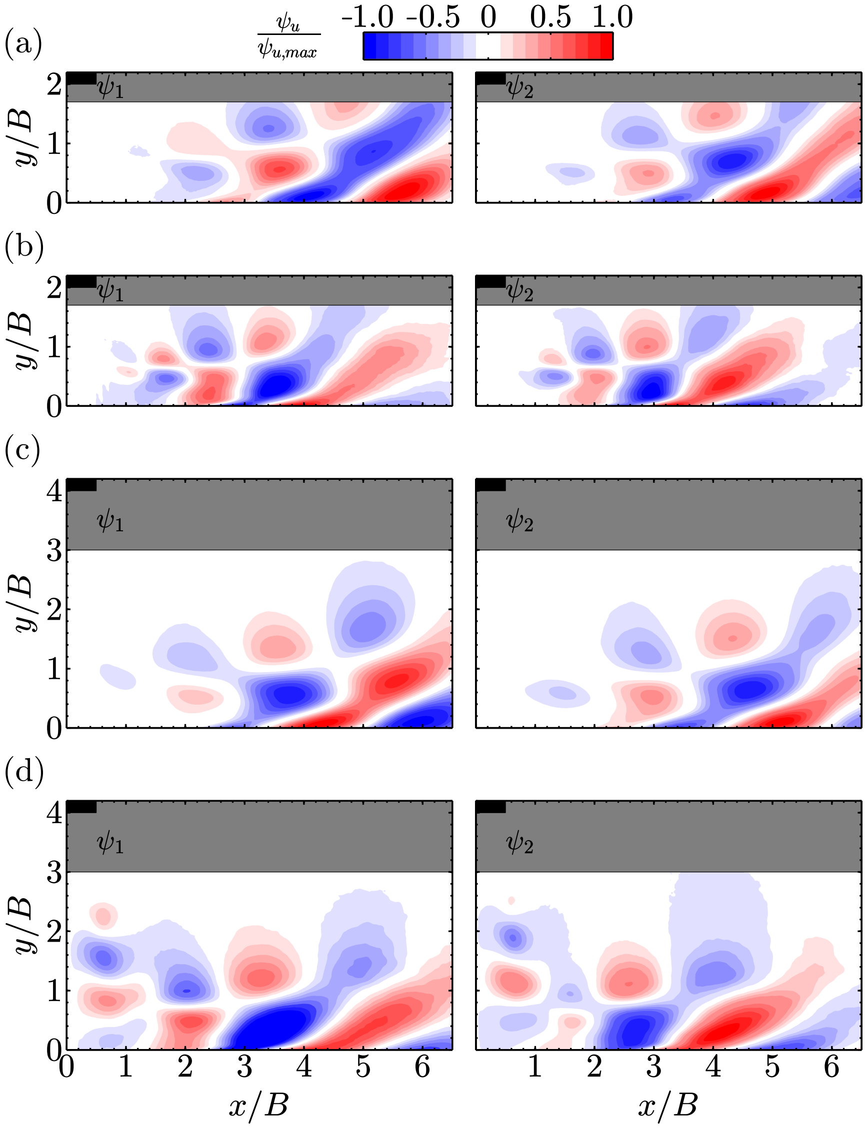

Figure 4.25: Contours of surface parallel component of first POD spatial mode pair $\psi_{1,u}$ and $\psi_{2,u}$ corresponding to (a) $H/B = 2$, $\mathrm{Re}_B = 3000$, (b) $H/B = 2$, $\mathrm{Re}_B = 6000$, (c) $H/B = 4$, $\mathrm{Re}_B = 3000$, and (d) $H/B = 4$, $\mathrm{Re}_B = 6000$.

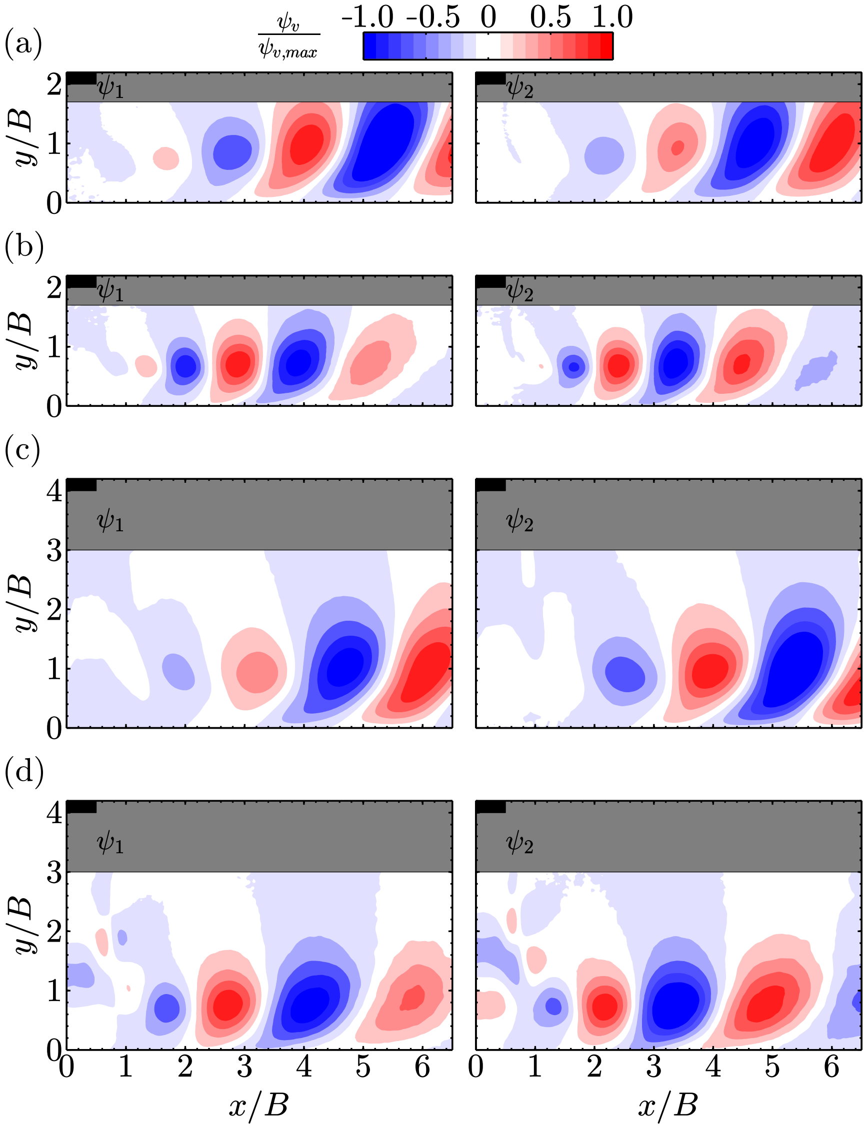

Figure 4.26: Contours of surface normal component of first POD spatial mode pair $\psi_{1,v}$ and $\psi_{2,v}$ corresponding to (a) $H/B = 2$, $\mathrm{Re}_B = 3000$, (b) $H/B = 2$, $\mathrm{Re}_B = 6000$, (c) $H/B = 4$, $\mathrm{Re}_B = 3000$, and (d) $H/B = 4$, $\mathrm{Re}_B = 6000$.

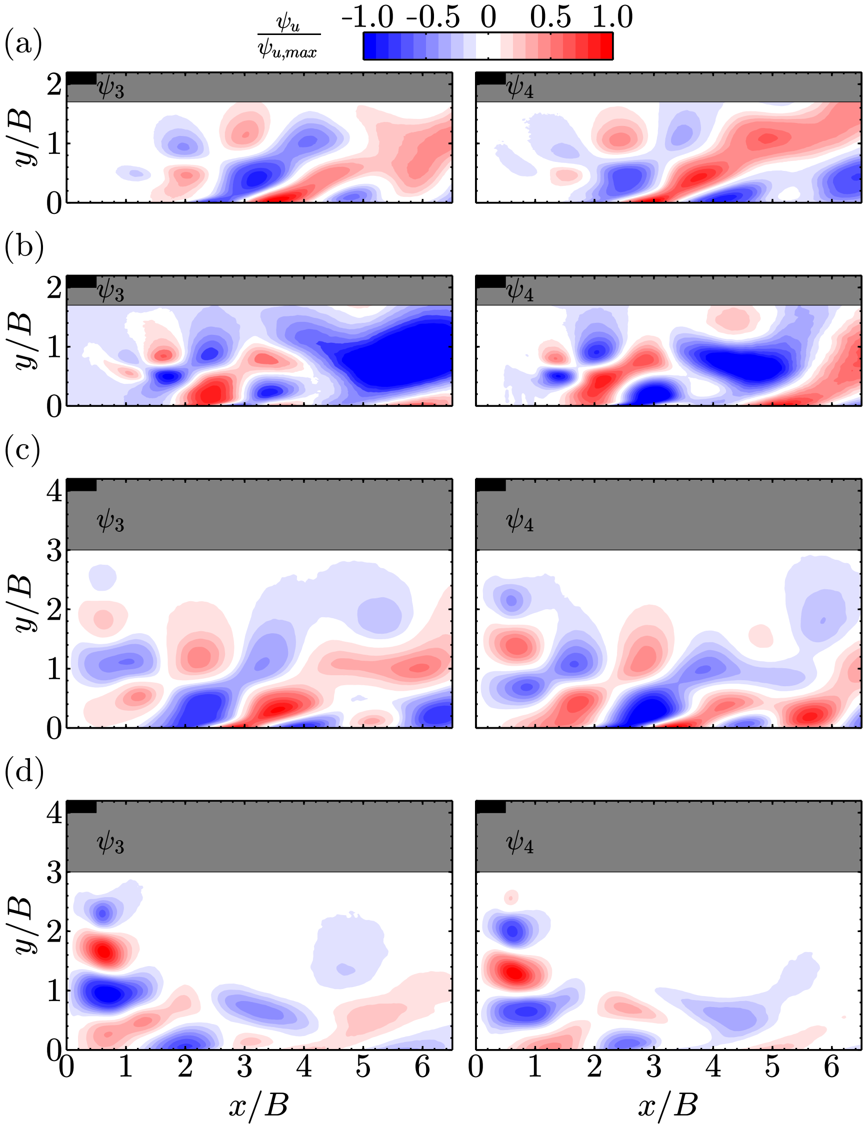

Figure 4.27: Contours of surface parallel component of second POD spatial mode pair $\psi_{3,u}$ and $\psi_{4,u}$ corresponding to (a) $H/B = 2$, $\mathrm{Re}_B = 3000$, (b) $H/B = 2$, $\mathrm{Re}_B = 6000$, (c) $H/B = 4$, $\mathrm{Re}_B = 3000$, and (d) $H/B = 4$, $\mathrm{Re}_B = 6000$.

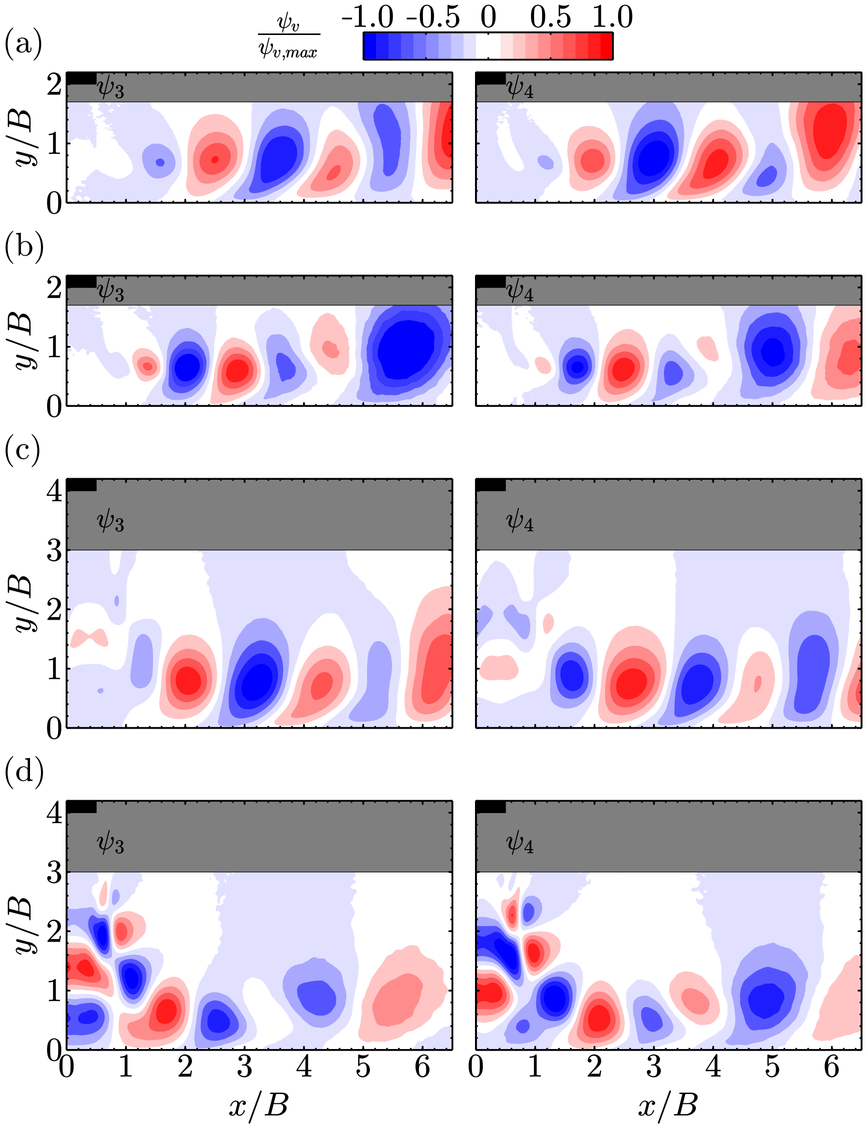

Figure 4.28: Contours of surface normal component of second POD spatial mode pair $\psi_{3,v}$ and $\psi_{4,v}$ corresponding to (a) $H/B = 2$, $\mathrm{Re}_B = 3000$, (b) $H/B = 2$, $\mathrm{Re}_B = 6000$, (c) $H/B = 4$, $\mathrm{Re}_B = 3000$, and (d) $H/B = 4$, $\mathrm{Re}_B = 6000$.

Table 4.4: Surface parallel wavelengths of the structures in the first four POD modes.

		$H/B = 2$		$H/B = 4$	
		$\mathrm{Re}_B = 3000$	$\mathrm{Re}_B = 6000$	$\mathrm{Re}_B = 3000$	$\mathrm{Re}_B = 6000$
$\frac{\lambda_x}{B}$	mode 1	2.6	2.2	2.8	2.4
	mode 2	2.6	2.1	2.9	2.1
	mode 3	2.0	2.0	2.2	2.2
	mode 4	2.1	1.7	2.1	1.9

energy was concentrated at the first subharmonic of the primary vortex shedding frequency. Furthermore, similar to the first spatial mode pair, as the Reynolds number is increased for each nozzle-to-plate spacing the energy shifts upstream. Although the characteristic wavelengths in the second mode pair are smaller compared to the first mode pair, the spatial distribution of energy and the spectra suggest that the second mode pair describes the same merged primary vortices as the first mode pair.

Both merged and non-merged primary vortices induce the formation of secondary vortices as observed from the instantaneous vorticity snapshots in Figs. 4.2 and 4.3 and a high concentration of energy is observed in the surface parallel component of the first four spatial modes (Figs. 4.25 and 4.27) near the secondary vortex shedding location in the inner shear layer when $x/B > 3$. As the secondary vortex shedding is prominent in the wall jet region, this suggests that the first two spatial mode pairs also capture the secondary vortex shedding and pairing with merged primary vortices, in addition to being linked to the convection of merged primary vortices.

Chapter 5

Conclusions

The flow development of a planar jet normally impinging on a flat plate is investigated experimentally at jet Reynolds numbers of 3000 and 6000 and nozzle-to-plate spacings of 2 and 4 nozzle widths. Using time resolved planar PIV, the velocity field is measured in a specialized open-loop jet facility that is designed, fabricated, and characterized as a part of this investigation. The PIV measurements capture the flow field up to $x/B = 6.5$ for all cases by using two cameras with overlapping FOVs and the images are later stitched to form the full FOV.

Examination of the time-averaged statistics shows the typical topological features of an impinging jet flow: free jet region, stagnation region, and wall jet region. At the smaller nozzle-to-plate spacings, the length of the potential core in the free jet region reduces, notably. The stagnation region shows no significant changes at the various flow conditions, while the wall jet region is the most sensitive to changes in the flow parameters. As the Reynolds number is increased, the growth of the wall jet decreases, potentially due to a less pronounced secondary vortex formation, which allows the mean flow to develop more parallel to the surface. The nozzle-to-plate spacing is found to have no significant effect on the development of the wall jet. Lower Reynolds stresses measured at the higher Reynolds number indicates that the flow is more turbulent and a decrease in turbulence production is observed in the later stages of the wall jet region.

Due to the Kelvin-Helmholtz instability, disturbances initiate in the mixing layer of the jet above the impingement region and grow to form primary vortices. At a Reynolds number of 3000, the primary vortex shedding occurs at a non-dimensional frequency range of $0.4 \leq \mathrm{St}_B \leq 0.5$ As the Reynolds number is increased to 6000, the primary vortex shedding process shows lower cycle-to-cycle variation, marked by the narrower peaks in the power spectra centred at $\mathrm{St}_B = 0.5$. The wavelengths of the primary vortices extracted using wavenumber-frequency spectra show that at the lower Reynolds number the primary vortices have wavelengths of $1.5B$ and $1.3B$ for $H/B = 2$ and 4, respectively. As the Reynolds number is increased, the wavelengths decrease to $1.1B$ for both nozzle-to-plate spacings, which is comparable to the wavelengths observed in the instantaneous vorticity contours. The primary vortices are convected downstream at an average value of $U_{cv,P}/U_c = 0.57$, which does not change significantly with the flow parameters tested. However, local deceleration of the primary vortex causes two consecutively shed vortices to reach a critical distance before merging to form a single vortex and is observed for all experimental conditions.

The analysis of the spatial distribution of the energy content associated with the fundamental primary vortex shedding frequency shows that the energy content of the velocity fluctuations associated with non-merged primary vortices is in the flow reorientation region above the stagnation region for $H/B = 2$ and in the free jet mixing layer for $H/B = 4$. Similarly, energy content associated with the first subharmonic of the fundamental frequency indicates that vortex merging events are mainly found throughout the wall jet region for $H/B = 2$, but start further upstream in the free jet region and continue into the wall jet region for $H/B = 4$.

The passage of primary vortices in the wall jet region induces the roll up of the wall attached vorticity in the inner shear layer, forming a secondary vortex with opposingly signed vorticity. Spectral analysis of velocity fluctuations in the inner shear layer reveals that these secondary vortices do not have a characteristic shedding frequency. The secondary vortices are convected downstream at velocities ranging between $55\% - 71\%$ of U_c and unlike the primary vortices, the secondary vortices do not undergo vortex merging. As the Reynolds number is increased, the convective velocity of the secondary vortices decreases due to the interaction with the surface.

Correlation analysis verifies that the secondary vortex formation is induced by the passage of primary vortex passage in the outer shear layer, shown by the bimodal distribution in the correlation maps. At the lower Reynolds number, maximum correlation values of 0.58 is found in the outer shear layer for $H/B = 2$ and 4, which indicates a high correlation between secondary vortex shedding following primary vortex passage. As the Reynolds number is increased, the correlation values decrease to 0.45 and 0.35 for $H/B = 2$ and 4, respectively, as the deformation of the secondary vortices increases due to the more turbulent nature of the flow.

The primary vortices and the secondary vortices form a vortex pair, which subsequently moves away from the wall at the lower Reynolds number for both nozzle-to-plate spacings. As the Reynolds number is increased, the pairing process is immediately followed by the breakdown of the vortex pair and is characterized by the redistribution of the spectral energy content across a wide band of frequencies in the later stages of the wall jet region.

Proper Orthogonal Decomposition analysis shows that as the Reynolds number is increased, the turbulent kinetic energy is divided between a larger number of modes due to the more complex behaviour of the structures, consistent with increasing turbulent nature of the flow. In contrast, the nozzle-to-plate spacing does not significantly affect the distribution of the energy between the POD modes. In all flow conditions, the first four most energetic POD modes are paired, as indicated by the equivalent relative energy, similar spectral content of the temporal coefficients, and the $\pi/2$ spatial mode phase offset of each mode pair. The surface parallel wavelengths of the primary vortices varies between 1.5 to 2 times the wavelengths of non-merged vortices extracted from the wavenumber-frequency spectra and shows that the first four modes describe merged primary vortices. This is consistent with the spectral energy content of the temporal coefficients of the first four modes, which shows a concentration of energy between the first and second subharmonics of the vortex shedding frequency. In addition to representing velocity fluctuations associated with merged primary vortices, high energy content in the spatial modes in the inner shear layer of the wall jet region suggests that the first four spatial modes also capture velocity fluctuations associated with secondary vortices.

Chapter 6

Recommendations

From the results of the present work, additional questions remain to be addressed through further analysis and investigations. The following recommendations are made for future work:

1. Perform wavelet analysis in order to examine the time variation of the frequencies at various points of interest. At $\mathrm{Re}_B = 3000$, the power spectra showed the amplification of a wide band of frequencies near the nozzle exit, making it difficult to associate a frequency band with a specific behaviour of the vortices. Revealing temporal variations in the dominant frequencies would provide additional insight into the periodicity of vortex shedding, pairing, and merging.
2. Implement vortex tracking in order to determine convective velocities and examine vortex merging events with more detail. In the current study, convective velocities along with vortex merging and breakdown are inferred from spectral analysis. Specifically for convective velocities, the waveform-frequency spectra only provide an average value, which is sensitive to the choice of the trajectory along which the spectra is computed. Vortex tracking would allow for convective velocities to be determined for each individual vortex from roll-up to breakdown, which provides information about the changes in the convective velocities. This information is missing in this study and would provide additional insight into the behaviour of vortices both in space and in time. Additionally, the impact of merging events on the shedding of secondary vortices can be determined by classifying the secondary vortex roll-up according to passage of merged and singular vortices.
3. Examine the effect of turbulence intensity at the jet exit on the vortex dynamics introduced in this study, while keeping the Reynolds number constant. The primary vortex shedding frequencies reported in this study was found to be between $0.40 < \mathrm{St}_B < 0.50$ for all flow conditions, which is lower than the values reported by a number

of studies in the literature by approximately 15% [16, 19, 30, 103]. It is not clear whether the difference in the shedding frequency is due to variations in Reynolds number or due to jet exit conditions which are unique to each experimental setup, for example, turbulence intensity.

4. Expand the parameter space to include transitional impingement and additional data points for potential core impingement in order to fully quantify the trends in the vortex dynamics identified in this study. The current study focused on potential core impingement at $H/B = 2$ and 4, but the potential core is known to extend up to 7.7 nozzle widths downstream of the jet exit for a slot jet [36–38]. It is suggested that additional date be collected at $H/B = 5$, 6, 7, and 8, which covers the flow regimes from potential core impingement to beyond transitional impingement. In order to minimize number of experiments required, numerical simulations can be employed, which can be validated using the flow conditions tested in the present investigation.

During the course of the experimental investigation, improvements to the experimental methodology were noted based on the experience gained. In accordance with these observations, the following modifications to the facility are recommended:

1. Reduce the rapid dissipation of the seeding into the ambient. The dissipation of the seeding proved to be a challenge when collecting images using PIV at low acquisition rates due to inconsistent seeding resulting in lower quality images. In the present study, the dissipation of the seeding was mitigated by collecting multiple sets of images, however, some unusable data sets were still collected due to variations in the seeding quality during data collection. A closed loop facility would improve the seeding as the dissipation in to the ambient would be reduced drastically.
2. Fabricate a new impinging plate with embedded microphones and pressure taps in order to record mean and fluctuating pressures at the surface. Pressure measurements synchronized with TR-PIV measurements can allow for enrichment of the statistics and provide added insight into vortex dynamics, such as improving the quantification of the unsteady pressure gradient that plays a role in the secondary vortex shedding as investigated by Didden & Ho [75]. Implementation of vortex tracking methods using the fluctuating pressure signal is also possible with surface pressure measurements, as discussed by Lambert [116]. Further, pressure reconstruction methods can be implemented with synchronized velocity and surface pressure measurements to obtain the pressure field of the flow.
3. Implement a cooling system and improve temperature monitoring of the facility. Currently, the temperature of the air issued by the nozzle is dependent on the temperature of the blower and heat up of flow conditioning elements in the nozzle assembly. During experiments, the experimenter is required to wait for approximately

an hour after the blower has turned on before the temperatures settle, which must be repeated for each Reynolds number tested. A heat exchanger would allow for the temperature of the air at the exit to be cooled and maintained independent of the blower temperature. For example, O'Donovan & Murray [117] maintained the temperature difference between the air from the nozzle and the ambient air to within 0.5 °C. During the study, the temperature of the exit was measured using a thermocouple that was removed before each measurement using TR-PIV. An embedded thermocouple would improve this process and remove any inconsistencies in the placement of the thermocouple, improving the accuracy of the Reynolds number calculated at the nozzle exit.

Letters of Copyright Permission

UNIVERSITY OF
WATERLOO

FACULTY OF ENGINEERING | Mechanical and Mechatronics Engineering
519-888-4567, ext. 33328 | fax 519-888-4351
mme.uwaterloo.ca

December 4, 2017

Dear Supun Pieris,

This letter serves as permission for you to publish content from the following paper, in full or in part, in your MASc thesis:

Pieris, S., Zhang, X., Yarusevych, S., and Peterson, S.D. (2017) “Evolution of coherent structures in a two-dimensional impinging jet,” 10th *International Symposium on Turbulence and Shear Flow Phenomena (TSFP-10),* July 6- 9, Chicago, IL, USA.

Sincerely yours,

Serhiy Yarusevych, Ph.D., P.Eng.,

Associate Professor
Department of Mechanical and Mechatronics Engineering
University of Waterloo
200 University Avenue West
Waterloo, On, Canada, N2L 3G1
Phone: (519) 888-4567 x35442
Fax: (519) 885-5862
E-mail: syarus@uwaterloo.ca
Web: http://www.fmrl.uwaterloo.ca

200 UNIVERSITY AVENUE WEST, WATERLOO, ON, CANADA N2L 3G1

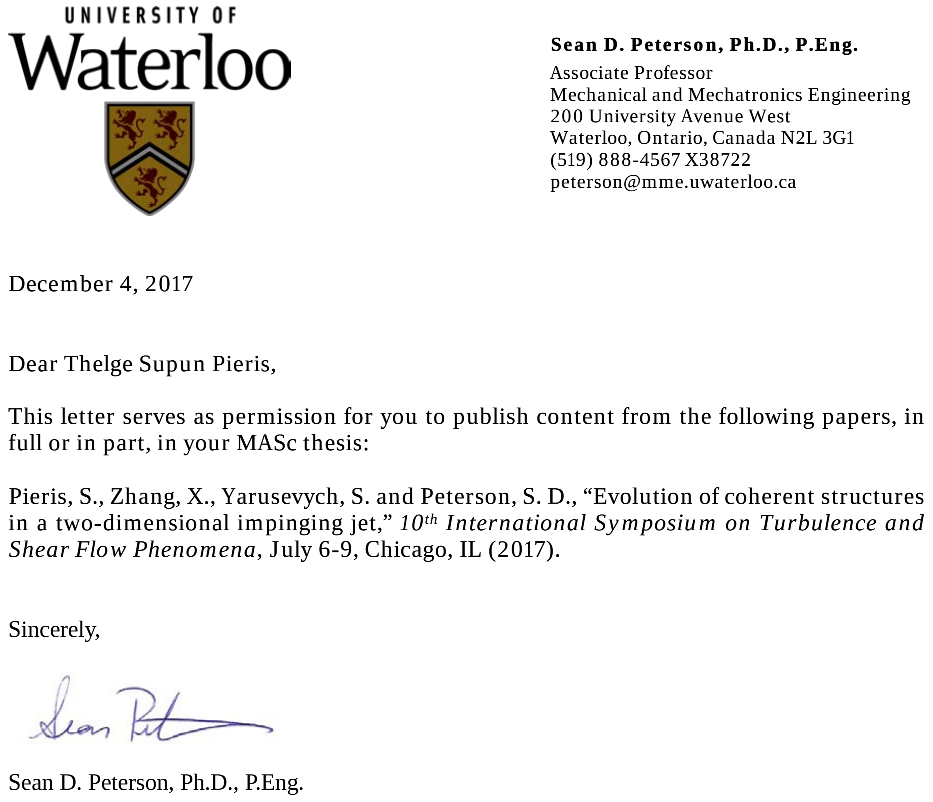

Sean D. Peterson, Ph.D., P.Eng.
Associate Professor
Mechanical and Mechatronics Engineering
200 University Avenue West
Waterloo, Ontario, Canada N2L 3G1
(519) 888-4567 X38722
peterson@mme.uwaterloo.ca

December 4, 2017

Dear Thelge Supun Pieris,

This letter serves as permission for you to publish content from the following papers, in full or in part, in your MASc thesis:

Pieris, S., Zhang, X., Yarusevych, S. and Peterson, S. D., “Evolution of coherent structures in a two-dimensional impinging jet,” *10th International Symposium on Turbulence and Shear Flow Phenomena*, July 6-9, Chicago, IL (2017).

Sincerely,

Sean D. Peterson, Ph.D., P.Eng.

References

[1] Han, B. & Goldstein, R. J. 2001 Jet Impingement Heat Transfer in Gas Turbine Systems. *Annals New York Academy of Sciences* **934** (1), 147–161. DOI. ↩

[2] Decathlon, V. V. 2007 Heat and Mass Transfer in Impingement Drying. *Drying Technology* **54** (December), 4233–4243. DOI. ↩

[3] Feng, S. S., Kuang, J. J., Wen, T., Lu, T. J., & Ichimiya, K. 2014 An experimental and numerical study of finned metal foam heat sinks under impinging air jet cooling. *International Journal of Heat and Mass Transfer* **77**, 1063–1074. DOI. ↩

[4] Yazici, H., Akcay, M., Golcu, M., Koseoglu, M., & Sekmen, Y. 2015 Experimental Investigation of Transient Temperature in Glass Tempering Processing. *Iranian Journal of Science and Technology, Transactions of Mechanical Engineering* **39.M2**, 337–349. URL. ↩

[5] Larraona, G. S., Rivas, A., Antón, R., Ramos, J. C., Pastor, I., & Moshfegh, B. 2013 Computational parametric study of an impinging jet in a cross-flow configuration for electronics cooling applications. *Applied Thermal Engineering* **52** (2), 428–438. DOI. ↩

[6] Westerweel, J., Elsinga, G. E., & Adrian, R. J. 2013 Particle Image Velocimetry for Complex and Turbulent Flows. *Annual Review of Fluid Mechanics* **45** (1), 409–436. DOI. ↩

[7] Van Oudheusden, B. W. 2013 PIV-based pressure measurement. *Measurement Science and Technology* **24** (3), 032001. DOI. ↩

[8] Violato, D., Ianiro, A., Cardone, G., & Scarano, F. 2012 Three-dimensional vortex dynamics and convective heat transfer in circular and chevron impinging jets. *International Journal of Heat and Fluid Flow* **37**, 22–36. DOI. ↩

[9] Herrero Martin, R. & Buchlin, J. 2011 Jet impingement heat transfer from lobed nozzles. *International Journal of Thermal Sciences* **50** (7), 1199–1206. DOI. ↩

[10] Kristiawan, M., Meslem, A., Nastase, I., & Sobolik, V. 2012 Wall shear rates and mass transfer in impinging jets: Comparison of circular convergent and cross-shaped orifice nozzles. *International Journal of Heat and Mass Transfer* **55** (1-3), 282–293. DOI. ↩

[11] San, J. Y. & Chen, J. J. 2014 Effects of jet-to-jet spacing and jet height on heat transfer characteristics of an impinging jet array. *International Journal of Heat and Mass Transfer* **71**, 8–17. DOI. ↩

[12] Hall, J. & Ewing, D. 2006 On the dynamics of the large-scale structures in round impinging jets. *Journal of Fluid Mechanics* **555** (2006), 439. DOI. ↩

[13] Medina, H., Benard, E., & Early, J. M. 2013 Reynolds Number Effects on Fully Developed Pulsed Jets Impinging on Flat Surfaces. *AIAA Journal* **51** (June), 1–14. DOI. ↩

[14] Xu, Z. & Hangan, H. 2008 Scale, boundary and inlet condition effects on impinging jets. *Journal of Wind Engineering and Industrial Aerodynamics* **96** (12), 2383–2402. DOI. ↩

[15] Buchlin, J. M. 2011 Convective heat rransfer in impinging- gas-jet arrangements. *Journal of Applied Fluid Mechanics* **4** (2), 137–149. URL. ↩

[16] O'Donovan, T. S. & Murray, D. B. 2007 Jet impingement heat transfer - Part II: A temporal investigation of heat transfer and local fluid velocities. *International Journal of Heat and Mass Transfer* **50** (17-18), 3302–3314. DOI. ↩

[17] Sodjavi, K., Montagné, B., Bragança, P., Meslem, A., Byrne, P., Degouet, C., & Sobolik, V. 2016 PIV and electrodiffusion diagnostics of flow field, wall shear stress and mass transfer beneath three round submerged impinging jets. *Experimental Thermal and Fluid Science* **70**, 417–436. DOI. ↩

[18] Chung, Y. M. & Luo, K. H. 2002 Unsteady Heat Transfer Analysis of an Impinging Jet. *Journal of Heat Transfer* **124** (6), 1039. DOI. ↩

[19] Hadžiabdić, M. & Hanjalić, K. 2008 Vortical structures and heat transfer in a round impinging jet. *Journal of Fluid Mechanics* **596** (2008), 221–260. DOI. ↩

[20] Kataoka, K., Suguro, M., Degawa, H., Maruo, K., & Mihata, I. 1987 The effect of surface renewal due to largescale eddies on jet impingement heat transfer. *International Journal of Heat and Mass Transfer* **30** (3), 559–567. DOI. ↩

[21] Popiel, C. O. & Trass, O. 1991 Visualization of a free and impinging round jet. *Experimental Thermal and Fluid Science* **4** (3), 253–264. DOI. ↩

[22] Roux, S., Fénot, M., Lalizel, G., Brizzi, L. E., & Dorignac, E. 2011 Experimental investigation of the flow and heat transfer of an impinging jet under acoustic excitation. *International Journal of Heat and Mass Transfer* **54** (15-16), 3277–3290. DOI. ↩

[23] Vejrazka, J., Tihon, J., Mart, P., & Sobolík, V. 2005 Effect of an external excitation on the flow structure in a circular impinging jet. *Physics of Fluids* **17** (10), 1–14. DOI. ↩

[24] Tummers, M. J., Jacobse, J., & Voorbrood, S. G. J. 2011 Turbulent flow in the near field of a round impinging jet. *International Journal of Heat and Mass Transfer* **54** (23-24), 4939–4948. DOI. ↩

[25] El Hassan, M., Assoum, H. H., Sobolik, V., Vétel, J., Abed-Meraim, K., Garon, A., & Sakout, A. 2012 Experimental investigation of the wall shear stress and the vortex dynamics in a circular impinging jet. *Experiments in Fluids* **52** (6), 1475–1489. DOI. ↩

[26] Cooper, D., Jackson, D. C., Launder, B. E., & Liao, G. X. 1993 Impinging jet studies for turbulence model assessment-I. Flow-field experiments. *International Journal of Heat and Mass Transfer* **36** (10), 2675–2684. DOI. ↩

[27] Geers, L. F. G., Tummers, M. J., & Hanjalić, K. 2004 Experimental investigation of impinging jet arrays. *Experiments in Fluids* **36** (6), 946–958. DOI. ↩

[28] Fox, M. D., Kurosaka, M., Hedges, L., & Hirano, K. 1993 The influence of vortical structures on the thermal fields of jets. *Journal of Fluid Mechanics* **255** (1993), 447–472. DOI. ↩

[29] Donaldson, C. D. & Snedeker, R. S. 1971 A study of free jet impingement. Part 1. Mean properties of free and impinging jets. *Journal of Fluid Mechanics* **45** (2), 281–319. DOI. ↩

[30] Yule, A. J. 1978 Large-scale structure in the mixing layer of a round jet. *Journal of Fluid Mechanics* **89** (03), 413. DOI. ↩

[31] Shinneeb, A.-M., Balachandar, R., & Bugg, J. D. 2008 Analysis of Coherent Structures in the Far-Field Region of an Axisymmetric Free Jet Identified Using Particle Image Velocimetry and Proper Orthogonal Decomposition. *Journal of Fluids Engineering* **130** (January 2008), 011202. DOI. ↩

[32] Fellouah, H., Ball, C. G., & Pollard, A. 2009 Reynolds number effects within the development region of a turbulent round free jet. *International Journal of Heat and Mass Transfer* **52** (17-18), 3943–3954. DOI. ↩

[33] George, W. K. 1989 The self-preservation of turbulent flows and its relation to initial conditions and coherent structures. ISBN. ↩

[34] Cornaro, C., Fleischer, A. S., & Goldstein, R. J. 1999 Flow visualization of a round jet impinging on cylindrical surfaces. *Experimental Thermal and Fluid Science* **20** (2), 66–78. DOI. ↩

[35] Hussain, A. K. M. F. & Zaman, K. B. M. Q. 1981 *The 'preferred mode' of the axisymmetric jet*, vol. 110 of number 1981, pp. 39–71. DOI. ↩

[36] Livingood, J. N. B. & Hrycak, P. 1973 Impingement heat transfer from turbulent air jets to flat plates: A literature survey. *NASA TM X-2778* (May), 43. URL. ↩

[37] Narayanan, V., Seyed-Yagoobi, J., & Page, R. H. 2004 An experimental study of fluid mechanics and heat transfer in an impinging slot jet flow. *International Journal of Heat and Mass Transfer* **47** (8-9), 1827–1845. DOI. ↩

[38] Gardon, R. & Akfirat, J. 1965 The role of turbulence in determining the heat-transfer characteristics of impinging jets. *International Journal of Heat and Mass Transfer* **8** (10), 1261–1272. DOI. ↩

[39] Hussein, H. J., Capp, S. P., & George, W. K. 1994 Velocity measurements in a high-Reynolds-number, momentum-conserving, axisymmetric, turbulent jet. *Journal of Fluid Mechanics* **258** (1994), 31–75. DOI. ↩

[40] McNaughton, K. J. & Sinclair, C. G. 1966 Submerged jets in short cylindrical flow vessels. *J. Fluid Mech.* **25** (02), 367. DOI. ↩

[41] Wille, R. 1963 Growth of velocity fluctutations leading to turbulence in a free shear layer. *Tech. rep.*, Technical Univ of Berlin (Germany). URL. ↩

[42] Lord Kelvin (Sir W. Thomson). 1871 Hydrokinetic solutions and observations. *Philosophical Magazine Series 4* **42** (281), 362–377. URL. ↩

[43] Von Helmholtz, H. 1868 On discontinuous movements of fluids. *Philosophical Magazine Series 4* **36** (244), 337–346. URL. ↩

[44] Fiedler, H. 1988 Coherent structures in turbulent flows. *Progress in Aerospace Sciences* **25** (3), 231–269. DOI. ↩

[45] Berkooz, G., Holmes, P., & Lumley, J. L. 1993 The Proper Orthogonal Decomposition in the Analysis of Turbulent Flows. *Annual Review of Fluid Mechanics* **25** (1), 539–575. DOI. ↩

[46] Quinn, W. R. 2006 Upstream nozzle shaping effects on near field flow in round turbulent free jets. *European Journal of Mechanics, B/Fluids* **25** (3), 279–301. DOI. ↩

[47] Mi, J., Nathan, G. J., & Nobes, D. S. 2001 Influence of jet exit conditions on the passive scalar field of an axisymmetric free jet. *J. Fluid Mech.* **432** (4), 878. DOI. ↩

[48] Quinn, W. R. & Militzer, J. 1989 Effects of nonparallel exit flow on round turbulent free jets. *International Journal of Heat and Fluid Flow* **10** (2), 139–145. DOI. ↩

[49] Mi, J., Nathan, G. J., & Nobes, D. S. 2001 Mixing Characteristics of Axisymmetric Free Jets From a Contoured Nozzle, an Orifice Plate and a Pipe. *Journal of Fluids Engineering* **123** (4), 878. DOI. ↩

[50] Gori, F. & Nino, E. 2003 Fluid Dynamics Measurements and Flow Visualizations of a Free Slot Jet of Air. *Fluids Engineering* 187–192. DOI. ↩

[51] Chin, D.-t. & Agarwal, M. 1991 Mass Transfer from an Oblique Impinging Slot Jet. *Journal of electrochemical society* **138** (9), 3–10. DOI. ↩

[52] Yoon, S. H., Kim, M. K., & Lee, D. H. 1997 Turbulent flow and heat transfer characteristics of a two-dimensional oblique plate impinging jet. *KSME International Journal* **11** (4), 476–483. DOI. ↩

[53] Launder, B. & Rodi, W. 1979 The turbulent wall jet. *Progress in Aerospace Sciences* **19** (2-4), 81–128. DOI. ↩

[54] Launder, B. E. & Rodi, W. 1983 The Turbulent Wall Jet Measurements and Modeling. *Annual Review of Fluid Mechanics* **15** (1), 429–459. DOI. ↩

[55] Polat, S., Huang, B., Mujumdar, A. S., & Douglas, W. J. M. 1989 Numerical flow and heat transfer under impinging jets: a review. *Annual Review of Heat Transfer* **2** (2), 157–197. DOI. ↩

[56] Gauntner, J., Livingood, J., & Hrycak, P. 1970 Survey of literature on flow characteristics of a single turbulent jet impinging on a flat plate. URL. ↩

[57] Carlomagno, G. M. & Ianiro, A. 2014 Thermo-fluid-dynamics of submerged jets impinging at short nozzle-to-plate distance: A review. *Experimental Thermal and Fluid Science* **58**, 15–35. DOI. ↩

[58] Beaubert, F. & Viazzo, S. 2003 Large eddy simulations of plane turbulent impinging jets at moderate Reynolds numbers. *International Journal of Heat and Fluid Flow* **24** (4), 512–519. DOI. ↩

[59] Maurel, S. & Solliec, C. 2001 A turbulent plane jet impinging nearby and far from a flat plate. *Experiments in Fluids* **31** (6), 687–696. DOI. ↩

[60] Zuckerman, N. & Lior, N. 2006 Jet impingement heat transfer: Physics, correlations, and numerical modeling. *Advances in Heat Transfer* **39** (C), 565–631. DOI. ↩

[61] Homann, F. 1936 Der einfluss grosser zähigkeit bei der strömung um den zylinder und um die kugel. *ZAMM-Journal of Applied Mathematics and Mechanics/Zeitschrift für Angewandte Mathematik und Mechanik* **16** (3), 153–164. DOI. ↩

[62] Liu, T. & Sullivan, J. P. 1996 Heat transfer and flow structures in an excited circular impinging jet. *Int. J. Heat Mass Transfer.* **39** (17), 3695–3706. DOI. ↩

[63] Ashforth-Frost, S. & Jambunathan, K. 1996 Effect of nozzle geometry and semi-confinement on the potential core of a turbulent axisymmetric free jet. *International Communications in Heat and Mass Transfer* **23** (2), 155–162. DOI. ↩

[64] Reichardt, H. 1943 On a new theory of free turbulence. *The Journal of the Royal Aeronautical Society* **47** (390), 167–176. DOI. ↩

[65] Martin, H. 1977 Heat and mass transfer between impinging gas jets and solid surfaces. *Advances in heat transfer* **13**, 1–60. DOI. ↩

[66] Fitzgerald, J. a. & Garimella, S. V. 1998 A study of the flow field of a confined and submerged impinging jet. *International Journal of Heat and Mass Transfer* **41** (8-9), 1025–1034. DOI. ↩

[67] Gutmark, E., Wolfshtein, M., & Wygnanski, I. 1978 The plane turbulent impinging jet. *Journal of Fluid Mechanics* **88** (1978), 737. DOI. ↩

[68] Peters, F., Ruppel, C., Javili, A., & Kunkel, T. 2008 The two-dimensional laminar wall jet. Velocity measurements compared with similarity theory. *Forschung im Ingenieurwesen/Engineering Research* **72** (1), 19–28. DOI. ↩

[69] Glauert, M. B. 1956 The wall jet. *Journal of Fluid Mechanics* **1** (06), 625. DOI. ↩

[70] Rostamy, N., Bergstrom, D. J., Sumner, D., & Bugg, J. D. 2011 The effect of surface roughness on the turbulence structure of a plane wall jet. *Physics of Fluids* **23** (8), 085103. DOI. ↩

[71] Gogineni, S. & Shih, C. 1997 Experimental investigation of the unsteady structure of a transitional plane wall jet. *Exp. Fluids* **23** (2), 121–129. DOI. ↩

[72] Eriksson, J. G., Karlsson, R. I., & Persson, J. 1998 An experimental study of a two-dimensional plane turbulent wall jet. *Experiments in Fluids* **25** (1), 50–60. DOI. ↩

[73] Fairweather, M. & Hargrave, G. 2002 Experimental investigation of an axisymmetric, impinging turbulent jet. 1. Velocity field. *Experiments in Fluids* **33**, 464–471. DOI. ↩

[74] Knowles, K. & Myszko, M. 1998 Turbulence measurements in radial wall-jets. *Experimental Thermal and Fluid Science* **17** (1-2), 71–78. DOI. ↩

[75] Didden, N. & Ho, C.-M. 1985 Unsteady separation in a boundary layer produced by an impinging jet. *Journal of Fluid Mechanics* **160**, 235–256. DOI. ↩

[76] Landreth, C. C. & Adrian, R. J. 1990 Impingement of a low Reynolds number turbulent circular jet onto a flat plate at normal incidence. *Experiments in Fluids* **9** (1-2), 74–84. DOI. ↩

[77] Terra-Homem, M. & Erdélyi, R. 2004 Absolute and convective instabilities in open shear layers. *Astronomy & Astrophysics* **413** (1), 7–15. DOI. ↩

[78] Tsubokura, M., Kobayashi, T., Taniguchi, N., & Jones, W. P. 2003 A numerical study on the eddy structures of impinging jets excited at the inlet. *International Journal of Heat and Fluid Flow* **24** (4), 500–511. DOI. ↩

[79] Ho, C.-M. & Nosseir, N. S. 1981 Dynamics of an impinging jet. Part 1. The feedback phenomenon. *Journal of Fluid Mechanics* **105** (-1), 119. DOI. ↩

[80] Violato, D. & Scarano, F. 2011 Three-dimensional evolution of flow structures in transitional circular and chevron jets. *Physics of Fluids* **23** (12). DOI. ↩

[81] Crow, S. C. & Champagne, F. H. 1971 Orderly structure in jet turbulence. *Journal of Fluid Mechanics* **48** (03), 547–591. DOI. ↩

[82] Cerretelli, C. & Williamson, C. 2003 The physical mechanism for vortex merging. *Journal of Fluid Mechanics* **475** (2003), 41–77. DOI. ↩

[83] Meunier, P., Le Dizès, S., & Leweke, T. 2005 Physics of vortex merging. *Comptes Rendus Physique* **6** (4-5 SPEC. ISS.), 431–450. DOI. ↩

[84] Le Dizès, S. & Verga, A. 2002 Viscous interactions of two co-rotating vortices before merging. *Journal of Fluid Mechanics* **467**, 389–410. DOI. ↩

[85] Meunier, P., Ehrenstein, U., Leweke, T., & Rossi, M. 2002 A merging criterion for two-dimensional co-rotating vortices. *Physics of Fluids* **14** (8), 2757–2766. DOI. ↩

[86] Law, H. S. & Masliyah, J. H. 1984 Mass transfer due to a confined laminar impinging two-dimensional jet. *International Journal of Heat and Mass Transfer* **27** (4), 529–539. DOI. ↩

[87] Mehta, R. D. & Bradshaw, P. 1979 Design Rules for Small Low Speed Wind Tunnels. URL. ↩

[88] Hassaballa, M. & Ziada, S. 2015 Self-excited oscillations of two opposing planar air jets. *Physics of Fluids* **27** (1). DOI. ↩

[89] Arthurs, D. & Ziada, S. 2012 Self-excited oscillations of a high-speed impinging planar jet. *Journal of Fluids and Structures* **34**, 236–258. DOI. ↩

[90] Bradshaw, P. & Pankhurst, R. 1964 The design of low-speed wind tunnels. *Progress in Aerospace Sciences* **5**, 1–69. DOI. ↩

[91] Hultmark, M. & Smits, A. J. 2010 Temperature corrections for constant temperature and constant current hot-wire anemometers. *Measurement Science and Technology* **21** (10), 105404. DOI. ↩

[92] Adrian, R. J. & Westerweel, J. 2011 *Particle image velocimetry*, number 30. Cambridge University Press. ISBN. ↩

[93] Prasad, A. K. 2007 *Particle Image Velocimetry*, vol. 79 of number 1 in *Experimental Fluid Mechanics*. Springer Berlin Heidelberg, pp. 51–60. DOI. ↩

[94] Willert, C. & Gharib, M. 1991 Digital particle image velocimetry. *Experiments in Fluids* **10** (4), 181–193. DOI. ↩

[95] Luca, L. D., Carlomagno, G. M., Federico, N., Energetica, D., Meola, C., de Luca, L., & Carlomagno, G. M. 1996 Influence of shear layer dynamics on impingement heat transfer. *Experimental Thermal and Fluid Science* **13** (1), 29–37. DOI. ↩

[96] Raffel, M., Willert, C. E., Wereley, S. T., & Kompenhans, J. *Post-Processing of PIV Data*. In *Particle Image Velocimetry: A Practical Guide*. Springer Berlin Heidelberg, pp. 177–208. DOI. ↩

[97] Jeong, J. & Hussain, F. 1995 On the identification of a vortex. *Journal of Fluid Mechanics* **285**, 69. DOI. ↩

[98] Baydar, E. 1999 Confined impinging air jet at low Reynolds numbers. *Experimental Thermal and Fluid Science* **19** (1), 27–33. DOI. ↩

[99] Nishino, K., Samada, M., Kasuya, K., & Torii, K. 1996 Turbulence statistics in the stagnation region of an axisymmetric impinging jet flow. *International Journal of Heat and Fluid Flow* **17** (3), 193–201. DOI. ↩

[100] Bajura, R. A. & Catalano, M. R. 1975 Transition in a two-dimensional plane wall jet. *Journal of Fluid Mechanics* **70** (04), 773. DOI. ↩

[101] Welch, P. 1967 The use of fast Fourier transform for the estimation of power spectra: A method based on time averaging over short, modified periodograms. *IEEE Transactions on Audio and Electroacoustics* **15** (2), 70–73. DOI. ↩

[102] Schadow, K. C. & Gutmark, E. 1992 Combustion instability related to vortex shedding in dump combustors and their passive control. *Progress in Energy and Combustion Science* **18** (2), 117–132. DOI. ↩

[103] Han, B. & Goldstein, R. J. 2003 Instantaneous energy separation in a free jet. Part I. Flow measurement and visualization. *International Journal of Heat and Mass Transfer* **46** (21), 3975–3981. DOI. ↩

[104] O'Donovan, T. S. & Engineering, M. 2005 *Fluid Flow and Heat Transfer of an Impinging Air Jet.* Doctor of Philosophy, University of Dublin. URL. ↩

[105] Chiriac, V. A. & Ortega, A. 2002 A numerical study of the unsteady flow and heat tranfer in a transitional confined slot jet impinging on an isothermal surface. *International Journal of Heat and Mass Transfer* **45** (6), 1237–1248. DOI. ↩

[106] Howe, M. 1998 *Acoustics of Fluid-Structure Interactions.* Cambridge Monographs on Mechanics. Cambridge University Press. ISBN. ↩

[107] Handler, R. A., Smith, G. B., & Leighton, R. I. 2001 The thermal structure of an air-water interface at low wind speeds. *Tellus, Series A: Dynamic Meteorology and Oceanography* **53** (2), 233–244. DOI. ↩

[108] Wheeler, M. & Kiladis, G. N. 1999 Convectively Coupled Equatorial Waves: Analysis of Clouds and Temperature in the Wavenumber–Frequency Domain. *Journal of the Atmospheric Sciences* **56** (3), 374–399. DOI. ↩

[109] Nosseir, N. S. & Ho, C.-M. 1982 Dynamics of an impinging jet. Part 2. The noise generation. *Journal of Fluid Mechanics* **116**, 379–391. DOI. ↩

[110] Olsson, M. & Fuchs, L. 1998 Large eddy simulations of a forced semiconfined circular impinging jet. *Physics of Fluids* **10** (2), 476–486. DOI. ↩

[111] Kim, K. C., Min, Y. U., Oh, S. J., An, N. H., Seoudi, B., Chun, H. H., & Lee, I. 2007 Time-resolved piv investigation on the unsteadiness of a low reynolds number confined impinging jet. *Journal of Visualization* **10** (4), 367–379. DOI. ↩

[112] Lumley, J. 2007 *Stochastic Tools in Turbulence.* Dover books on engineering. Dover Publications. ISBN. ↩

[113] Holmes, P. 2012 *Turbulence, Coherent Structures, Dynamical Systems and Symmetry.* Cambridge Monographs on Mechanics. Cambridge University Press. ISBN. ↩

[114] Sirovich, L. 1987 Turbulence and the dynamics of coherent structures. II. Symmetries and transformations. *Quarterly of Applied Mathematics* **45** (3), 573–582. DOI. ↩

[115] Taira, K., Brunton, S. L., Dawson, S. T. M., Rowley, C. W., Colonius, T., McKeon, B. J., Schmidt, O. T., Gordeyev, S., Theofilis, V., & Ukeiley, L. S. 2017 Modal Analysis of Fluid Flows: An Overview 1–46. URL. ↩

[116] Lambert, A. R. 2015 *Vortex Dynamics within the Laminar Separation Bubble over a NACA 0018 Airfoil at Low Reynolds Numbers*. PhD thesis. URL. ↩

[117] O'Donovan, T. S. & Murray, D. B. 2007 Jet impingement heat transfer - Part I: Mean and root-mean-square heat transfer and velocity distributions. *International Journal of Heat and Mass Transfer* **50** (17-18), 3291–3301. DOI. ↩

[118] Moffat, R. J. 1988 Describing the uncertainties in experimental results. *Experimental Thermal and Fluid Science* **1** (1), 3–17. DOI. ↩

[119] Moffat, R. J. 1985 Using Uncertainty Analysis in the Planning of an Experiment. *Journal of Fluids Engineering* **107** (2), 173. DOI. ↩

[120] Moffat, R. J. 1982 Contributions to the Theroy of Single-Sample Uncertainity Analysis. *Journal of Fluids Engineering* **104** (June), 250–258. DOI. ↩

[121] Sciacchitano, A., Wieneke, B., & Scarano, F. 2013 PIV uncertainty quantification by image matching. *Measurement Science and Technology* **24** (4), 045302. DOI. ↩

[122] Sciacchitano, A., Neal, D. R., Smith, B. L., Warner, S. O., Vlachos, P. P., Wieneke, B., & Scarano, F. 2015 Collaborative framework for PIV uncertainty quantification: comparative assessment of methods. *Measurement Science and Technology* **26** (7), 074004. DOI. ↩

Appendices

Appendix A

Jet Facility Characterization

The jet facility designed and fabricated as part of this thesis required characterization prior to any experimental investigations and pertinent characterization results are presented in this appendix. One of the metrics employed in evaluating the performance of the jet facility in the iterative fabrication stage was the spanwise uniformity of the jet exit velocity profile. The streamwise velocity at the jet exit was indirectly calculated by measuring the dynamic pressure using a pitot-static tube with an inner diameter of 1.5 mm mounted to a traverse with a resolution of 0.005 mm. All measurements were recorded using a Setra Model 239 pressure transducer with a full range of 1240 Pa connected to an NI PICe 6321 data acquisition board in order to sample the signal at a frequency of 1000 Hz for 10 000 samples. The uncertainty in the dynamic pressure measurement is mainly due to the accuracy of the measurement, which is quoted as 0.14% of the full-scale (accounting for hysteresis, non-linearity and non-repeatability), and the uncertainty is ±1.7 Pa. The associated uncertainty of the streamwise velocity is then ±2%, which does not include the uncertainty in the density of the flow due to its relatively minimal contribution. The first iteration of the jet facility utilized only two flow conditioning mesh screens and with the addition of two mesh screens and a flow redistribution (perforated) tube, the spanwise uniformity at the exit improved from ±4% to ±0.5%, which is within the uncertainty of the measurement, for 95% of the span. The increase in the spanwise uniformity is shown in Fig. A.1 by the streamwise jet exit velocity profiles across the span for the initial and final revision of the flow conditioning assembly at $\mathrm{Re}_B \approx 10\,000$.

After characterization, the jet facility was calibrated while in its free jet configuration in order to set the jet centreline velocity with high repeatability and reliability despite variations in the ambient conditions and nozzle-to-plate distance when in its impinging jet configuration. In ideal conditions with no minor losses, the Bernoulli's principle can be used to derive a relationship between the pressure drop across the contraction and the

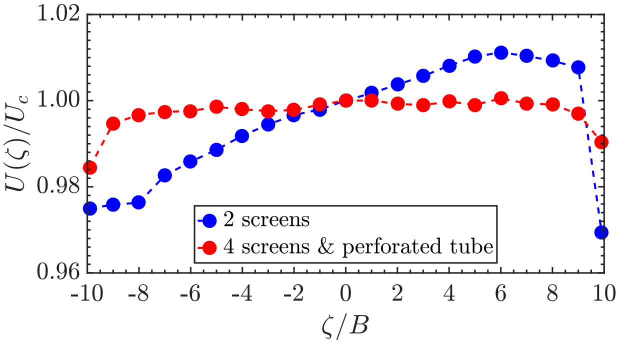

Figure A.1: Profile of normalized streamwise velocity measured across the spanwise direction at $\mathrm{Re}_B \approx 10\,000$.

jet centreline velocity. Assuming the outlet velocity of the contraction is equal to the jet centreline velocity U_c,

$$\Delta P_{con} = \frac{1}{2}\rho(U_c^2 - U_i^2) \tag{A.1}$$

where, U_i is the inlet velocity to the contraction. The inlet velocity is related to the outlet velocity of the contraction through the conservation of mass. With a known contraction ratio of 9:1, Eq. A.1 is reduced to a linear relationship between the contraction pressure drop and dynamic pressure at the jet exit centre:

$$\begin{aligned} \Delta P_{con} &= \left(1 - 1/9^2\right)\frac{1}{2}\rho U_c^2 \\ P_{dyn} &= 1.0125\Delta P_{con} \end{aligned} \tag{A.2}$$

The true relationship between the contraction pressure and dynamic pressure requires experimental measurements due to minor losses in the contraction assembly. Figure A.2 shows the measured jet exit dynamic pressure plotted against the measured contraction pressure drop. The contraction pressure drop is measured by mechanical averaging of four pressures on each side of the contraction at the inlet, while the outlet pressure is assumed to be equivalent to the ambient. The dynamic pressure is measured at the centre of the jet exit. Pressure measurements are recorded using Setra Model 239 pressure transducers with a full range of 1240 Pa and 500 Pa for the contraction pressure drop and dynamic pressure at the exit, respectively. Each measurement consists of 10 s samples acquired at 1000 Hz. The jet facility is calibrated between $2.1\,\mathrm{m\,s^{-1}}$ and $15.7\,\mathrm{m\,s^{-1}}$, corresponding to a Reynolds number range of 1700 to 11 600, which spans beyond the conditions tested in this investigation. The true calibration relationship between the jet exit dynamic pressure and the contraction pressure drop is obtained through a least-squares linear fit in Fig. A.2:

$$P_{dyn} = 1.04\Delta P_{con} - 0.14 \text{ [Pa]} \tag{A.3}$$

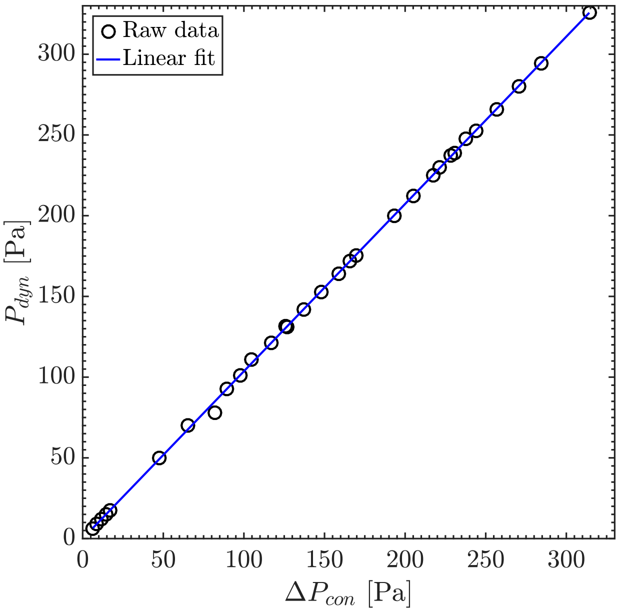

Figure A.2: Relationship between jet centreline dynamic pressure and pressure drop across the contraction. Equation for the linear fit is given in Eq. A.3.

The root-mean-squared error associated with the linear fit is ±1.3 Pa. Comparing with Eq. A.1, the calibration fit has a constant term which is associated with the losses in the jet facility contraction. The ratio of the slopes of the measured and theoretical relationships is $1.04/1.0125 = 1.02$ and indicates that the measured calibration shows good agreement with theory with less than 2% difference between theory and experiments.

Appendix B

Experimental Uncertainty

The calculation of uncertainty is important for the interpretation of results from any scientific study in order to determine its significance. The uncertainty of results presented throughout the thesis is calculated over a 95% confidence interval and for a particular quantity, β, the associated total uncertainty value is represented by ϵ_β. The root-sum-square methodology of Moffat [118–120] is used to quantify the uncertainty in ϵ_β due to n sources of error according to:

$$\epsilon_\beta = \left(\sum_{i=1}^{n} \epsilon_i^2 \right)^{1/2} . \tag{B.1}$$

It is impossible to include all sources of error in Eq. B.1, however, an effort has been made to include the major contribution to the uncertainty of results such that a conservative estimate of the uncertainty is obtained.

In addition to measured quantities, most results will include derived quantities calculated through a known relationship. If the derived quantity, β, and measured quantities, α_i, are related through $\beta = f(\alpha_1, \alpha_2, \cdots, \alpha_{n-1}, \alpha_n)$, then the uncertainty of β can be obtained using a root-sum-square method similar manner to Eq. B.1:

$$\epsilon_\beta = \left[\left(\frac{\partial G}{\partial \alpha_1} \epsilon_{\alpha_1} \right)^2 + \left(\frac{\partial G}{\partial \alpha_2} \epsilon_{\alpha_2} \right)^2 + \cdots + \left(\frac{\partial G}{\partial \alpha_{n-1}} \epsilon_{\alpha_{n-1}} \right)^2 + \left(\frac{\partial G}{\partial \alpha_n} \epsilon_{\alpha_n} \right)^2 \right]^{1/2} . \tag{B.2}$$

In Eq. B.2, the partial derivatives are known as the sensitivity coefficients for β with respect to a measurement α_i [118]. It is extremely convenient to implement Eq. B.2 for a known relationship, f, unfortunately, most results are obtained through a complex analytical process which is not easily described by a single function. Further, the discrete nature of the measured quantities in this investigation leads to numerical approximations when analyzing the data, which has an associated error. In such instances, an approach known as "method of sequential perturbation" is implemented [118, 119], in order to propagate the uncertainty in the measured quantities, α_i to the derived quantity, β. The general approach is as follows:

1. Calculate the result using α_i without uncertainties, which is denoted β_0.
2. For each i, add ϵ_{α_i} to α_i to calculate β_{i+}, while all other measure quantities are unchanged. This is repeated for subtracting ϵ_{α_i} from α_i, to calculate β_{i-}. The differences $\beta_{i+} - \beta_0$ and $\beta_{i-} - \beta_0$ are a measure of the uncertainty interval and the average of the absolute value of the differences is used as a characteristic uncertainty contribution by α_i.
3. Calculate the total uncertainty using Eq. B.1.

The uncertainty analysis presented in Appendices B.1 and B.2 is summarized in Table B.1 for all flow conditions tested in the study.

Table B.1: Uncertainty estimates of experimental conditions PIV measurements.

Parameter	Uncertainty*			
	$H/B = 2$		$H/B = 4$	
	$\mathrm{Re}_B = 3000$	$\mathrm{Re}_B = 6000$	$\mathrm{Re}_B = 3000$	$\mathrm{Re}_B = 6000$
U_c	±6.7%	±1.7%	±6.2%	±1.7%
Re_B	±6.8%	±2.0%	±6.3%	±2.0%
H	±5.0%		±2.5%	
θ	±0.07°			
U	$\leq \pm 6\%$ (of U_c)			
u'	$\leq \pm 8\%$ (of $max(u')$)			
v'	$\leq \pm 4\%$ (of $max(v')$)			
$\mathrm{d}y_{1/2}/\mathrm{d}x$	±6%	±12%	±5%	±8%
$St_{B,0}$	±0.3%	±0.75%	±0.3%	±0.75%
$U_{cv,P}$	±21%	±14%	±20%	±10%
$U_{cv,S}$	±24%	±9%	±27%	±12%
k_0B	±1.4%	±0.6%	±1.4%	±0.5%
λ_0/B	±1.4%	±0.6%	±1.4%	±0.5%

* All uncertainty estimates are within a 95% confidence interval

B.1 Experimental Conditions

The experimental conditions consists of the nozzle width based Reynolds number, Re_B, and nozzle-to-plate distance, H. Additionally, the angle of impingement, θ, is held constant such that the jet impinged normally on the plate. The associated uncertainties of these three parameters are presented in this section.

The nozzle width based Reynolds number is calculated from the jet centreline velocity, U_c, nozzle width, B, and dynamic viscosity, ν, that each have associated uncertainties. The nozzle width is a product of the CNC machining tolerances of the jet nozzle Assembly, which is known with high precision and is not expected contribute to the uncertainty of the Reynolds number, resulting in $\epsilon_B \approx 0$. The kinematic viscosity is related to density, ρ, and dynamic viscosity, μ, by its ratio, $\nu = \mu/\rho$, which are functions of temperature and pressure and are measured using instruments that have an associated relative uncertainty of $\pm 0.73\%$ and $\pm 0.14\%$, respectively. Density is a function of both temperature and pressure, while dynamic viscosity is only dependent on temperature, hence the uncertainty of temperature is expected to contribute more than the uncertainty in the pressure when calculating ν. The propogation of error through the application of Eq. B.2 results in $\epsilon_\nu/\nu = \pm 1\%$. As outlined in Appendix A, the pressure drop across the jet facility contraction is measured and the centerline dynamic pressure is calculated through a known calibration, which is used with the Bernoulli's principle to obtain the jet centerline velocity indirectly. The uncertainty in the dynamic pressure is calculated to be $\epsilon_{P_{dyn}} = \pm 2.2\,\mathrm{Pa}$, which takes into account the uncertainty of the measured contraction pressure and root-mean-square error (RSME) of the calibration fit. The calculation of relative uncertainty of the jet centerline velocity incorporates the uncertainty of the dynamic pressure as well as the density (due to the Bernoulli's principle) through Eq. B.2 and results in $\pm 1.7\% < \epsilon_{U_c}/U_c < \pm 6.7\%$. By applying Eq. B.2 once mroe, the relative uncertainty of the Reynolds number is determined to be $\pm 2.0\% < \epsilon_{\mathrm{Re}_B}/\mathrm{Re}_B < \pm 6.8\%$.

The nozzle-to-plate distance is set using a ruler with a resolution of 1 mm by measuring from the nozzle exit to the impingement surface. Due to the two measurements, the associated uncertainty in the nozzle-to-plate distance is then $\epsilon_H = \pm 1\,\mathrm{mm}$ and less than 5.0% for the two nozzle-to-plate distances tested.

The impingement angle is set using a digital protractor with an angular resolution of 0.1° and a corresponding uncertainty of $\pm 0.05^\circ$, however, two measurements are required, one on the nozzle exit and another on the impingement surface in order ensure the relative angle between the two surfaces is approximately zero. Using Eq. B.1, this results in an uncertainty of $\epsilon_\theta = \pm 0.07^\circ$

B.2 PIV Measurements

Error estimation of PIV measurements and derived quantities is a challenging task due to a multitude of factors that contribute to PIV uncertainty stemming from the high complexity of the measurement system. The uncertainty estimate of the random error in PIV is quantified in this investigation using the particle disparity method [121, 122]. In its essence, the particle disparity method is *a posteriori*, since the measured velocity field is used as an input in the error estimation process. For each interrogation window of an image pair, the measured velocity field is used to predict the displacement of particles from the first image to the second image. An unavoidable disparity between the predicted and the actual displacements arises due to out-of-plane particle motions, variation of background intensity and camera sensor noise levels, and high gradients in velocity [121]. The error in the velocity is extracted by applying statistical methods to the disparity matrix, which describes the residual displacements between identified particle pairs. An advantage of the particle disparity method is that the uncertainty in the instantaneous, mean, and fluctuating velocity fields can be easily determined.

The first column of Fig. B.1 shows the random error estimates in the velocity magnitude for PIV images acquired a rate of $f = 125$Hz. Overall, the uncertainty in the velocity magnitude is the lowest when $H/B = 2$ (Figs. B.1a and B.1d). For both Reynolds numbers when $H/B = 2$, an uncertainty maximum of $\epsilon_{\|\vec{U}\|}/U_c = 10\%$ is observed near the nozzle exit and is associated with inconsistent seeding due to bloackage of the flow entrainment by the nozzle and laser light reflections. The uncertainty at the impinging surface is also higher when comapred to the rest of the flow field for similar reseasons. As the nozzle-to-plate spacing is increased to $H/B = 4$, the uncertainty in the velocity magnitude shows an overall increase in magnitude and its spatial distrubiton in Figs. B.1g and B.1j. This is associated with the larger spread of the laser beam when comapred to $H/B = 2$, which leads to decrease quality of the light near the edges of the FOV. Notably, for $H/B = 4$ and $\mathrm{Re}_B = 6000$ (Fig. B.1j), the uncertainty distribution in the velocity magnitude is drastically increased where flow entrainment occurs above the wall jet region. This is attributed to the increase in ambient seeding disspation at the higher Reynolds number and decrease in the laser light intensity due to the lower frame separation time (Table 3.1). In the regions relevent to the analysis presented in this work, the characteristic relative uncertainty of the velocity magnitude is less than $\pm 6\%$ of U_c for all test cases.

The uncertainty in the surface parallel and normal components of RMS velocity is shown in the second and third column of Fig. B.1, respectively. The uncertainty in the surface parallel and normal RMS velocities have a similar distribution to the uncertainty of the velocity magnitude, however, the relative uncertainty in the surface normal RMS

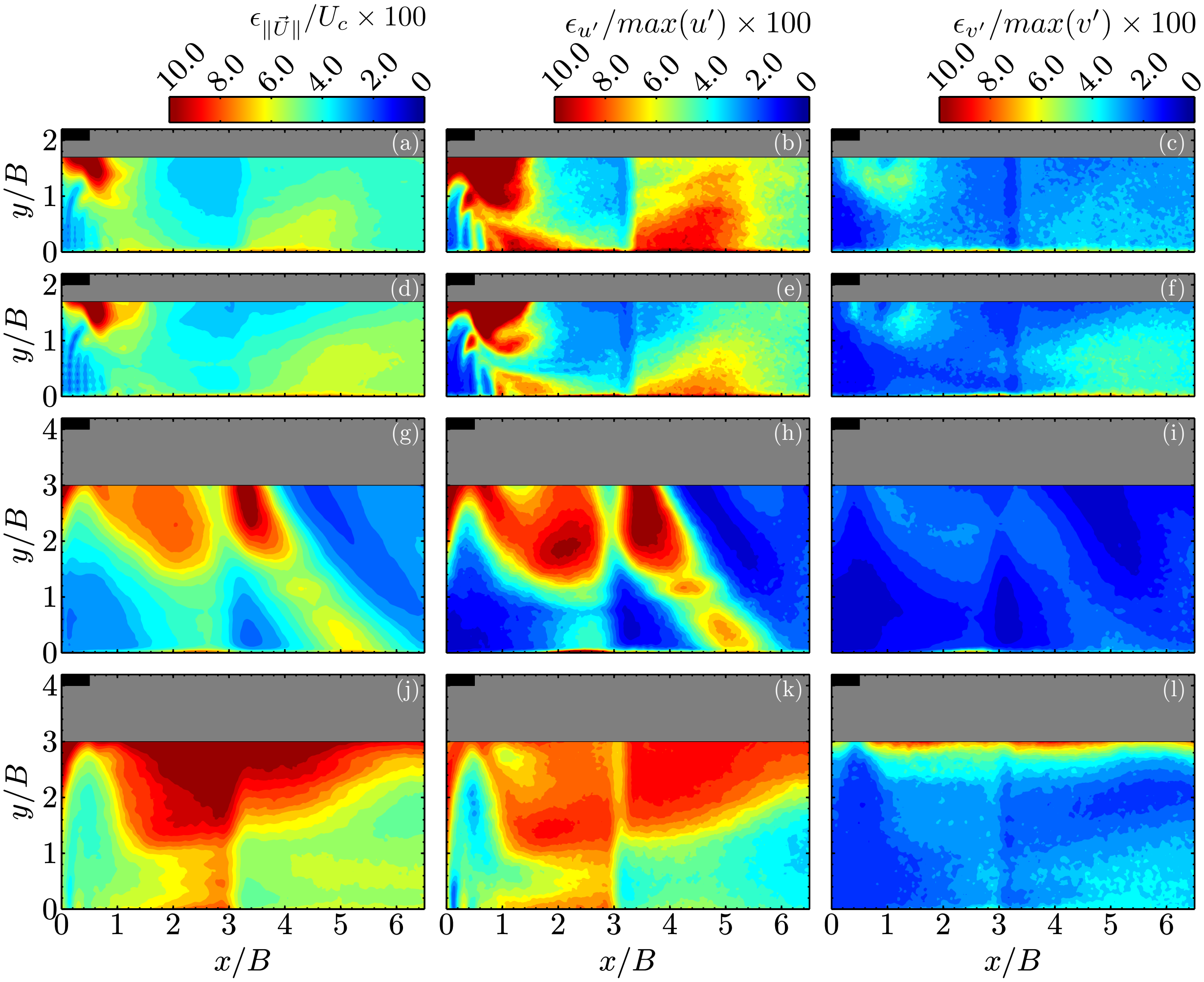

Figure B.1: Random error estimation of PIV measurements for (a-c) $H/B = 2$, $\mathrm{Re}_B = 3000$, (d-f) $H/B = 2$, $\mathrm{Re}_B = 6000$, (g-i) $H/B = 4$, $\mathrm{Re}_B = 3000$, and (j-l) $H/B = 4$, $\mathrm{Re}_B = 6000$. First column shows the uncertainty in the velocity magnitude normalized by the jet centreline velocity, middle column shows the uncertainty in the x-component of the RMS velocity field, and right column shows the uncertainty in the y-component of the RMS velocity field. The RMS velocity uncertainties are normalized by the maximum RMS value of the corresponding component.

velocity is less than the uncertainty of the surface parallel component. The effect of using two cameras is more apparent in the uncertainty of the RMS velocities as the uncertainty spatial distribution shows large spatial gradients along the surface parallel direction in the overlap region ($2.8 < x/B < 3.3$), where other contributing factors such as the laser light and seeding are expected to not vary significantly. In the regions of interest,, the relative uncertainty of the surface normal RMS velocity field is less than 8%, while the surface normal component of the relative uncertainty is less than 4%.

B.2.1 PIV Derived Quantities

An important parameter which defines the wall jet is its growth rate defined by $\mathrm{d}y_{1/2}/\mathrm{d}x$, which is typically constant when the wall jet is self-similar [53, 54]. The growth rate is estimated by extracting $y_{1/2}$ using the surface parallel component of the PIV velocity fields and applying a linear fit, where the slope of the linear fit is the growth rate. Therefore the wall jet growth rate uncertainty includes contributions from the PIV random error in the velocity field and the RSME of the linear fit. The uncertainty contribution from the PIV random error towards the wall jet growth rate is estimated by following the "method of sequential perturbation" [118, 119]. The PIV random error for the surface parallel velocity (similar to velocity magnitude uncertainty in Fig. B.1 is added and subtracted from the surface parallel velocity field in order to determine the uncertainty contribution. Th uncertainty due to the PIV error ranges from ±2% to ±9%, while the uncerntainty of the linear fit ranges from ±4% to ±8%. The two uncertainties are combined together using Eq. B.2, which results in a relative uncertainty range of $\pm 5\% \leq \epsilon_{\mathrm{d}y_{1/2}/\mathrm{d}y}/\mathrm{d}y_{1/2}/\mathrm{d}y \leq \pm 12\%$.

In the discussion pertaining to the dynamics of the coherent structures Section 4.3, the shedding frequencies of the primary vortices are determined using one-dimensional frequency spectra. The spectra shown in Figs. 4.11–14 and 4.24 are computed using Welch's averaged, modified periodogram approach [101]. Using a window size of 2^{10}, results in a frequency resolution of $\Delta f = 3.125$ and a non-dimensional frequency resolution of $\Delta \mathrm{St}_B = 0.006$ and 0.003 for $\mathrm{Re}_B = 3000$ and 6000, respectively. The uncertainty in determining a particular frequency is half of the frequency resolution, $\epsilon_{\mathrm{St}_B} = \pm 0.003$ and ± 0.0015, for $\mathrm{Re}_B = 3000$ and 6000, respectively. Therefore, the relative uncertainty in determining the shedding frequency ranges from $\pm 0.3\% \leq \epsilon_{\mathrm{St}_{B,0}}/St_{B,0} \leq \pm 0.75\%$.

When characterizing the vortex dynamics, convective velocities and characteristic wavelengths are also determined using spectral analysis. The convective velocities are extracted by using a linear fit to the convective ridge observed in the wavenumber-frequency spectra in Figs. 4.19 and 4.20. The uncertainty of the convective velocities is a function of the uncertainty due to the frequency resolution and the RSME of the linear fit. The frequency resolution is equal to the one-dimensional spectra as a consistent window size in time (2^{10}) is used. Through the use of Eq. B.2, the uncertainty of the characteristic convective velocity due to the frequency resolution ranges from $\pm 0.3\%$ to $\pm 0.75\%$. The uncertainty in the convective velocities due to the quality of the linear fit is determined by using RSME values. This results in a relative uncertainty of $\pm 10\% \leq \epsilon_{U_{cv,P}}/U_{cv,P} \leq \pm 21\%$ for the primary vortices and $\pm 9\% \leq \epsilon_{U_{sv,P}}/U_{sv,P} \leq \pm 27\%$ for the secondary vortices due to the linear fit. The uncertainty contribution from the frequency is negligible when compared to the RSME of the linear fit. The uncertainty of any wavelength extracted from the wavenumber-frequency spectra is subject to the resolution of the wavenumber. However, the uncertainty in the wavenumbers and wavelengths can be improved by selecting wavenumbers and wavelengths along the convective ridge, which has a lower uncertainty due to the higher resolution of the frequency. The resulting uncertainty of the characteristic wavenumbers ranges from $\pm 0.6\% < \epsilon_{k_0 B}/(k_0 B) < \pm 1.4\%$. This corresponds to an uncertainty range of $\pm 0.5\% < \epsilon_{\lambda_0/B}/(\lambda_0/B) < \pm 1.4\%$, for the wavelengths.